INTEGRATION OF TIME LAPSE SEISMIC DATA USING ONSET TIME AND ANALYSIS OF SPATIAL RESOLUTION

A Dissertation

by

GILL HETZ

Submitted to the Office of Graduate and Professional Studies of
Texas A&M University
in partial fulfillment of the requirements for the degree of

DOCTOR OF PHILOSOPHY

Chair of Committee,	Akhil Datta-Gupta
Committee Members,	Michael J. King
	Eduardo Gildin
	Binayak Mohanty
Head of Department,	A. Daniel Hill

December 2017

Major Subject: Petroleum Engineering

ABSTRACT

Integration of time-lapse seismic data into the reservoir model offers great potential in understanding reservoir flow patterns as well as reservoir properties. However, it also requires the solution of an inverse problem, which poses challenges in terms of dynamic reservoir modeling and seismic history matching to infer reservoir characterization.

In this dissertation, we first present a method for assessing the inversion results in underdetermined problems, resulting in a multi scale data integration, Then, we introduce a novel history matching approach to integrate frequent seismic surveys (4D) using onset times.

In the first part, an analysis of spatial resolution is incorporated into an efficient history matching approach, in order to indicate the reliability of the estimated solution. By examining the spatial resolution in seismic data integration, as a function of derivation type, we evaluate quantitatively the contribution of pressure and saturation changes on the calibrated permeability field.

Next, we present a novel and efficient approach to integrate frequent time lapse (4D) seismic data into high resolution reservoir models based on seismic onset times. Our approach reduces multiple time-lapse seismic survey data into a single map of onset times, leading to substantial data reduction for history matching while capturing all relevant information regarding fluid flow in the reservoir. We demonstrate the practical feasibility of our proposed approach through the heavy oil reservoir at Pad 31 in the

Peace River Field (Alberta, Canada) with daily time lapse seismic surveys recorded by a permanently buried seismic monitoring system.

Finally, we quantitatively investigate the effectiveness of the onset time and the amplitude inversion to solve the inverse problem associated with integrating 4D seismic data into the reservoir model.

The results of the study demonstrate the effectiveness of the onset time approach for integrating a large number of seismic surveys by compressing them into a single map. Also, the onset times appear to be relatively insensitive to the petro elastic model but sensitive to the steam/fluid propagation, making it a robust method for history matching of time lapse surveys.

DEDICATION

I dedicate this dissertation to my wife and my family.

ACKNOWLEDGEMENTS

I would like to express my sincere gratitude to my committee chair, Dr. Datta-Gupta, for his academic guidance and financial support throughout the course of this research.

I would also like to extend my sincere appreciation to my committee members: Dr. King, Dr. Gildin, and Dr. Mohanty for their thoughtful discussions and suggestions that improved the contents of this dissertation.

Special thanks also go to MCERI alumni and current students for their mentorship, partnership and friendship though my study life.

Also, I would like to thank the Israeli Ministry of National Infrastructures, Energy and Water Resources for the financial support.

I would like also to thank Shell (operator of the Peace Revir field) for providing the field data.

Finally, thanks to my mother and father for their encouragement and to my wife for her patience and love.

CONTRIBUTORS AND FUNDING SOURCES

Contributors

This work was supervised by a dissertation committee consisting of Professor Akhil Datta-Gupta (advisor), Michael J. King, and Eduardo Gildin of the Department of Petroleum Engineering and Professor Binayak Mohanty of the Department of Biological and Agricultural Engineering.

The global stage of history matching in Chapter III was collaborated with Hyunmin Kim and will be published in 2017. The student designed the global history matching workflow. In Chapter IV, the synthetic case was contributed by Hongquan Chen.

All other work conducted for the dissertation was completed by the student independently.

Funding Sources

This work was made possible by the financial support of the member companies of the Model Calibration and Efficient Reservoir Imaging (MCERI) consortium.

TABLE OF CONTENTS

Page

LIST OF FIGURES

Page

LIST OF TABLES

Page

CHAPTER I

INTRODUCTION AND STUDY OBJECTIVES

Reconciling geologic models to the dynamic response of the reservoir, also known as history matching, is critical for building reliable reservoir models. This is a type of inverse problem in which the data misfit between observed reservoir behavior and calculated response from the forward simulator is minimized by calibrating the reservoir properties. The history matched model is then used for predicting fluid displacement patterns and related decision options concerning reservoir management and field development.

The dynamic data could be production history, well test, tracer response, and 4-D seismic data. The possibility of integrating seismic surveillance data is particularly attractive because of the large areal coverage of the seismic data. This large quantity of information can be utilized to infer reservoir properties far from the wells. However, it poses new challenges in terms of dynamic reservoir modeling and history matching. In this dissertation, we focus on efficient integration of seismic data, under varying field conditions, to infer changes in the state of the reservoir.

In this chapter, we start with an overview of reservoir modeling. Then, the history matching problem is generally described. Finally, study objectives and the outline of this dissertation are summarized.

1.1 Overview of Reservoir Simulation

Reservoir simulation is the most comprehensive tool applied to describe the fluid movement within the reservoir. It provides a numerical solution to a set of partial differential equations ("PDEs") that define the conservation laws (mass, momentum and energy) and a set of constitutive equations that determine the behavior of fluids in the formation for a given set of boundary conditions (well locations, rates, pressures, aquifer, gas cap, etc.) and initial conditions (oil water contacts, gas oil contact, initial pressure, fluids in place, etc.). Based on the simulation response, one can design a production strategy to maximize recovery.

Reservoir modeling typically begins with the conceptual geologic model and the identification of regional attributes such as facies or depositional sequences, domain boundaries and boundary conditions, and faults. After identifying the reservoir, the geological model turned into a discrete system (e.g. the simulation grid) on which the flow equations can be solved. The geological model is typically up-scaled as its resolution is higher than it is practical to include in a reservoir flow simulation. The next step is to construct the model using early stage of production data, well logs, core data to infer initial fluid saturation distributions and flow properties such as permeability and porosity.

Given the disparity in resolution of various types of measurements available, from seismic down to the core, the petrophysical properties are sampled into the simulation grid by utilizing geostatistical tools. The initialization of the reservoir equilibrium conditions occurs after the PVT data and the core analysis become available

from laboratory experiments. For a given production schedule, one can conduct the reservoir simulation in order to forecast the production of fluids at the field facilities. The responses of the reservoir simulation are used to select a business development plan which aims to maximize the oil recovery while minimizing the operational cost with some acceptable level of risk.

1.2 Overview of History Matching

The reservoir model always consists of large numbers of subsurface uncertainties. Models derived exclusively from static data often fail to reproduce the observed dynamic production history and consequently will most likely give a poor recovery prediction. Therefore, integrating historical dynamic production data is a critical step to develop reliable reservoir performance models. The process is referred to as history matching or model calibration.

Traditionally, history matching is performed manually on a single reservoir model by sequential trial-and-error adjustments of the reservoir properties(Datta-Gupta and King 2007). This process involves considerable subjective judgment and can create artificial discontinuities inside the reservoir, potentially destroying the correlation built into the initial geologic model.

Recently, we are witnessing an increase in the use of assisted history matching (AHM) methods for the characterization of flow properties in the subsurface. The AHM is mainly rooted in the concept of inverse theory to minimize an appropriately defined misfit function to obtain a history match. The majority of the methods can be broadly

categorized into two classes: deterministic (Hoffman et al. 2006; Vega et al. 2004) and stochastic,(Granville et al. 1994; Hastings 1970).

The stochastic methods are often used to find the global parameter. These methods are typically non-gradient methods such as Monte-Carlo methods and the Ensemble Kalman Filter. The stochastic methods usually adopt the Bayesian formulation that provides a convenient framework for combining data and prior information (Tarantola 2005). A sub-category of the stochastic methods is the heuristic methods. The algorithms are population-based optimization algorithms and often refer to evolutionary algorithms such as genetic algorithm. The genetic algorithms typically use random uniform sampling for mutation of parameters and search for best combinations of model parameters that reduce objective functions in the history matching problem. One major drawback with stochastic optimization methods is that they may require hundreds or thousands of evaluations of the reservoir model response, which can be prohibitive for reservoir models that are CPU-intensive.

While the number of simulations and amount of computational resources are limited, history matching often needs to be carried out with a small number of reservoir simulations. Typically, the stochastic method are used to find the global parameters, and then deterministic approaches are used to update the fine scale static parameters. In the deterministic approaches, the efficiency of calculating the parameter sensitivities is a key to conduct such high resolution reservoir model updating. In order to find the parameter sensitivities, we have to relate between the dynamic response of the simulator and the flow properties where the following approaches are generally used: perturbation

methods, gradient-simulator methods (Anterion et al. 1989) and adjoint or optimal control methods (Chavent et al. 1975; Li et al. 2001). The perturbation method is computationally prohibitive for a large number of parameters because it requires ($N+1$) forward simulation where N is the number of parameters (e.g. grid cells). The adjoint method or the optimal control theory becomes more popular for accurately computing the gradient of a function of the state variables with respect to model variables, where the adjoint state variables can be interpreted as measures of importance of variables describing the reservoir. However, it typically requires access to the source code of the forward simulator, which may not be available (Rey et al. 2009). The amount of information and the indirect relationship between the seismic response and the reservoir state are major challenges for the implementation of those techniques when dealing with large 4D seismic data sets.

Recently, streamline techniques have proven to be particularly efficient to calibrate static properties from dynamic well responses. They have also been applied for integrated changes using seismic data but mostly focused on amplitude and magnitude match (Rey et al. 2012; Watanabe et al. 2017). This approach has many advantages in terms of computational efficiency and applicability (Datta-Gupta and King 2007). The main advantage of the streamline-based method is that it requires a single forward simulation with a post-processing step to find parameter sensitivity by analytical formulation. Furthermore, data integration based on travel time sensitivities leads to a minimization procedure that exhibits quasi-linear properties, converging in a smaller number of iterations, and is less likely to trap into a local minima compared to amplitude

inversion algorithms (Cheng et al. 2005; Luo and Schuster 1991; Vasco and Datta-Gupta 1999).

This research aims to provide a novel approach of seismic data integration using the concept of onset time (Vasco et al. 2015; Vasco et al. 2014). The proposed approach relates the initiation of a change in the geophysical property to the arrival time arrival time of a particular physical phenomenon (e.g. the saturation front and/or the pressure front). Such fluid phase arrival times can often be linked to flow properties and are very suitable to the streamline-based method. We also incorporate an efficient approach to indicate the reliability of the estimated solution using the analysis of spatial resolution.

1.3 Research Objectives and Dissertation Outline

The research focuses on the development of efficient history matching methods for 4-D seismic data and exploring the model parameter estimation. The main objectives and corresponding chapters of this dissertation are as follows.

- In Chapter II, we present the streamline-based seismic amplitude sensitivity and perform an analysis of spatial resolution to indicate the reliability of the estimated solution. We illustrate our results using both synthetic case and field applications of 4-D seismic and production data.
- In chapter III, we develop and validate a novel and efficient approach to integrate frequent time lapse (4D) seismic data in to the reservoir model based on the concept of seismic onset times.

- In chapter III, we also apply a hierarchical history matching workflow in a real field application, which involves steam injection into a heavy oil reservoir with daily time lapse seismic surveys.
- In chapter IV, we discuss the mathematical foundation for the measure of nonlinearity and its implications on the seismic-data integration. We quantitatively investigate the extent of nonlinearity in onset time inversion and amplitude inversion. We illustrate our results using both synthetic and field applications.

CHAPTER II

INTEGRATION OF TIME-LAPSE SEISMIC AND PRODUCTION DATA: ANALYSIS OF SPATIAL RESOLUTION

2.1 Chapter Summary

In this chapter, an analysis of spatial resolution is incorporated into an efficient history matching approach with multi-scale data integration, in order to indicate the reliability of the estimated solution. The resolution is a measure of the degree of averaging the local–scale (gridblock) permeabilities. For a given set of data, it indicates the regions where our estimate is well constrained. By examining the spatial resolution in seismic data integration, as a function of derivation type, we can evaluate quantitatively the contribution pressure and saturation changes on the calibrated permeability field.

We illustrate this concept using synthetic and field applications. The first example is a 5 spot pattern, where the seismic data is provided as pressure and saturation changes. The field example, involves waterflooding of a North Sea reservoir with multiple seismic surveys. The results demonstrate that the analysis of spatial resolution provide a quantitative information on our ability to estimate the subsurface heterogeneity based on a given set of data. It is found that integration of seismic data with respect pressure changes better determine the barriers to the flow (e.g. low permeability areas), while calibrating the model based on saturation provides a compliment information to solve the channels (e.g. high permeability areas).

2.2 Introduction

Integration of 4-D seismic acquisitions, along with the production data, improves the data characterization and reduces the uncertainty associated with the estimated model. Such information has a great potential in inferring reservoir properties, such as permeability and porosity through the reservoir model calibration process. Different algorithms of dynamic data integration have been proposed in the literature to reconcile the reservoir model heterogeneity with temporal changes in seismic attributes (Dong and Oliver 2005; Fahimuddin et al. 2010; Falcone et al. 2004; Huang et al. 1997; Mavko et al. 2009; Rey et al. 2012; Skjervheim et al. 2007; Vasco 2004; Watanabe et al. 2017) (Mavko, 1998; Falcone et al., 2004 ;Huang et al. 1997 ;Vasco et al. 2004 Dadashpour et al., 2008, 2009, 2010 ; Gosselin et al. 2001 ; Dong and Oliver 2005; Skjervheim et al. 2007; Fahimuddin et al. 2010; Rey et al. 2012; Watanabe et al.2017) .

The integration of dynamic data (seismic, production) typically requires the solution of an inverse problem that can be computationally intensive. A critical issue here is the calculation of the sensitivity coefficients, the derivatives of dynamic data history with respect to the flow properties. We follow Watanabe et al.'s (2017) approach of an efficient history matching that simultaneously integrates 4-D seismic surveys with well production data, using streamline-based analytic sensitivities for fluid saturation and pressure data integration to calibrate the model. The possibility of incorporating 4-D seismic data with high spatial resolution into history matching not only enables a better understanding of the fluid flow away from the well locations, but also allows us to assess the parameters estimates and determining their reliability in a grid cell resolution.

Traditionally, most of the efforts in assessing the inversion have been focused on quantifying the uncertainty associated with parameters estimates, while very little exist in the petroleum literature on the resolution analysis(Datta-Gupta et al. 1997; Datta-Gupta et al. 2002; Vasco et al. 1997). In this study, we are interested in exploring the model parameter estimation by using the concept of the model resolution analysis. The model resolution matrix is useful for quantifying the nonuniqueness of inversion results in underdetermined problems (Menke 2012). Nonuniqueness and instability of the inverse solutions are reflections of the illposed nature of the inverse problems, where the ill-posedness is a result of limited data and its associated uncertainty(Backus and Gilbert 1968; Backus and Gilbert 1967). For large cases, it is difficult to obtain a specific value for each cell and one can only constrain spatial averages of the value as some combination of block permeabilities (Vasco et al. 1997). The concept of model resolution introduced by Backus and Gilbert (1967, 1968) formed a foundation for inverse geophysical problems to provide insight of the parameters spatial averaging. Further work on the model parameters resolution has been done by Tarantola (2005) ,Parker (1994) and Menke (2012)showing that the resolution matrix provides a measure of the spatial averaging inherent in our inverse modeling.

There is a trade-off between the model resolution and the model covariance (Backus &Gilbert 1970; Menke ,1989; Parker, 1994). A solution with small spread resolution tends to have large variance and vice versa (Menke, 2014). Many inverse methods have a tunable parameter that defines a “trade-off curve” of allowable combinations of spread resolution and size of the covariance (Menke 2012; Tarantola

2005; Wiggins 1972).(Xia et al. 2010) consider using a proper regularization parameter to find a trade-off between model resolution and model covariance matrices in the vicinity of a regularized solution. Here, the trade-off solution, is calculated by truncated inverse of a data kernel (Hansen 1998; Parker 1994) with the singular value decomposition (SVD) (Golub and Reinsch 1970; Lanczos 1996) in order to achieve a meaningful solution from limited observation by combing both the data space and the model space.

In this chapter, we start with the mathematical background of the streamline-based analytic sensitivities for fluid saturation and pressure data integration. Next, we derived the resolution and the covariance matrices for the flow properties of the subsurface. We illustrate an analysis of spatial resolution for history matching application of time-lapse data to evaluate the reliability of the estimated solution. We also outline the relative contribution of pressure and saturation on the seismic integration and discus the sequence order of seismic integration. Finally, we apply the proposed approach to the Norne field, where the time-lapse acoustic impedance change derived from the post-stack seismic amplitude data.

2.3 Background and Methodology

In this section, we discuss our theoretical and computational framework for inversion and analysis of dynamic reservoir response: production and time lapse seismic using the streamlines approach. First, we demonstrate the relations of the reservoir properties to the dynamic reservoir response, as known as the sensitivities. This includes

time of flight sensitivity, saturation front arrival time sensitivity, water saturation sensitivity, and pressure drop sensitivity. In the second stage we show the spatial resolution analysis using SVD approach in order to evaluate the inversion process.

2.3.1 Time of Flight Sensitivity Calculation

The time of flight (TOF) is defined as the travel time of a neutral tracer along a streamline trajectory (Datta-Gupta,& King, 2007) ,

$$\tau(\psi) = \int_{\psi} s(x)dr \tag{2.1}$$

where ψ is the streamline trajectory, *r* is distance along the streamline, and *s* is the slowness defined by the reciprocal of the interstitial velocity

$$s(\boldsymbol{x}) = \frac{1}{\left|\vec{v}(\boldsymbol{x})\right|} = \frac{\phi(\boldsymbol{x})}{\lambda_{rt} k(\boldsymbol{x}) \left|\nabla P\right|}. \tag{2.2}$$

Using Darcy's law, here λ_{rt} is the total relative mobility, $\lambda_{rt} = \lambda_{ro} + \lambda_{rw} + \lambda_{rg}$ and $\left|\nabla P\right|$ is the pressure gradient along the streamline. Because slowness is a composite quantity involving reservoir properties, its first order variation, assuming a fixed pressure gradient, will be given by

$$\delta s(\boldsymbol{x}) = \frac{\partial s(\boldsymbol{x})}{\partial k(\boldsymbol{x})} \delta k(\boldsymbol{x}) + \frac{\partial s(\boldsymbol{x})}{\partial \phi(\boldsymbol{x})} \delta\phi(\boldsymbol{x}). \tag{2.3}$$

From **Eq. 2.2,** the partial derivatives are then simply computed as the following

$$\frac{\partial s(\boldsymbol{x})}{\partial k(\boldsymbol{x})} \approx \frac{-\phi(\boldsymbol{x})}{\lambda_{rt} \left(k(\boldsymbol{x})\right)^2 \left|\nabla P\right|} = -\frac{s(\boldsymbol{x})}{k(\boldsymbol{x})}, \tag{2.4}$$

$$\frac{\partial s(\boldsymbol{x})}{\partial \phi(\boldsymbol{x})} \approx \frac{1}{\lambda_{rt} k(\boldsymbol{x}) |\nabla P|} = \frac{s(\boldsymbol{x})}{\phi(\boldsymbol{x})}, \tag{2.5}$$

In **Eq. 2.4** and **Eq. 2.5,** we assume that local perturbations in permeability or porosity generated by pressure changes can be neglected. This means that streamlines do not shift because of these small perturbations. By integrating along each streamline trajectory, the relationship between the change in the TOF ($\delta\tau$) and the change in slowness can be written as

$$\delta\tau(\psi) = \int_{\psi} \delta s(x) dr = \int_{\psi} \left[\frac{\partial s(x)}{\partial k(x)} \delta k(x) + \frac{\partial s(x)}{\partial \phi(x)} \delta\phi(x) \right] dr . \tag{2.6}$$

The tracer travel time sensitivity along a single streamline, ψ with respect to permeability and porosity at location $\boldsymbol{x}$ follows **Eq. 2.6** by integrating from the inlet to the outlet of the streamline within the gridblock,

$$\frac{\delta\tau(\psi)}{\delta k(\boldsymbol{x})} = \int_{\text{inlet}}^{\text{outlet}} \left[-\frac{s(\boldsymbol{x})}{k(\boldsymbol{x})} \right] dr = -\frac{\Delta\tau(\boldsymbol{x})}{k(\boldsymbol{x})}, \tag{2.7}$$

$$\frac{\delta\tau(\psi)}{\delta\phi(\boldsymbol{x})} = \int_{\text{inlet}}^{\text{outlet}} \left[\frac{s(\boldsymbol{x})}{\phi(\boldsymbol{x})} \right] dr = \frac{\Delta\tau(\boldsymbol{x})}{\phi(\boldsymbol{x})} . \tag{2.8}$$

Here $\Delta\tau(x)$ is the time-of-flight across the gridblock at location x .

2.3.2 Saturation Front Arrival Time Sensitivity

We now relate the time of flight sensitivity to the travel time sensitivity of the water saturation. Consider two phase incompressible flow of oil and water described by the Buckley-Leverett equation written using the streamline time of flight as the spatial coordinate (Datta-Gupta,& King, 2007) ,

$$\frac{\partial S_w}{\partial t} + \frac{\partial F_w}{\partial \tau} = 0 . \tag{2.9}$$

The velocity of a given saturation S_w along a streamline ψ is given by the slope of the fractional flow curve,

$$\left(\frac{\partial \tau}{\partial t} \right)_{S_w} = \frac{dF_w}{dS_w} . \tag{2.10}$$

This equation relates the travel time of a saturation, $t(S_w,\ \tau;\psi)$ to the TOF τ .We can now compute the sensitivity of the saturation arrival time using that of the streamline TOF as follows

$$\frac{\delta t(S_w,\ \tau;\psi)}{\delta k(\boldsymbol{x})} = \frac{\delta \tau(\psi)}{\delta k(\boldsymbol{x})} \Big/ \frac{dF_w}{dS_w} , \tag{2.11}$$

$$\frac{\delta t(S_w,\ \tau;\psi)}{\delta \phi(\boldsymbol{x})} = \frac{\delta \tau(\psi)}{\delta \phi(\boldsymbol{x})} \Big/ \frac{dF_w}{dS_w} . \tag{2.12}$$

After water breakthrough on a streamline, these arrival times are evaluated at the total time of flight, $\tau(\psi)$, for the streamline.

2.3.3 Water Saturation Sensitivity Calculation

Our goal here is to derive expressions for the sensitivity of water saturation with respect to variations in permeability. In two phase flow, water saturation is a function of the streamline TOF, τ ,and time, t . We consider a self-similar solutions to **Eq.2.9**, where the saturation is a function of the dimensionless ratio τ / t . This allows us to relate the derivative of saturation with respect to time to the derivative with respect to τ can be written as:

$$\frac{\partial S_w}{\partial t} = -\frac{\tau}{t^2}\frac{dS_w(\tau/t)}{d(\tau/t)} \tag{2.13}$$

$$\frac{\partial S_w}{\partial \tau} = \frac{1}{t}\frac{dS_w(\tau/t)}{d(\tau/t)}, \tag{2.14}$$

hence

$$\frac{\partial S_w}{\partial \tau} = -\frac{t}{\tau}\frac{\partial S_w}{\partial t}, \tag{2.15}$$

leads us to the water saturation sensitivity:

$$\frac{\delta S_w(\tau,t)}{\delta k(x)} = \frac{\partial S_w}{\partial \tau}\frac{\delta \tau}{\delta k(x)} = -\frac{t}{\tau}\frac{\partial S_w}{\partial t}\frac{\delta \tau}{\delta k(x)}. \tag{2.16}$$

We calculated the partial derivative of water saturation with respect to time in Eq. 2.16 by using a backward time difference as

$$\frac{\partial S_w(\tau,t)}{\partial t} \approx \frac{S_w(\tau,t) - S_w(\tau,t-\Delta t)}{\Delta t}. \tag{2.17}$$

here Δt is the timestep size. This requires saving the saturation information for the time step immediately prior to the time lapse survey time. Therefore, the saturation sensitivity at location τ at a given time t can be calculated by:

$$\frac{\delta S_w(\tau,t)}{\delta k(x)} = -\frac{t}{\tau}\frac{S_w(\tau,t) - S_w(\tau,t-\Delta t)}{\Delta t}\frac{\delta \tau}{\delta k(x)}, \tag{2.18}$$

where the last partial derivative of travel time, with respect to permeability, can be obtained from **Eq. 2.7**.In this paper we calibrate against the changes in saturation, rather than the saturation itself. The generalization of the sensitivity calculation to account for these effects can be found in Watanabe et al. (2017).

2.3.4 Pressure Data Integration

The streamlines are traced using pressure gradient generated by injector or producer. Normally, pressure is solved on 3D grid space however, in order to calculate pressure sensitivities we construct pressure equation along streamline and take the derivative with respect to reservoir parameters. That is, we evaluate the pressure drop along the streamlines and relate it a particular gridblock.Figure 2.1 demonstrates the process, where i is a particular location with pressure of p_i , the red line is the streamline passing through location i and leading to the producer with bottom hole pressure P_w . The pressure drop, $\Delta P|_w^i$ along the streamline can be written as:

$$P_i = P_w + \Delta P\big|_w^i . \tag{2.19}$$

If the distributed time lapse pressure data and well bottom hole pressure, we can compute the pressure drop from **Eq. 2.19** and use it as our observation data,

$$\Delta P\big|_{w,obs}^i = P_{i,obs} - P_{w,obs} . \tag{2.20}$$

The data misfit between the simulation response and observation can be written as

$$\begin{aligned} \delta d_i &= \Delta P\big|_{w,obs}^i - \Delta P\big|_{w,cal}^i = \left(P_{i,obs} - P_{w,obs}\right) - \left(P_{i,cal} - P_{w,cal}\right) \\ &= \left(P_{i,obs} - P_{i,cal}\right) - \left(P_{w,obs} - P_{w,cal}\right) \end{aligned} . \tag{2.21}$$

The first term is the pressure difference at location *i*, and the second term is the bottom hole pressure difference at well.

2.3.5 Pressure Drop Sensitivity Calculation

This can be computed by simply summing up the pressure drop across the grid blocks that intersect the streamline as shown in Figure 2.1. Further, we can express the local pressure drop along a streamline using Darcy's law as

$$\Delta P(\boldsymbol{x}) = \frac{q(\boldsymbol{x})\Delta L(\boldsymbol{x})}{A(\boldsymbol{x})\lambda_{rt}k(\boldsymbol{x})}, \tag{2.22}$$

where $A(x)$ is the cross sectional area, $q(x)$ is the flow rate along a streamline, λ_{rt} is the total relative mobility, and $\Delta L(\boldsymbol{x})$ is the arc length of the streamline within the gridblock. The pressure drop is a composite quantity involving reservoir properties. We assume that the streamline trajectories, flow rate along streamline and the total mobility do not change because of small perturbations in permeability. We can now relate the change in local pressure drop to a small change in permeability as

$$\delta\Delta P(\boldsymbol{x}) = \frac{\partial \Delta P(\boldsymbol{x})}{\partial k(\boldsymbol{x})}\delta k(\boldsymbol{x}), \tag{2.23}$$

where the partial derivative is

$$\frac{\partial \Delta P(\boldsymbol{x})}{\partial k(\boldsymbol{x})} \approx \frac{-q(\boldsymbol{x})\Delta L(\boldsymbol{x})}{A(\boldsymbol{x})\lambda_{rt}\left(k(\boldsymbol{x})\right)^2} = -\frac{\Delta P(\boldsymbol{x})}{k(\boldsymbol{x})}\ . \tag{2.24}$$

The pressure drop to a location i, $\Delta P|_w^i$ will be given by integration along the streamline trajectory passing through i to well w,

$$\delta\,\Delta P\big|_w^i = \int_{\psi} \delta\Delta P(\boldsymbol{x})\,dr = \int_{\psi}\left[\frac{\partial \Delta P(\boldsymbol{x})}{\partial k(\boldsymbol{x})}\delta k(\boldsymbol{x})\right]dr \tag{2.25}$$

and the pressure drop sensitivity for a particular gridblock at location $\boldsymbol{x}$ follows from **Eq. 2.25**,

$$\frac{\partial \Delta P\big|_w^i(\psi)}{\partial k(\boldsymbol{x})} = \int_{\text{location}}^{\text{outlet}} \left[-\frac{\Delta P(\boldsymbol{x})}{k(\boldsymbol{x})} \right] dr = -\frac{\Delta P(\boldsymbol{x})}{k(\boldsymbol{x})}. \tag{2.26}$$

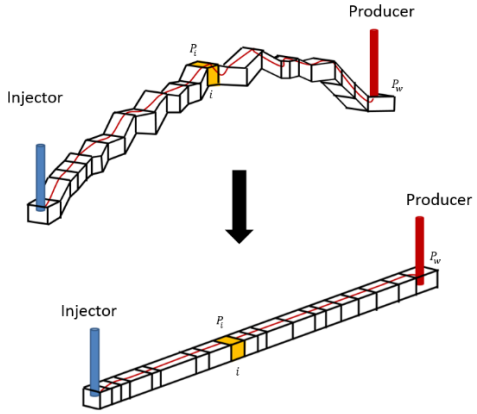

Figure 2.1 Pressure drop along the streamline.

2.3.6 The Inverse Problem and Analysis of Spatial Resolution

In this section, we describe the concept of the resolution and the solution of the inverse problem through the minimization of a penalized misfit function. Our goal is to reconcile high resolution geologic model to a given set of observation. In such a case, there are many more parameters describing the reservoir than there are observations. Furthermore, the relationship between the subsurface properties and the observations is highly nonlinear, which introduce another source of non-uniqueness. To overcome these

limitations, we use some form of regularization or penalty term into the inversion. We start with a prior knowledge about our model and solve the regularized inverse problem which minimize the sum

$$o(\delta m) = \|\delta d - G\delta m\| + \|\beta_1 \delta m\| + \|\beta_2 L\delta m\|. \quad (2.27)$$

Here, δd is the misfit between the observed data and the values estimated from the reservoir model. The matrix *G* contains the sensitivities of model responses with respect to reservoir parameters, δm is the vector of reservoir model parameter updates, and *L* is a second spatial difference operator matrix. The first term ensures the differences between the observed data and calculated model predictions are minimized. The second term, called a norm penalty, penalizes deviations from the prior model. The third term, referred to as a roughness penalty, constrains the model changes to be spatially smooth, in line with the resolution provided by the data. The weights β_1 and β_2 determine the relative strengths of the prior model and roughness conditions. An iterative sparse matrix solver, the LSQR algorithm (Paige and Saunders 1982) is used for solving the augmented linear system efficiently.

The next logical step is to determine the uncertainty associated with the estimates and the spatial averaging of the estimated model. For nonlinear problems, once the solution has been reached, the model parameters can be further assessed using the concept of the resolution analysis, based on a local linearization of the obtained solution.

The resolution and the covariance matrices are derived from the sensitivities matrix (G), which relates variation in the permeability to change in a specific

observation. The columns of the matrix present the gridblocks of the model and each row represents different observe data. In the matrix form we write as:

$$G\delta k = \delta d \tag{2.28}$$

where G is the sensitivity matrix, δk is the change in the paremeter we wish to solve and δd is the difference between the observed data and the simulated data. There is a true, but unknown set of model parameters δk^{true} that solve

$$G\delta k^{true} = \delta d \tag{2.29}$$

Now, our estimated model δk^{est} can be described by looking at the general inverse form:

$$\delta k^{est} = G^{-g}\delta d \tag{2.30}$$

Substituting Eq.2.29 into Eq.2.30 gives

$$\delta k^{est} = [G^{-g}G]\delta k^{true} = R\delta k^{true} \tag{2.31}$$

Here R is the $M \times M$ model resolution matrix (Menke 2012; Tarantola 2005). The resolution matrix can be interpreted as a linear filter through which we view the actual spatial distribution of our model (Datta-Gupta et al. 2002; Vasco et al. 1997). The diagonal elements' values are between 1 to zero. They indicate whether the estimation of a specific cell in the model is well or poorly constrained, with respect to the true model. 1 means that it is perfectly resolved and zero means that it cannot be resolved with the observation that we have. The diagonal is called the resolution of our model. The rows of the resolution matrix are averaging coefficients indicating the contribution of various other parameters to our estimate of a property in a given cell. We use SVD method to assess the model parameter estimates. In history matching problems most of the time the

number of unknowns is much higher than the number of equations. In the sense of our problem, this simply means that the number of columns in the sensitivity matrix is higher than the number of rows. The SVD provides us with a decomposition for a rectangular, rather than a square, matrix. The sensitivity matrix can be written as the following product:

$$G = USV^T \tag{2.32}$$

U is an $M \times M$ orthogonal matrix with columns that are unit basis vectors spanning the data space, V is an $N \times N$ orthogonal matrix with columns that are basis vectors spanning the model space and S is an m by n diagonal matrix with diagonal elements called singular values.The general inverse is

$$G^{-g} = VS^{-1}U^T, \tag{2.33}$$

substituting **Eq.2.32** and **2.33** into **Eq.2.31** leads to

$$R = VS^{-1}U^TUSV^T = VV^T, \tag{2.34}$$

where R is the model resolution matrix as shown in **Eq.2.31**.

In order to estimate the uncertainties associated with our model we investigate the model parameter covariance. Under the assumption of independent and normally distributed measurement errors with constant standard deviation (Aster et al. 2013), the model parameter covariance for the generalized inverse would be

$$Cov_m = \sigma^{-2}G^{-g}cov_d\left(G^{-g}\right)^T = VS^{-2}V^T, \tag{2.35}$$

σ is the standard deviation of the data. The covariance of the model parameters depends on the covariance of the data cov_d and the way in which error is mapped from data to

model parameters. This mapping is a function of only the data kernel and the generalized inverse, not of the data itself (Menke 2012).

2.3.7 Resolution–Covariance Trade-off

There is a trade-off between model resolution and covariance (Backus and Gilbert 1968; Backus and Gilbert 1967; Menke 2012; Parker 1994). Theoretically, if we set all the elements of data covariance to zero, we could achieve the resolution matrix as identity matrix. Where this is the case, the covariance of the model becomes large and every small error in our data has a huge effect in our model. In our approach, we adopt a truncation level $P_{cut-off}$ of the SVD for eliminating those singular vectors, columns of *U* and *V*, associated with elements that are close to zero. For this truncation level, **Eq. 34** becomes

$$R = V_p S_p^{-1} U_p^T U_p S_p V_p^T = V_p V_p^T, \tag{2.36}$$

where the subscript denotes that only *p* columns of *U* and *V* are retained. At the same time we investigate the trace of the model covariance associated with truncation level $P_{cut-off}$

$$trace\left(\left[COVm_p\right]\right) = \sum_{i=1}^{N}\left[COVm_p\right]_{ii}. \tag{2.37}$$

As we use more eigenvectors, the resolution increases and at the same time the trace of the model covariance increases. As noted previously, our goal is to have the best resolution possible but at the same time to keep the covariance reasonable. Figure 2.2 shows the relationship between the number of eigenvectors used to generate the model resolution and the trace of the associated covariance model for a synthetic 2-D model

case. The model has a total of 2295 eigenvectors. As can be seen, the trace of the covariance increases when the cut-off level is getting bigger. For this case we used a value of p=700.

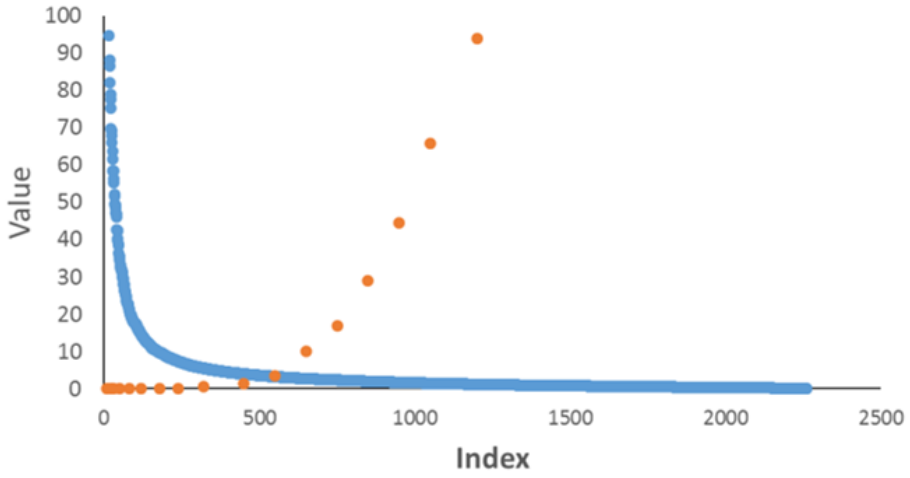

Figure 2.2 Trade-off curve. The blue dots are the singular values. The orange dots are the trace of the covariance associated with those values.

2.4 History Matching Applications

2.4.1 Five–Spot Synthetic Case - Order of Integration

Since our history matching follows a sequential approach, an important aspect that we have to consider when preforming history matching is the hierarchical frame of integrating the data. That is, we need to decide which property we account for first, the pressure or the saturation changes. In the first example, we will examine two hierarchical frames to calibrate the model: (1) our hierarchical frame first integrates the pressure effects follows by the saturation and (2) integration of saturation changes follows by pressure. Our synthetic 2-D model containing 50 x 50 x 1 cells. It is a five spot model with one injector at the center and four producers at the corners. Wells are constrained by the historical reservoir flow rates. Table 2.1 shows the rock and fluid properties. Table 2.2 represents the simulation specifications. The relative permeability curves are shown in Figure 2.3. We use a sequential Gaussian simulation to generate both the reference permeability (Figure 2.4a) and the prior permeability models (Figure 2.4b), but we use different geostatistical parameters in order to create the prior model. We generated the observation data using a commercial reservoir simulator. The seismic observation data is provided as 2-D maps of pressure and saturation changes between 260 days and 1560 days from the start of the production (Figure 2.5).In addition, the well production data is available as water-cut and bottom-hole -pressure at the well locations.

Table 2.1 Rock and fluid properties

Porosity	0.25
Rock compressibility, $\frac{1}{\text{psi}}$	8.10E-06
Oil density, $\frac{\text{lb}}{\text{cf}}$	52.1
Water density, $\frac{\text{lb}}{\text{cf}}$	63.3
Oil viscosity, cp	0.29
Water viscosity, cp	0.31
Oil formation volume factor	1.305
Water formation volume factor	1.04

Table 2.2 Simulation specifications of the synthetic case

Grid number	50x50x1
Grid size, ft	32.8x32.8x32.8
Initial pressure, psi	5863.8
Injector location	(25,25,1)
Injector rate, $\frac{bbl}{day}$	2515
Producer locations	(1,1,1),(1,50,1) (50,1,1),(50,50,1)
Producer rate, $\frac{bbl}{day}$	628
Total simulation time, $days$	2080
Time step size, $days$	260

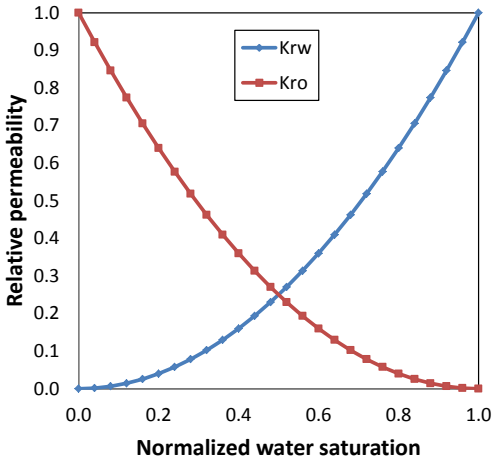

Figure 2.3 Relative permeability curves.

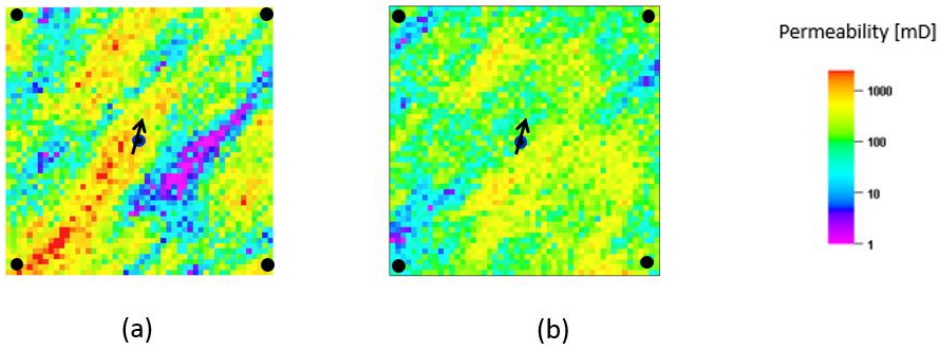

Figure 2.4 Permeability fields. (a) Reference model, and (b) Initial model.

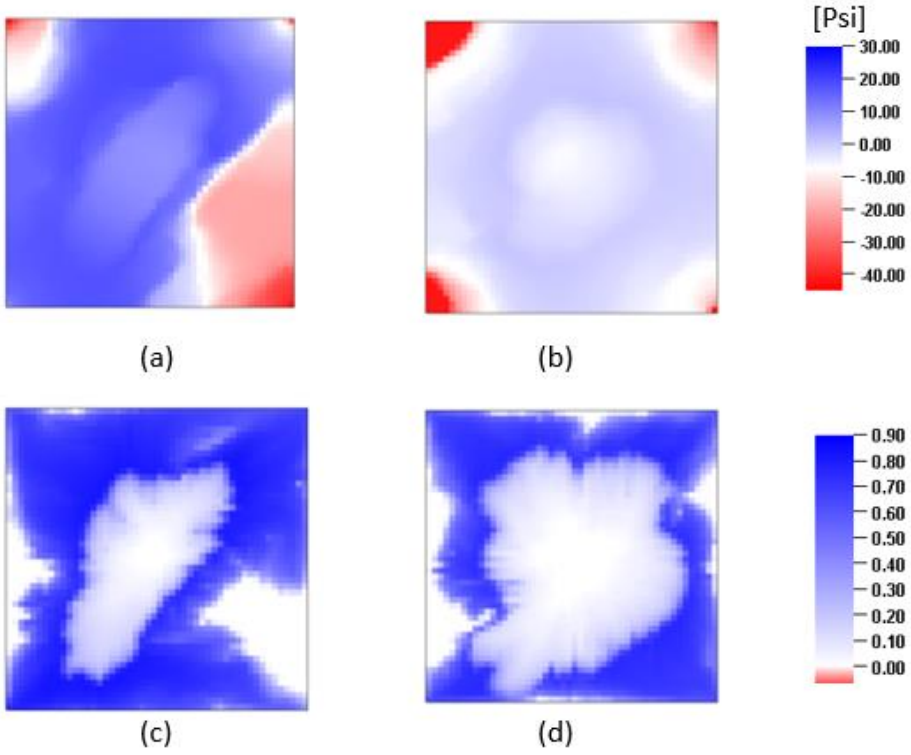

Figure 2.5 Time-lapse data between 260 days and 1560 days. (a) Reference model pressure changes, (b) Initial model pressure changes, (c) Reference model saturation changes, and (d) Initial model saturation changes.

A comparison of the misfit reduction for case 1 and 2, shown in Figure 2.6, displays a notable reduction for both cases. The fit to the time-lapse pressure and saturation changes is improved significantly for both cases (Figure 2.7 and Figure 2.8**)**, showing almost identical results. In addition, water cut data of the wells for both cases shows good agreement as shown in Figure 2.9. These results suggest that we do not have enough information to uniquely constrain our solution.

Thus, the solution of the inverse problem is not unique, and we get multiple solutions that satisfy the objective function.

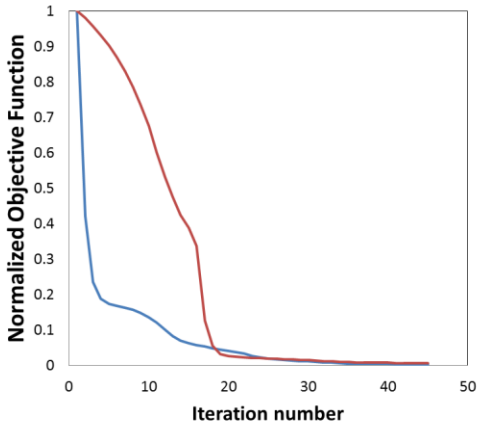

Figure 2.6 Objective function as a function of iterations for a synthetic 2D model. Blue color represents case 1 first integrates the pressure effects followed by the saturation. Red color represents case 2, where integration of saturation changes followed by pressure.

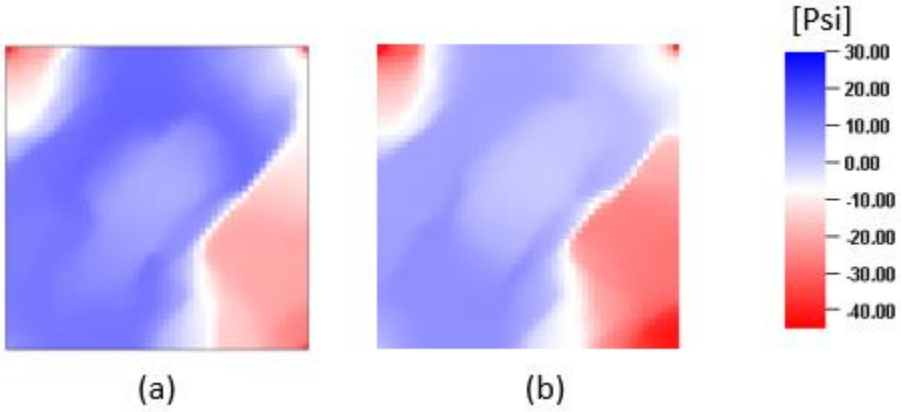

Figure 2.7 Pressure Time-lapse data between 260 days and 1560 days. (a) Case1-first integrates the pressure effects followed by the saturation. (b) Case 2- integration of saturation changes followed by pressure.

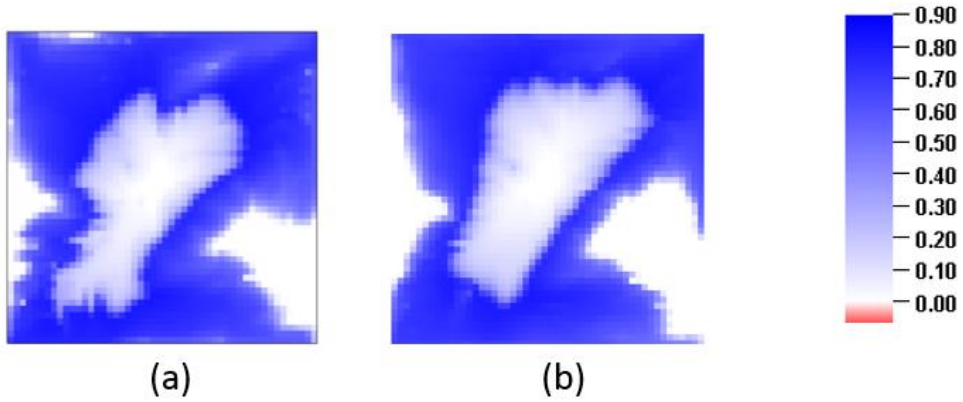

Figure 2.8 Saturation Time-lapse data between 260 days and 1560 days. (a) Case1-first integrates the pressure effects followed by the saturation. (b) Case 2- integration of saturation changes followed by pressure.

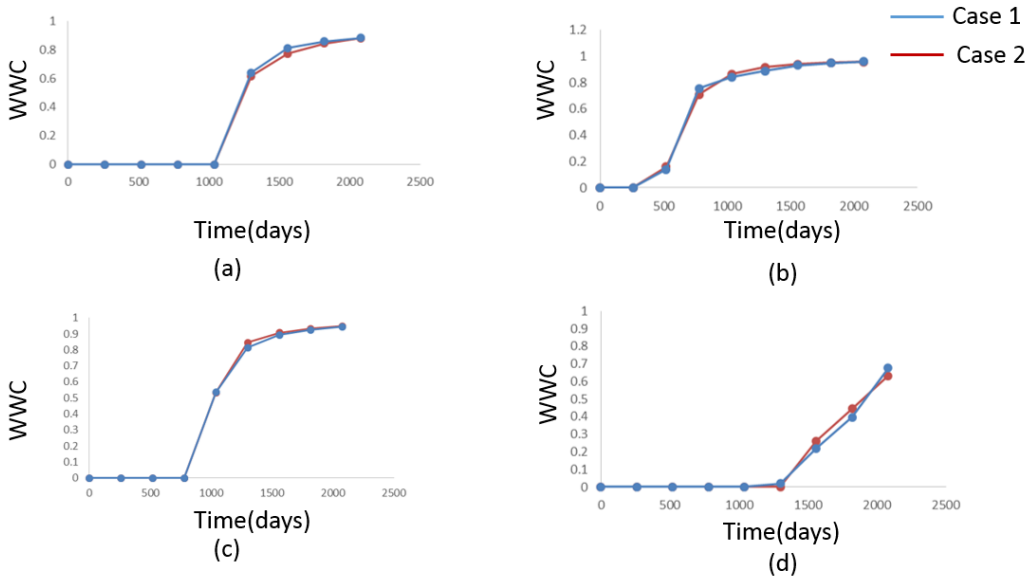

Figure 2.9 Water cut results for the producing wells. Blue line- first integrates the pressure effects followed by the saturation. Red line- integration of saturation changes followed by pressure.

We use the analysis of spatial resolution as a quantitative knowledge to provide insight into our ability (or inability) to estimate our model based on a given set of data. The updates of the permeability models from seismic data for both cases, the associated resolution model, and covariance model are shown in Figure 2.10. Based on the analysis of spatial resolution, both cases appear to identify the low permeability barrier located in the right lower corner of the model. The resolution model, shows high value for those regions, indicating that our estimate is well constrained. The associated covariance model**,** having low values**,** emphasizes the importance of choosing an appropriate truncation level to the trade-off between the covariance and the model resolution. The averaging kernel, for two different cells (case 1), is shown in Figure 2.11**.** We observed that as our resolution value in a specific cell closer to 1, our spatial averaging to infer the permeability in the cell is more constrained. It is of equal importance to indicate the areas where our estimates are poorly constrained. The updated permeability model of case 2 shows two relatively high permeability regions, labeled **A** and **B** in Figure 2.10. The associated model resolution shows low value for those regions, implying that the estimates are poorly constrained and confidence should not be placed on those updates. This post-process analysis is a useful tool for quantifying the nonuniqueness of inversion results in underdetermined problems. It also shows that time-lapse pressure match, followed by a match of the saturation changes, leads to a more constrained estimated model. This sequence is analogous to the structured approach to history matching that is widely practiced in the industry (Williams et al. 1998; Cheng et al. 2008).

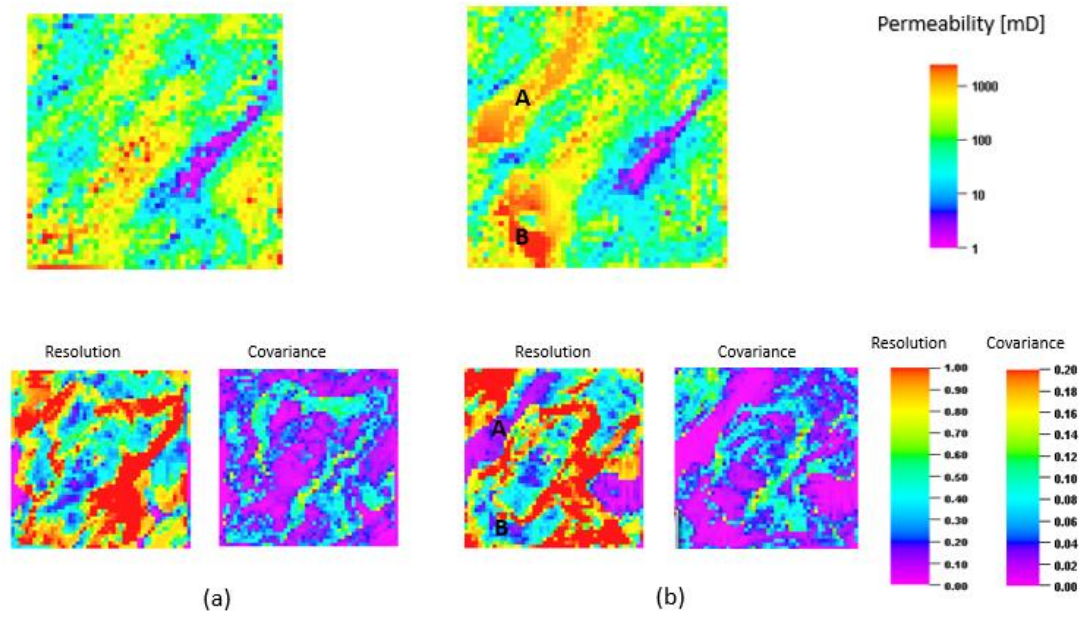

Figure 2.10 Updated permeability field, resolution model and model covariance for the two cases. (a) Case1-first integrates the pressure effects followed by the saturation. (b) Case 2- integration of saturation changes followed by pressure.

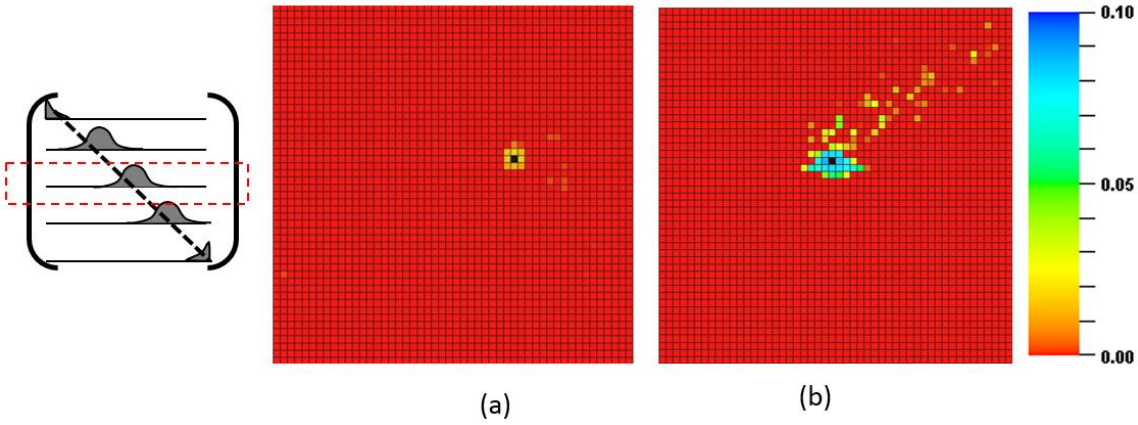

Figure 2.11 Kernel averaging of two different cells (black) in the model. (a) Cell number 1084 with a resolution model value of 0.94 and (b) Cell number 1075 with a resolution model value of 0.6.

Besides being a measure of accuracy and reliability of estimates, model resolution has important significance in determining the relative worth of different data types (Datta-Gupta, 1997). Specifically, we examine the relative contribution of pressure and saturation on integrating the seismic data. Figure 2.12, shows the permeability updated, the associated model resolution, and model covariance after integrating the seismic data with respect to pressure. The cells with high value at the model resolution are associated with the low permeability regions in the updated permeability fields. In our sensitivity calculation, the pressure drop sensitivity for a particular gridblock is the derivative of the pressure drop along the streamline with respect to gridblock permeability. The pressure drop at low-permeability regions is relatively large (Figure 2.5) and makes those gridblocks to be more sensitive to pressure changes. The results seem to imply that pressure better captures the barriers to flow compared to channels to flow.

Next, saturation changes are integrated into the updated model from the pressure updates (Figure 2.13).The saturation changes provides us with complimentary information about the permeability field, particularly in the flow units. It can be seen from Figure 2.13, that those updates reduce some of the overestimated high permeability regions, as we received it from the pressure updates. In addition, it solves some of the unphysical high permeability channels that appear after the pressure updates.
The model resolution shows that integrating both pressure and saturation increases the number of cells that are well constrained in term of our estimation.

Finally, the generalized travel time inversion is applied to match the well- by- well water- cut data as shown in Figure 2.14. The production updates are well suited to capture local variation. Since, in this case, we only have 4 wells, the resolution is poor, and it cannot provide valuable information regarding the relative influence of this type of data. However, when it comes after the seismic data updates, it gives us local changes specifically in the high perm areas. These results show that the resolution of the model can provide us with an efficient tool to know how well our estimated model is. In addition, it points out the importance of accounting for both saturation and pressure changes to constrain the parameter estimation.

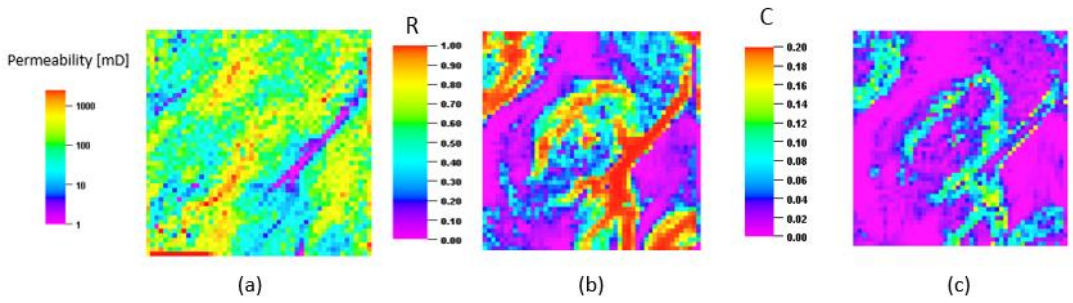

Figure 2.12 Updated permeability field after integrating the seismic pressure changes. (a) Updated model, (b) Resolution model and (c) Model covariance.

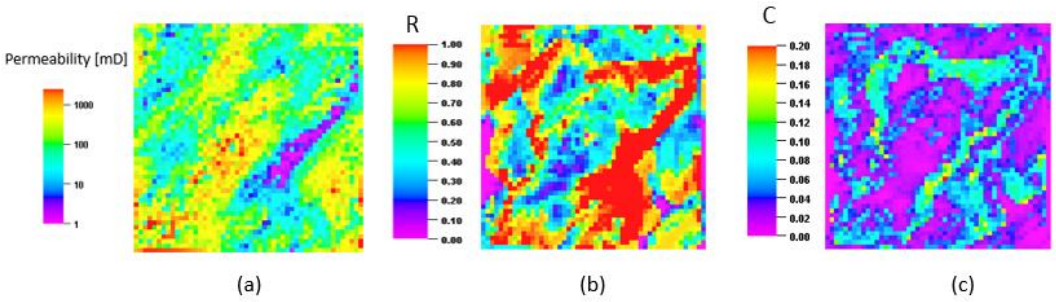

Figure 2.13 Updated permeability field after integrating the seismic pressure and saturation. (a) Updated model, (b) Resolution model and (c) Model covariance.

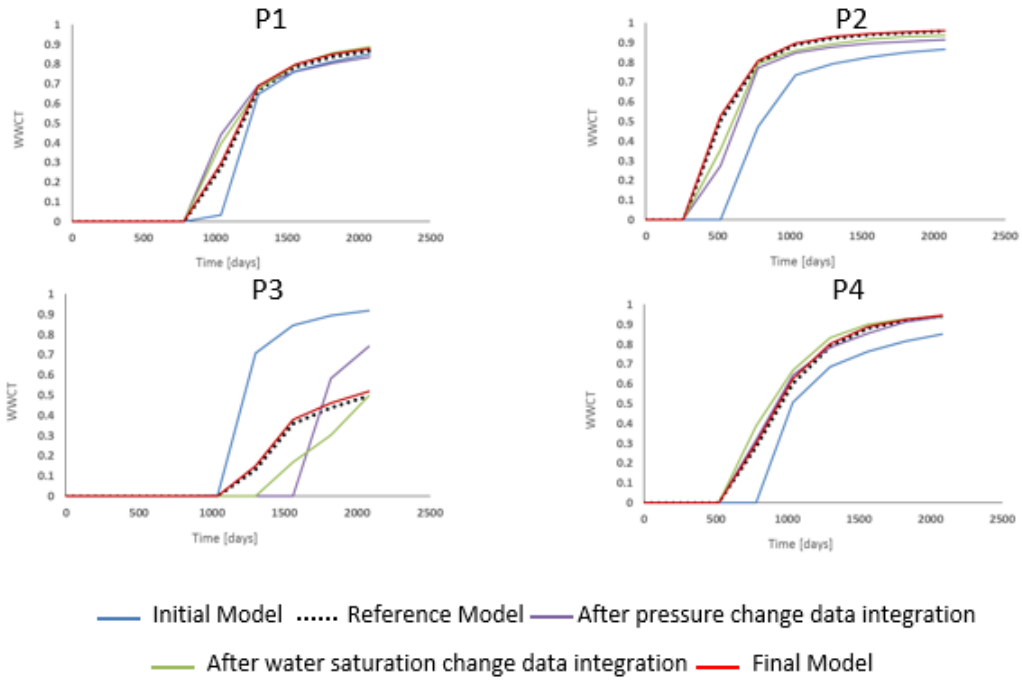

Figure 2.14 Water cut history matching results. Reference model responses are plotted as dot points, initial model responses are in blue lines, model responses after accounting the pressure changes are in purple lines, model responses after accounting the saturation changes are in green lines and final updated model responses are in red lines.

2.4.2 Field Application –The Norne Field Case

The field was discovered in December 1991. Oil production started in November 1997 and gas production in 2001. The faulted reservoir model consists of 44431 active cells and, it has 9 injectors and 27 producers as shown in Figure 2.15. The field has high quality sets of 4-D seismic data (2001-2003, 2003-2004, 2004-2006) and production data used as observation for the history matching process. The production data include water, oil, and gas rates and bottom-hole pressures at the producers. The seismic data provided for the model calibration as near, mid, far, and full offset stacked 3-D volumes of the reflection amplitude together with the corresponding horizons for the top and base of the reservoir. More details of the data set can be found in Rwechungura, R.W. et al. (2012) .

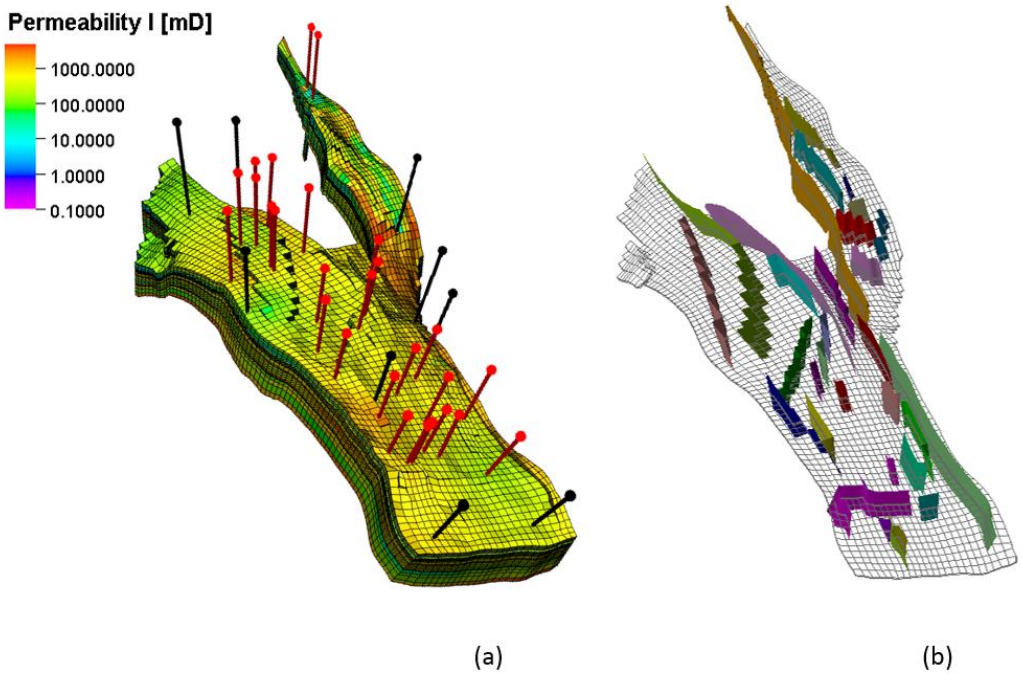

Figure 2.15 Structure of the Norne field. (a) Well locations producers in red, injectors in black, and (b) Internal faults in the reservoir.

A fundamental challenge is to relate the seismic data to the static flow properties in the reservoir simulator. From data integration standpoint, the seismic volumes of reflection has to be inverted from amplitude to changes in acoustic (p-wave) impedance (AI). This process involved a genetic inversion of the seismic amplitude (Veeken et al. 2009).
In this work only near-offset stacking data set has been used, because the acoustic (p-wave) impedance changes are more evident in the small angle reflection waves in AVO analysis (Aki and Richards 2002) .Using commercial software, we conduct seismic data processing which consists of (1) time to depth data conversion, (2) well log quality

check and acoustic impedance log calculation, and (3) genetic inversion for generating an acoustic impedance map from the seismic amplitude data. Figure 2.16 shows the observe seismic data as a change in the AI for each time-lapse in different layers in the model. Further details about the seismic data processing can be found in Watanabe et al. (2017).

From a reservoir simulation point of view, we must rely on a petro-elastic model to relate the static and the dynamic response of the reservoir (pore volume, pore fluid saturations, reservoir pressures and rock composition) to seismic rock elastic parameters (the seismic wave's velocity). We adopt the Gassmans equation (1951) and Hertz-Mindlin contact theory (Mindlin, 1949) to account for the changes in the elastic parameters caused by fluid saturation and reservoir pressure variations.

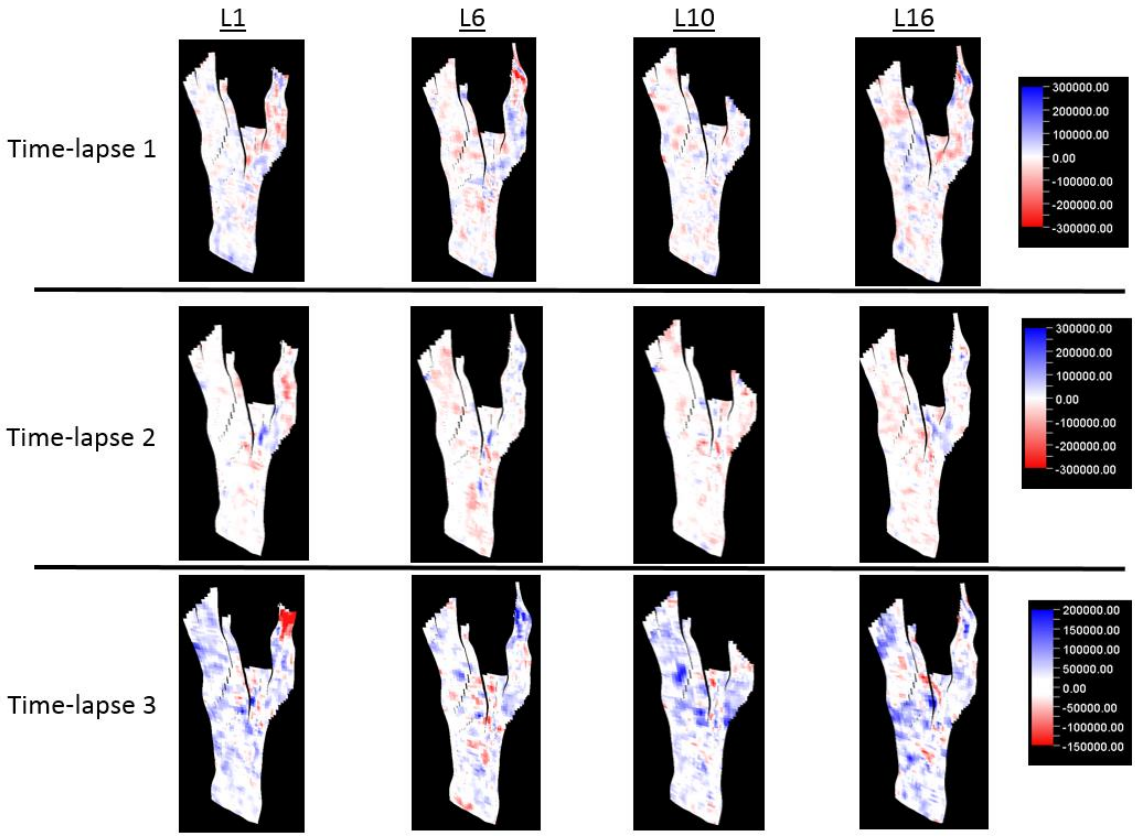

Figure 2.16 The observed seismic data as a change in the AI for selected layers in the model.

Table 2.3 Input parameters for petro-elastic model-Norne Field

Send properties			
Garn Formation (layer1-3)	Frame bulk modulus,Gpa	K_{fr}	18.8-36.8 φ
	Frame shear modulus,Gpa	G_{fr}	11.8-21.4 φ
	Matrix bulk modulus,Gpa	K_{ma}	37
	Matrix density, kg/m³	ρ_{ma}	2650
Garn Formation (layer 5-22)	Frame bulk modulus,Gpa	K_{fr}	18.5-27.4φ
	Frame shear modulus,Gpa	G_{fr}	10.9-13.0 φ
	Matrix bulk modulus,Gpa	K_{ma}	37
	Matrix density, kg/m³	ρ_{ma}	2650
Fluid properties			
Fluid bulk modulus	Oil bulk modulus, Gpa	K_o	1.35
	Water bulk modulus, Gpa	K_w	2.79
	Gas bulk modulus, Gpa	K_g	6.49x10-2
Fluid density	Oil density ,kg/m³	ρ_o	860
	water density ,kg/m³	ρ_w	1000
	Gas density ,kg/kg/m³	ρ_g	190

The Hertz-Mindlin model to relate the seismic rock elastic parameter to pressure changes (Mavko et al, 1998)

$$K_{\mathrm{HM}} = K_{\mathrm{ma}} \sqrt[n]{P_{\mathrm{eff}} / \left(P_{\mathrm{ext}} - P_{\mathrm{i}}\right)}, \tag{2.38}$$

where K_{HM} is the bulk modulus at critical porosity (Dadashpour 2009, 2010) and K_{ma} is the bulk modulus of the matrix. P_{eff} is the effective pressure, P_{ext} is lithostatic pressure which depends upon on the true vertical depth (TVD) , as can be seen in **Eq.38** and p_i is the initial pressure , here set to 270 [bar.] n is the coordination number set up to be 5 in this study, the effective pressure is given as

$$P_{\text{ext}} = 0.0981.\left(9\times10^{-5}\times\text{TVD}+1.7252\right)\times\text{TVD}\,. \tag{2.39}$$

The Gassmann's equation (1951) is adopted to relate the bulk modulus of the fluid saturated rock.

$$K_{\text{sat}} = K_{\text{fr}} + \frac{\left(K_{\text{HM}} - K_{\text{fr}}\right)^2}{K_{\text{HM}}\left(1-\phi+\phi\dfrac{K_{\text{HM}}}{K_{\text{f}}}-\dfrac{K_{\text{fr}}}{K_{\text{HM}}}\right)}, \tag{2.40}$$

where ϕ is the effective porosity of the medium and the bulk modulus of the pore fluids (oil, water, and gas). K_{HM} is the bulk modulus of the mineral matrix calculated from **Eq.38,** K_{fr} is the bulk modulus of the porous rock frame and K_{f} is the bulk modulus of the pore-filling fluids.We consider the lower bound on the moduli given as (Reuss, 1929)

$$\frac{1}{K_{\text{f}}} = \frac{S_{\text{o}}}{K_{\text{o}}} + \frac{S_{\text{w}}}{K_{\text{w}}} + \frac{S_{\text{g}}}{K_{\text{g}}}\,. \tag{2.41}$$

Here S_{o}, S_{w} and S_{g} are oil, water and gas saturations, respectively, and K_{o}, K_{w}, and K_{g} are bulk moduli for oil, water, and gas, respectively. The physical meaning of using that bound is that the compression is in a direction perpendicular to layers of pure components. Then, the weakest layer determines the modulus (Vasco et al. 2014). This will be discussed in more details in the next chapter. Table 2.3 summarizes the rock elastic properties. The density of the saturated rock is given by the weighted average of the densities of the components

$$\rho_{\text{sat}} = \left(1-\phi\right)\rho_{\text{ma}} + \phi\left(S_{\text{o}}\rho_{\text{o}} + S_{\text{w}}\rho_{\text{w}} + S_{\text{g}}\rho_{\text{g}}\right), \tag{2.42}$$

where ρ_o, ρ_w, ρ_g and ρ_{ma} are the densities of oil, water, gas and the rock matrix, respectively. The compressional (p-wave) velocity can be calculated by using the saturated rock bulk modulus, and the shear modulus G_{fr}, which is not affected by fluid saturations and density. Given as (Kennett 2013)

$$V_p = \sqrt{\frac{K_{sat} + \frac{4}{3}G_{fr}}{\rho_{sat}}}. \tag{2.43}$$

The acoustic impedance can be computed as

$$Z_p = \rho_{sat} V_p = \sqrt{\rho_{sat}\left(K_{sat} + \frac{4}{3}G_{fr}\right)}, \tag{2.44}$$

2.4.2.1 Sensitivity of the Acoustic Impedance with Respect to Permeability

In this section we relate the changes in the acoustic impedance to the changes in the grid block permeability. We assume that changes in porosity because of compaction in **Eq.6** are not significant. As demonstrated in the previous section, the PEM is depended on the pressure and saturation. By implementing the chain rule we can generate the sensitivity of the acoustic impedance with respect to grid block permeability as.

$$S_{Z_p} = \frac{\delta d_{Z_p}}{\delta k} = \left[\frac{\partial Z_p}{\partial S_w}\frac{\delta S_w}{\delta k} + \frac{\partial Z_p}{\partial S_g}\frac{\delta S_g}{\delta k} + \frac{\partial Z_p}{\partial P}\frac{\delta P}{\delta k}\right], \tag{2.45}$$

Here the partial derivatives of acoustic impedance, $\frac{\partial Z_p}{\partial S_w}, \frac{\partial Z_p}{\partial S_g}, \frac{\partial Z_p}{\partial P}$ are computed by numerical perturbation from the current saturation and pressure grid block values using **Eq. 45**, and water saturation sensitivity and pressure drop sensitivity are computed by

Eq. 18 and **Eq. 26**, respectively. The gas saturation sensitivity is calculated using the same equation as we use for the water

$$\frac{\delta S_s(\tau,t)}{\delta k(x)} = -\frac{t}{\tau}\frac{S_s(\tau,t)-S_s(\tau,t-\Delta t)}{\Delta t}\frac{\delta \tau}{\delta k(x)}, \tag{2.46}$$

2.4.2.2 Norne Field –History Matching and Analysis of Spatial Resolution

Our objective is to update the permeability model using the streamline based sensitivity and to indicate the reliability of our updated model by applying the analysis of spatial resolution. The data integration is consistent with the synthetic cases. First, the AI changes with respect to pressure changes are collaborated into the model, then AI changes with respect to saturation changes of water and gas are integrated into the model. For each level of the data integration, an analysis of the spatial resolution has been performed. Figure 2.17 shows the observed, the initial and the updated AI changes maps for different times in different layers. Overall, the misfit associated with the time-lapse acoustic impedance change are reduced from the initial misfit calculated using the prior model. At the same time, we can clearly see the effect of the second term in **Eq.27** (norm penalty), that penalizes deviations from the prior model.

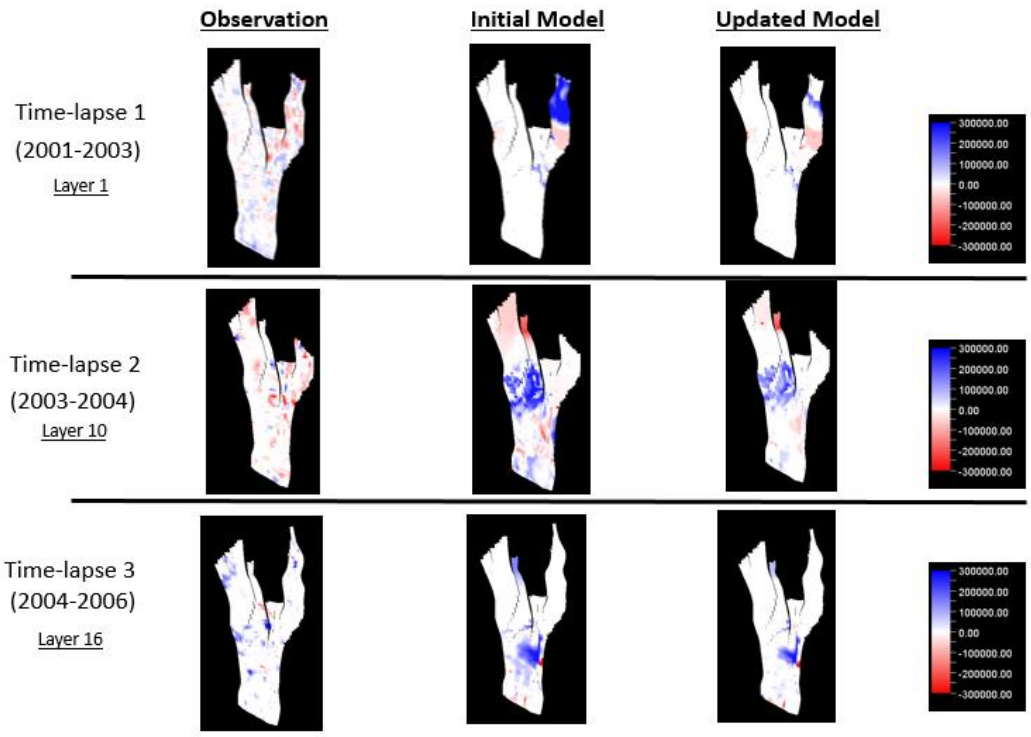

Figure 2.17 The acoustic impedance changes for selected layers.

Figure 2.18 shows the permeability field, the associated resolution model and covariance model for seismic calibration based on pressure change between 2001 and 2003 for different layers. Figure 2.19 shows the permeability field, the associated resolution model and covariance model for seismic calibration based on saturation change between 2001 and 2003 for different layers. The resolution model clearly determines the regions that are more constrained to the physics that is followed (e.g. pressure, saturation). For example, in layer 1 the north right part of the reservoir (Figure 2.18**)**, the updated model is more constrained when calibrating the AI changes with respect to pressure. On the other hand, Figure 2.19 shows that the seismic integration is more constrained at the

bottom part of the reservoir (layer 10 and 16), when calibrating the AI changes with respect to saturation.

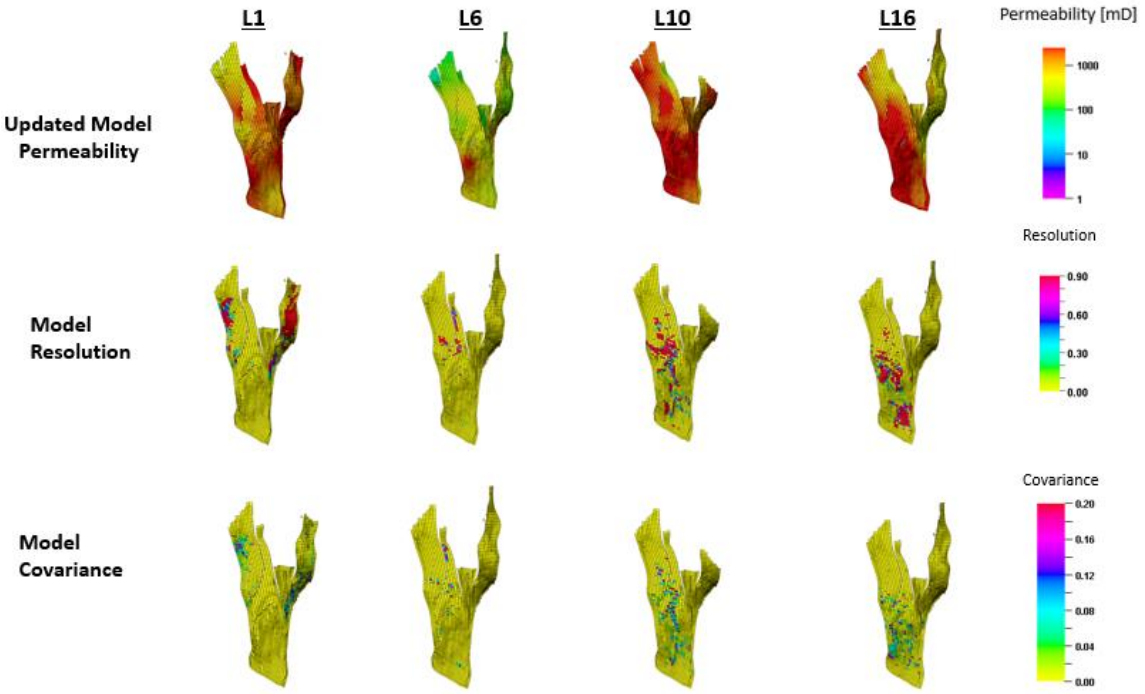

Figure 2.18 The updated permeability model, the model resolution and the model covariance in selected layers, after integrating the seismic data (2001-2003) with respect to pressure.

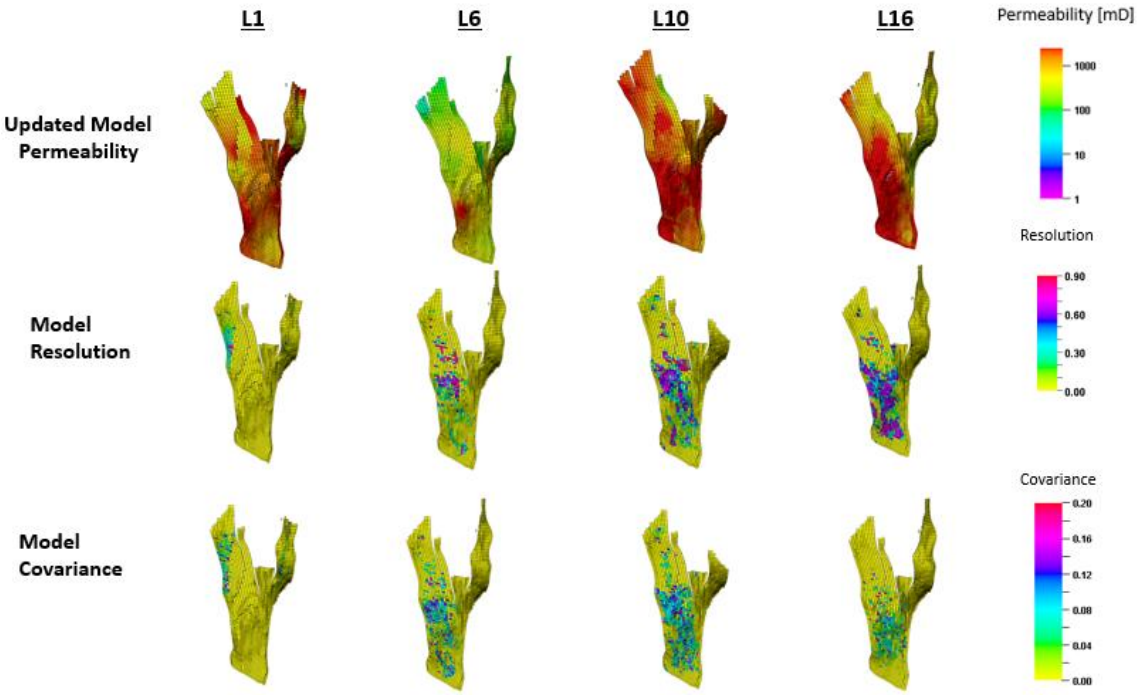

Figure 2.19 The updated permeability model, the model resolution and the model covariance in selected layers, after integrating the seismic data (2001-2003) with respect saturation.

Figure 2.20 demonstrates how one can use the analysis of spatial resolution to provide insight into our ability to estimate our model based on a given set of data. Specifically, we plot the permeability changes and the associated resolution model. The high value is seen at the north right part of the reservoir in the resolution plat, suggesting that the associated permeability updates with those cells are well constrained and more confidence should be placed there. These updates also leads to a significant reduction in the acoustic impedance change data misfit as shown in Figure 2.16. Contrarily, poor resolution regions indicate that the local permeability cannot be resolved as the degree of averaging associated with our estimates becomes larger and caution must be exercised.

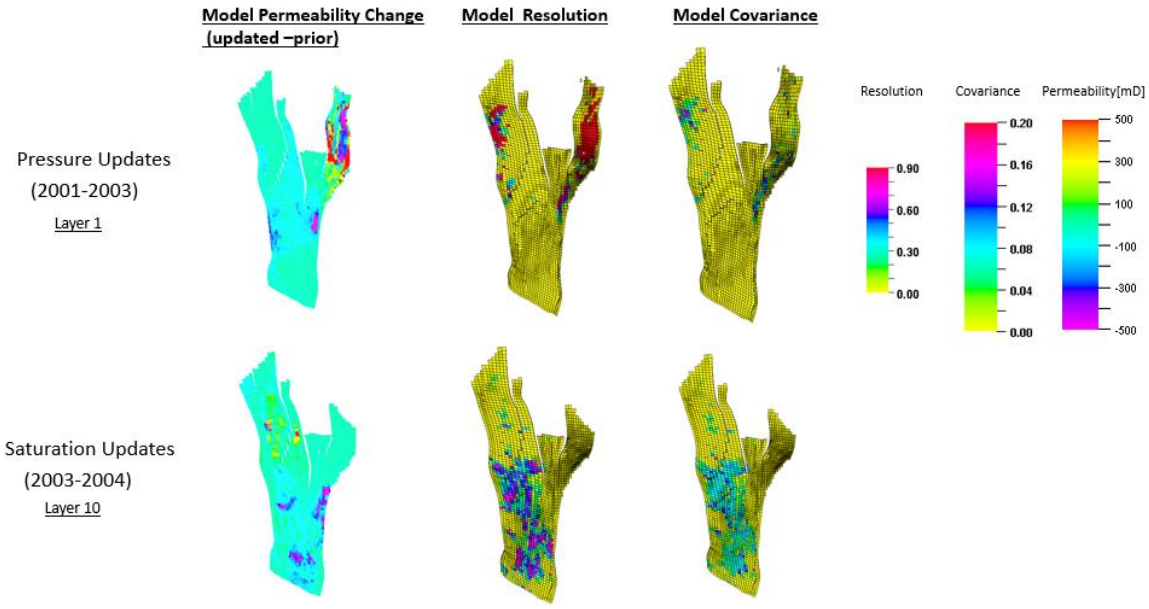

Figure 2.20 Permeability model change, resolution model and covariance model for selected layers. Seismic data is integrated with respect to pressure (Top), and Seismic data is integrated with respect to saturation

The analysis of spatial resolution also provides valuable information regarding the relative influence of the pressure and the saturation in our sequential data integration. Figure 2.21 shows the permeability field, and the associated resolution model for pressure and saturation updates. In particular, within the red dash line, it can be seen that the pressure appears to better resolve the barriers to the flow (low-permeability and faults), where the saturation provides a complimentary information about reservoir quality inside the flow units.

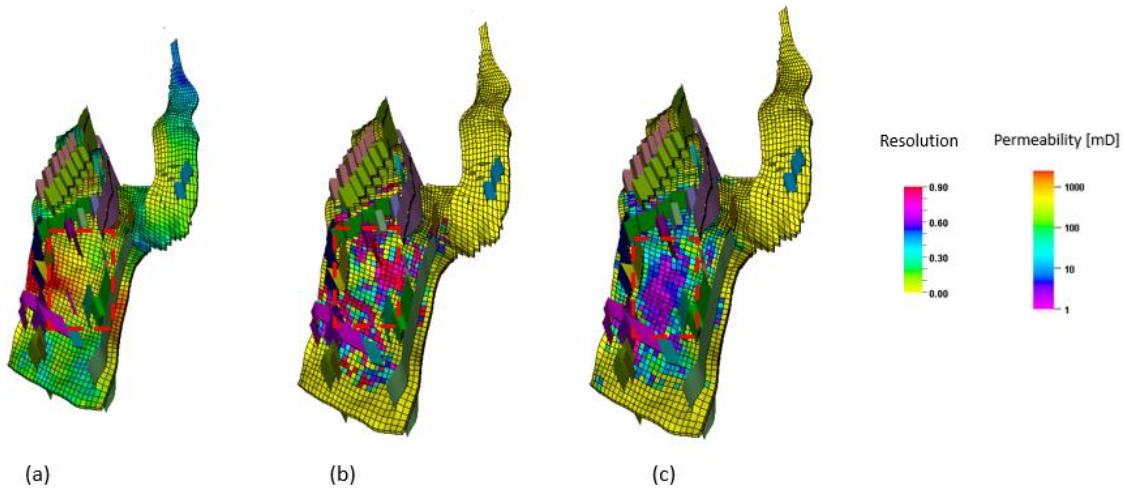

Figure 2.21 A resolution model comparison of pressure and saturation between 2004-2006 in layer 14. (a) Updated permeability field, (b) Model resolution of partial derivative of AI with respect to pressure, and (c) Model resolution of partial derivative of AI with respect to saturation

2.5 Chapter Conclusions

In this chapter, we described a method to quantify the resolution and the spatial averaging associated with estimated permeabilities derived through an efficient history matching approach of multi-scale data integration, accounting for both pressure and saturation effects. By applying techniques from geophysical inverse theory, we demonstrated how one can assess the ability of seismic and production data to constrain permeability variations in heterogeneous porous media and assessing the inversion results in underdetermined problems.

In seismic data, the spatial resolution points out the importance of accounting for both saturation and pressure changes to constrain the parameter estimation. However, the saturation and pressure changes within a reservoir are not the only factors that affect the

relationship between the reservoir properties and the variations in geophysical properties. The analysis presented here, shows the contribution of the saturation and pressure changes in to our estimated model. It appears that pressure is more sensitive to barriers to flow in global, whereas in the flow unit the barriers to flow and small variations in permeability are better determined by saturation. Based on the model resolution and the results of all cases, it seems that the low permeability areas in the high permeability zones are the locations where the most confidence should be placed. In practice, assessing the estimated model using the approach presented here, provides us with a cell-by-cell information about the quality of the estimation constraint. In history matching, when the problem is highly underdetermined, this information is as critical as the estimated value itself.

CHAPTER III

INTEGRATION OF TIME LAPSE SEISMIC DATA INTO RESERVOIR MODELS USING ONSET TIMES*

3.1 Chapter Summary

In this chapter, we present a novel and efficient approach to integrate frequent time lapse (4D) seismic data into high resolution reservoir models based on seismic onset times, defined as the calendar time when the seismic attribute crosses a pre-specified threshold value at a given location. Our approach reduces multiple time-lapse seismic survey data into a single map of onset times, leading to substantial data reduction for history matching while capturing all relevant information regarding fluid flow in the reservoir. Hence, the proposed approach is particularly well suited when frequent seismic surveys are available using permanently embedded sensors.

Our history matching workflow consists of two stages: global and local. At the global stage of history matching, large-scale features such as regional permeabilities, pore volumes, temperature and fluid saturations are adjusted to match seismic and bottomhole pressure data using a Pareto-based multi-objective history matching workflow. Rather than an artificial subdivision of the domain, the history matching regions are naturally defined based on an eigen-decomposition of the grid Laplacian and a spectral clustering

---

* * Part of this section is reprinted with permission from "History Matching of Frequent Seismic Surveys Using Seismic Onset Times at the Peace River Field, Canada" by G. Hetz, H. Kim, A. Datta-gupta, M.J. King, J.K. Przybysz-Jarnut, J.L. Lopez, D. Vasco, , 2017. Paper 187310 prepared for presentation at the SPE Annual Technical Conference and Exhibition held in San Antonio, Texas, USA, 7 October –12 October.

of the second eigenvector (fiedler vector). The global updating is followed by local history matching whereby cell permeabilities are adjusted to further refine the history match using semi-analytic, streamline-based model parameter sensitivities. The power and efficacy of our proposed approach is illustrated using synthetic and field applications.

The field example involves steam injection into a heavy oil reservoir at Pad 31 in the Peace River Field (Alberta, Canada) with daily time lapse seismic surveys recorded by a permanently buried seismic monitoring system(Lopez et al. 2015). In our specific application, we have used time lapse data (in terms of two-way travel time) from a Cyclic Steam Stimulation (CSS) cycle in the pad with a total of 175 seismic surveys. With a single onset time map derived from this data we were able to capture the propagation of pressure and saturation fronts and significantly improve the dynamic model through the estimation of permeability distribution, fluid saturation evolution and swept volume. With this methodology we correctly identified and further refined the location of stimulated zones as inferred before from reservoir engineering judgement and manual adjustments aiding better understanding of CSS behavior in the studied field. The results clearly demonstrate the effectiveness of the onset time approach for integrating large number of seismic surveys by compressing them into a single map. Also, the onset times appear to be relatively insensitive to the petro elastic model but sensitive to the steam/fluid propagation, making it a robust method for history matching of time lapse surveys.

3.2 Introduction

Reservoir monitoring is an integral part of reservoir management during enhanced oil recovery, where for example, steam (Eastwood et al. 1994) and CO_2 (Arts et al. 2000) are injected, to ensure injectant conformance and flood front management, maximizing recovery and minimizing operational costs. The availability of dense areal information from frequent 4D seismic offers a great opportunity to achieve these goals. It enables better understanding of reservoir sweep and flow patterns, reduction of the uncertainty in the reservoir properties and adjustment of the operational strategy to restore conformance and optimize recovery (Foster 2007; Przybysz-Jarnut et al. 2015; Watanabe et al. 2017). However, it also poses new challenges in terms of dynamic reservoir modeling and seismic history matching to infer changes in the state of the reservoir. The underlying issues for successful monitoring of reservoir fluid-flow systems using time-lapse data were reviewed by Lumley (2001) and Behrens et al. (2002).

Traditionally, time-lapse seismic techniques for inferring flow properties have been focused on amplitude, traveltime, and waveform changes. For example, Tura and Lumey (1999) and Landrø et al. (2001) used the inverted seismic responses and amplitude versus offset inversion to discriminate between the pressure and saturation changes. Arenas et al. (2001) used the compressional velocity to calibrate the permeability field. Vasco et al. (2005) used reflection amplitude to update the flow properties, where the sensitivity of seismic amplitude is analytically computed. (Dadashpour, M. et al. 2010; Dadashpour et al. 2009; Dadashpour et al. 2008) applied

the propagator-matrix method (Stovas and Arntsen 2006) to generate the seismic traces from a stack of plane layers and calibrate reservoir properties by a Gauss-Newton optimization technique. Rey et al. (2012) applied a streamline-based sensitivity calculation to integrate the seismically derived water saturation changes and the acoustic impedance differences and demonstrated field-scale applications. Watanabe et al. (2017) used the time-lapse changes in acoustic impedance to update grid cell permeability with a hierarchical approach involving global and local updates.

Although such methods can often detect changes in geophysical quantities and were successfully applied to field cases, relating geophysical changes to quantified changes in the fluid flow properties remains a fundamental challenge (Vasco et al. 2014). The connection between the current state of the reservoir and the geophysical observations relies on underlying rock physics model that can have considerable uncertainty. One of the main uncertainties comes from the fact that these models are built based on laboratory measurements that may not be representative of the field conditions. This makes seismic history matching difficult as the estimation results highly depend on the saturation mapping chosen and can be quite different, while originating from the same seismic measurement. Another difficulty is integrating the data from Permanent Reservoir Monitoring systems (PRM), where tens to hundreds time-lapse seismic surveys may be available.

To deal with the above-mentioned issues we present a novel and computationally efficient approach for frequent time lapse seismic integration using the concept of onset time (Vasco et al. 2015; Vasco et al. 2014). The onset times are defined as the calendar

times at which geophysical observations begin to deviate from their initial or background values above a pre-defined threshold value. It allows compression of multiple seismic surveys into a single map of front propagation, which can be used to effectively guide history matching and for dynamic model updating. The onset time can be related to the arrival time of a particular physical phenomenon (e.g. saturation front and/or pressure front). We demonstrate the power and the utility of the onset time methodology for history matching using synthetic study and field application. In the first instance, we compare the traditional seismic integration based on matching the magnitudes of seismic observations with the onset time approach. The second example involves steam injection into a heavy oil reservoir at Pad 31 in the Peace River Field (Alberta, Canada) with daily time lapse seismic surveys (in terms of two-way travel time) recorded by a permanently buried seismic monitoring system. We update our model based on onset time derived from the continuous seismic land monitoring using a hierarchical approach involving global and local updates.

3.3 Approach

In this section, we introduce our proposed approach of integrating time lapse seismic into the reservoir model using onset-times. We start with an explanation of the data integration workflow and illustrate the concept of onset time in a stepwise manner using a simple synthetic example.

3.3.1 From Multiple Surveys to a Single Map of Onset-times

The traditional approach to time lapse seismic data integration uses multiple seismic surveys and integrates seismic attributes (amplitudes or travel times) or changes thereof via dynamic modelling and history matching. In contrast, the onset time methodology collapses multiple seismic surveys into a single map of changes propagating in the reservoir. The onset times (Vasco et al. 2015) are defined as the calendar times at which measured time-lapse attributes begin to deviate from their initial values above a pre-defined threshold value. The magnitude and sign of the threshold value depends on the signal-to-noise ratio of the seismic dataset and the particular physical phenomenon that is being tracked (e.g. saturation front and/or pressure front).

3.3.2 Time Lapse Seismic Data and Petro Elastic Model (PEM)

In order to connect between the state of the reservoir and the geophysical observation, we have to rely on a PEM to calculate the elastic properties of the rock that vary in time as a result of changes in the dynamic reservoir properties: fluid saturations, reservoir pressure, and temperature etc. The relationship between the seismic properties and the rock elastic properties can often be described by Gassmann's equations (Gassmann 1951) for calculating the effective bulk modulus of the entire saturated rock. The model relates the bulk modulus of a rock to its pore, frame, and fluid properties. The Gassmann's relation is valid in most practical cases; however, it can have considerable uncertainty, particularly in the model used to describe how the fluids are arranged within the pore space. The onset time, as opposed to magnitude matching, seems to be

insensitive to the specific model used for mapping the fluid saturations (Vasco et al. 2015), and thus more robust against uncertainties in the underlying rock physics model.

3.4 Background and Methodology

In this section, we relate the onset time of time lapse seismic to the flow properties. Our inversion approach relies on the use of streamlines to relate small changes in reservoir properties to variations in the time lapse seismic response. Establishing these relationships, known as sensitivities, is crucial to the data integration process. The streamline approach allows us to derive analytical relationship between the arrival time of a propagating front in the reservoir and the flow properties, e.g., porosity and permeability, through which the propagation front traverses (Vasco et al. 2014). While the concept of the streamline method discussed in details in the previous chapter, here we focus on relating the onset of a change in a time-lapse attribute to the flow properties of a porous medium.

3.4.1 Time Lapse Seismic and Onset Time Sensitivity Calculation

In order to connect the dynamic responses of the simulator to the seismic observations, we need to translate the former into seismic domain using a rock-physics model. A petro-elastic model is a set of equations relating reservoir properties (pore volume, pore fluid saturations, reservoir pressures and rock composition) to seismic rock elastic parameters (P -wave and S-wave velocities, V_p and V_s , respectively).

The Gassmans equation (1951) is adapted to estimate the changes in elastic parameter caused by fluid substitution and reservoir pressure variations.

$$K_{\text{sat}} = K_{\text{fr}} + \frac{\left(K_{\text{HM}} - K_{\text{fr}}\right)^2}{K_{\text{HM}}\left(1-\phi+\phi\frac{K_{\text{HM}}}{K_{\text{f}}}-\frac{K_{\text{fr}}}{K_{\text{HM}}}\right)}. \tag{3.1}$$

K_{fr} is the bulk modulus of the porous rock frame, ϕ is the effective porosity of the medium and the bulk modulus of the pore fluid, the bulk modulus of the mineral matrix K_{HM} is calculated based on Hertz-Mindlin contact theory (Mindlin 1949), and K_{f} is the bulk modulus of the pore-filling fluids.

In order to calculate K_{f} we need to specify (1) the volume fraction of the phases, (2) the elastic moduli of the various phases, and (3)how the fluids are arranged relative to each other within the porous medium (Mavko et al. 2009). From the simulation response and the PEM, we can specify only the volume fractions and the constituent moduli. Currently, there is no universally accepted method of saturations mapping for an arbitrary distribution of fluids within the reservoir (Vasco et al. 2015). In such a case, one can only predict the upper and the lower bounds to describe the bulk modulus of the pore-filling fluids. The Reuss lower bound is given by

$$K_f^{Reuss} = \left(\sum_{i=1}^{N}\frac{S_i}{K_i}\right)^{-1}, \tag{3.2}$$

where S_i is the saturation of the i-th fluid and K_i is the bulk modulus of the i-th fluid. This bound can represent a scenario where the gas saturation is homogeneous distributed and determines the modulus. This curve (Figure 3.1) is achieved when the fluid phases are mixed at the finest scales and the seismic wave velocity is a nonlinear function of the gas saturation (Mavko et al. 1998).

On the other hand, the Voigt upper bound is used to describe a case where the gas saturation is spatially nonuniform and given by

$$K_f^{Voigt} = \left(\sum_{i=1}^{N} S_i * K_i \right). \tag{3.3}$$

This model (blue curve in Figure 3.1**)** predicts a monotonic, almost linear increase in velocity from the dry to saturated values. It is achieved when there is the greatest separation of phases. Within this framework, at any given volume fraction of constituents, the bulk modulus of the pore-filling fluids will fall between the upper and the lower bounds. For example, the Hill estimate of the fluid bulk modulus (Mavko et al. 2009) is the arithmetic average of the Voight and Reuss bounds

$$K_f^{Hill} = \frac{K_f^{Voigt} + K_f^{Reuss}}{2}, \tag{3.4}$$

which represents a certain scenario of linear interpolation between the models to obtain different curves of saturations mapping (green curve in Figure 3.1).

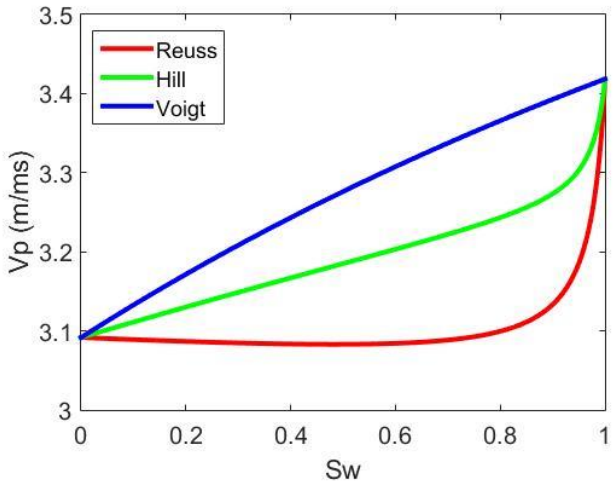

Figure 3.1 The velocity of a compressional wave as a function of the saturations for different models to describe the bulk modulus of the pore-filling fluids.

Vasco et al. (2015) showed that the onset time, as opposed to the time-lapse amplitude, is less sensitive to varying between the upper and the lower bounds. In this study, we also explore the onset time response with respect to the specific method used to map the saturation. This will be discussed in more detail in the applications. We use **Eq.2.42** to calculate the density of the saturated rock. The compressional (p-wave) velocity is generated using **Eq. 2.43** and the acoustic (p-wave) impedance is computed using **Eq. 2.44**.

In the previous chapter, we have shown how the streamlines approach can be used to compute sensitivities relating perturbations in flow properties to perturbations in saturation changes. Assuming onset time to be function of fluid saturation and pressure and implementing the chain rule, we can generate the sensitivity of the onset time with respect to permeability at a given location using the differential form of Eq**. 2.44** as

$$G_{OT_p} = \frac{\delta d_{OT}}{\delta k} = \left[\frac{\partial \mathrm{OT}}{\partial S_w} \frac{\delta S_w}{\delta k} + \frac{\partial \mathrm{OT}}{\partial S_g} \frac{\delta S_g}{\delta k} + \frac{\partial \mathrm{OT}}{\partial \mathrm{P}} \frac{\delta \mathrm{P}}{\delta k} \right]. \tag{3.5}$$

In this research, we study waterflooded and steam injected reservoirs where our focus is on water/steam front movement and therefore consider only the contribution of the changes in water front movement to the changes in onset time. In general, the seismic attribute depends upon coupling deferent physical phenomenon however, the fact that we use a threshold to define the onset time allows us to decuple those physics. In particular, the magnitude and sign of the threshold value depends on the signal to noise ratio of the seismic dataset and a particular physical phenomenon that is being tracked. In the above equation, the partial derivatives of onset times(OT), $\partial \mathrm{OT} / \partial S_w$ is computed by numerical perturbation from the current saturation grid block values using **Eq. 2.44**, and saturation sensitivity $\partial S_w / \partial k$ is computed by **Eq. 2.17**.

3.5 Application

3.5.1 Five –Spot Synthetic Case

We first illustrate the major steps involved in the onset time data integration procedure using a two-dimensional synthetic application. The model is composed of a 50

x 50 grid of cells and involves reservoir production in a 5-spot pattern with four producers located at the corners and one central injector. The description of the model is given in section 2.4.1. The observed 4D seismic data were generated from the permeability model using a commercial reservoir simulator and a petro-elastic model. Over an interval of 2080 days, a total of 8 time-lapse seismic surveys (260 days each) in the form of acoustic impedance maps, are available for integration.

In our onset time approach, the first step is to define a threshold value that allows a meaningful conversion of multiple attribute maps to a single map of onset time. The pre-defined threshold has two main roles: (1) to ensure that the magnitude of seismic observation is above the noise level, which determines the value of the threshold, (2) to define the physical phenomenon that is being tracked, which specifies the sign of the threshold value. Time-lapse seismic data are typically noisy due to non-repeatable noise, environmental noises, sensors spacing, and changes in near surface propagation due to variations in the water table or in the overlying water column. These variations lead to seismic signals even when there are no dynamic changes within the reservoir, and thus a need for threshold value to distinguish between noise and meaningful signal. In this example, we define the threshold to be 5% above the acoustic impedance of the baseline survey (that is, before the injection started). This increase above the threshold corresponds to an increase in the bulk density and velocity of the seismic waves, which results from replacement of "softer" for "harder" reservoir fluids (e.g. oil or gas being displaced by the injected water). Figure 3.2 illustrates the procedure of converting the time-lapse magnitude data to onset time map. For each cell in our model we indicate the

calendar time at which the measured time-lapse amplitude data crosses the threshold value. This time (day), will be recorded in the onset time map. Thus, data from multiple attribute maps reduce to a single onset time map **(**Figure 3.2C**)**. The contours of the onset time provide a display of the changes propagating in the reservoir.

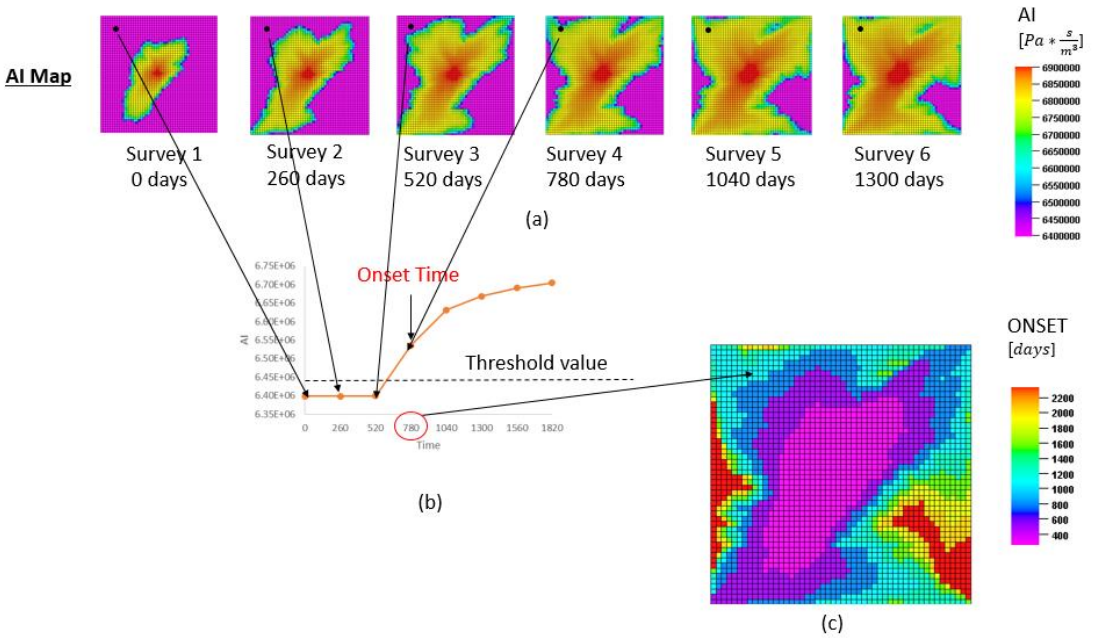

Figure 3.2 Conversion of multiple attribute maps (AI) to onset time map. (a) A sample of 6 attribute maps (AI) out of 8 that are available for integration.(b) A plot of the seismic response of a specific cell (black dot in (a)) to indicate the onset time. (c) The onset time map after converting from seismic attribute to time. The contours display the front progression.

To examine the sensitivity of the onset time to the PEM, we consider two sets of observations. In the first set, the acoustic impedance maps were calculated using the Reuss lower bound (**Eq.3.2**) to describe the bulk modulus of the pore-filling fluids. In

the second set, the acoustic impedance maps were calculated using the Voigt upper bound (**Eq.3.3**) to describe the bulk modulus of the pore-filling fluids. As indicated above, the velocity changes resulting from the saturation changes will vary, depending upon the specific bound we use to describe the bulk modulus of the pore-filling fluids. For each data set, we convert the multiple attribute maps (e.g. acoustic impedance) to an onset time map. Figure 3.3 shows the seismic response as a function of the method we use to describe the bulk modulus. In particular, in Figure 3.3a and Figure 3.3b we plot the acoustic impedance amplitude changes over the interval for both cases. The acoustic impedance amplitude changes seems to be very sensitive to the selected averaging method that we use to describe the bulk modulus of the pore-filling fluids. On the other hand, the onset times (Figure 3.3c and Figure 3.3d) appear to be relatively insensitive to the model used to estimate the fluid bulk moduli. Figure 3.4 shows the AI amplitude over the injection interval for two points in the model. There are clear differences in the magnitudes of the calculated amplitude changes depending upon which averaging technique is used. However the onset time is consisted for both bounds. Similar conclusions were arrived by Vasco et.al (2015).

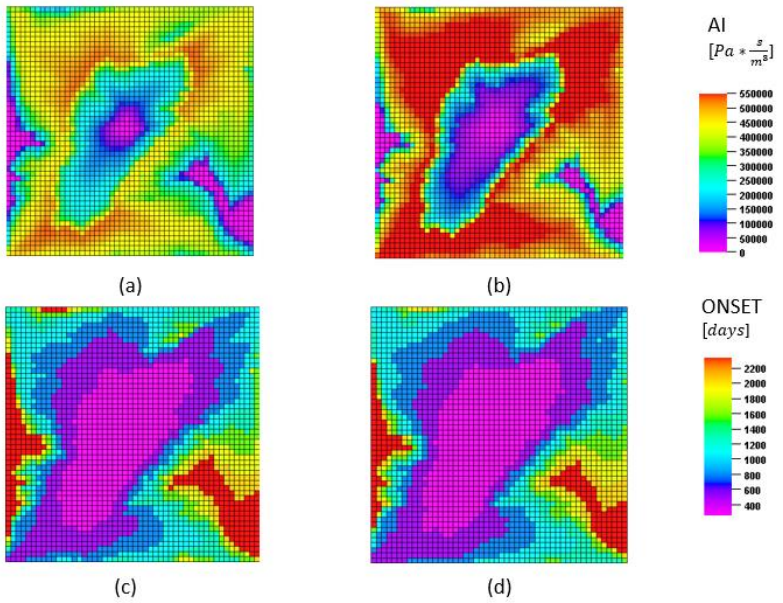

Figure 3.3 Calculated seismic response using different bounds to describe the bulk modulus of the pore-filling fluids. (a) Acoustic impedance changes based on the Voigt bound. (b) Acoustic impedance changes based on the Reuss bound. (c) Onset Time based on the Voigt bound, and (d) Onset Time based on the Reuss bound.

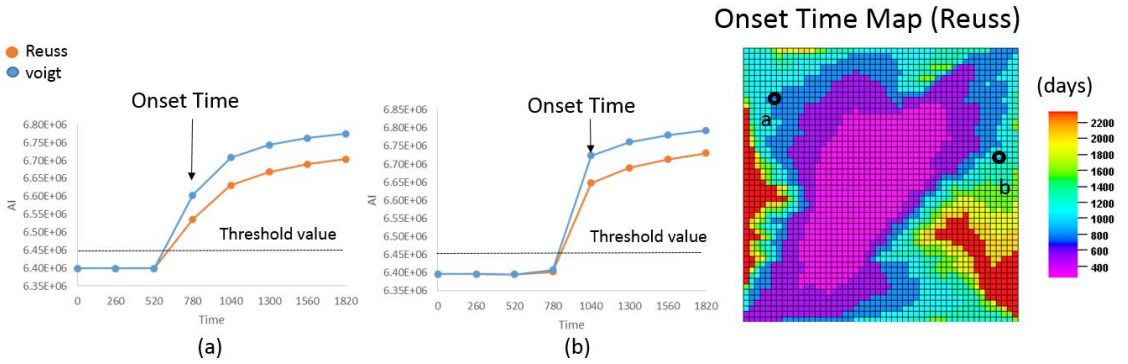

Figure 3.4 The AI response of two points (a and b in the onset time map)

In order to illustrate the different sources of dynamic data in the time lapse integration, we consider two different examples. In the first case, the inversion is based on acoustic impedance amplitude changes. We break up the entire period into three increments, shown in Figure 3.5, to achieve a reasonable resolution over the observation period and calibrate the model against acoustic impedance changes. In the second case, the inversion is based on the onset time integration which converts multiple time-lapse seismic survey data into a single map of onset times**.**

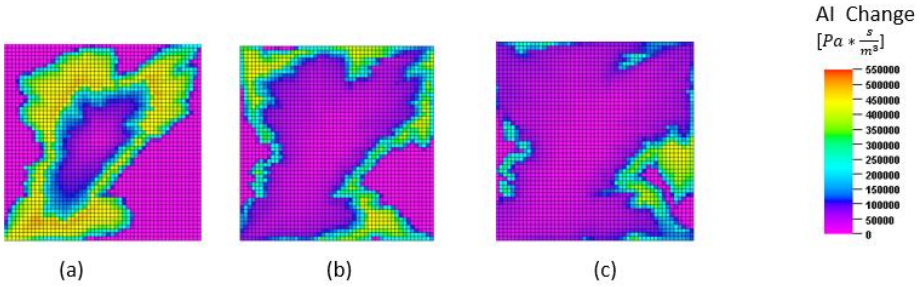

Figure 3.5 The seismic observations for the AI change inversion. (a) AI change between 0 and 780 days (b) AI change between 780 and 1560 days, and (c) AI change between 1560-2040 days.

To emphasis the dependence of the PEM on seismic response, in both cases, the bulk modulus of the pore-filling fluids is calculated based on the Hill estimate (**Eq.3.4**) for the observation set, while we purposely used the Reuss lower bound (**Eq.3.2**) for the simulated data.

The history matching results are shown in Figure 3.6**,** where reductions in objective function values are compared for both cases**.** Note the reduction of the onset time objective function as compared to the acoustic impedance change implies that the onset time is less sensitive to the petro elastic model. In addition, a significant improvement of the calculation time is achieved by compressing the data in to a single map of onset times. Figure 3.7 shows the fit to time lapse seismic for both cases, with a significant improvement in onset time map. Finally, the updated permeability field for both cases is shown in Figure 3.8, it appears that the onset time is able to better identify the low permeability barrier located in the right lower corner of the model.

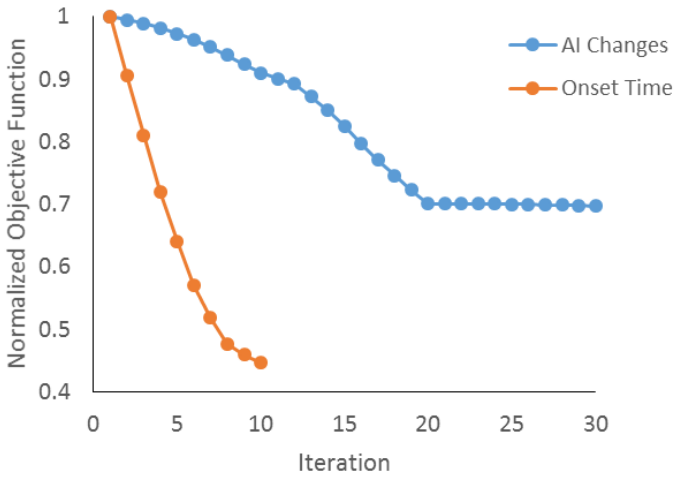

Figure 3.6 Objective function as a function of the number of iterations of the inversion algorithms.

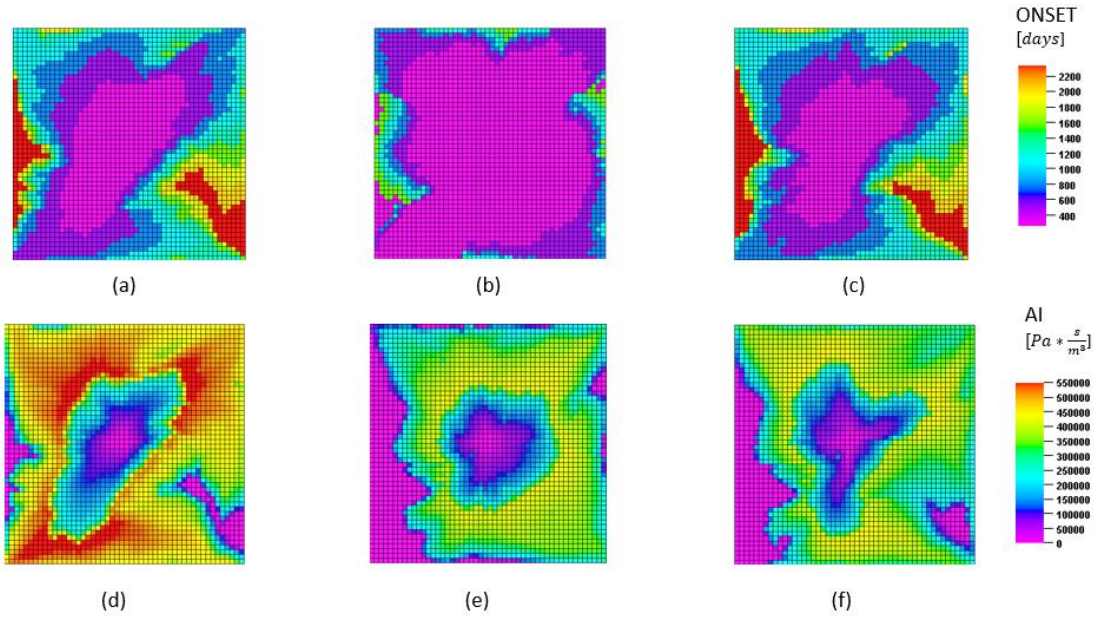

Figure 3.7 Seismic response for different inversion algorithm. (a) Onset Time of the reference model, (b) Onset Time of the initial model, and (c) Onset Time of the updated model. (d) AI changes of the reference model, (b) AI changes of the initial model, and (c) Onset Time of the updated model. (d) AI changes of the reference model, (b) AI changes of the initial model, and (c) AI changes of the updated model.

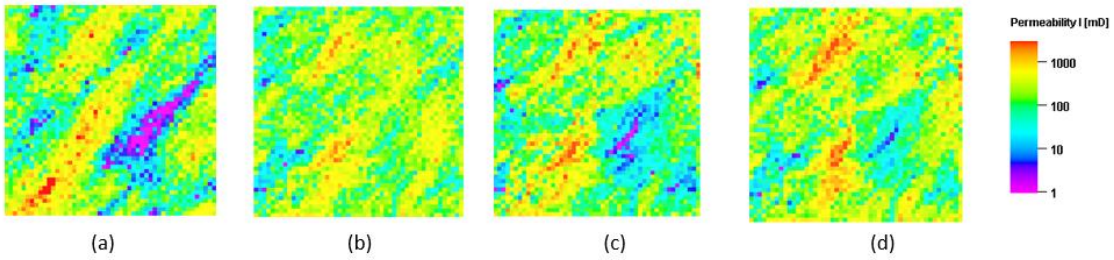

Figure 3.8 Permeability fields for the five-spot synthetic test. (a) Reference model, (b) Initial model, and (c) updated model based on Onset Time data integration, (d) updated model based on AI changes data integration.

3.5.2 The Peace River Case Seismic Monitoring at Pad 31

The Peace River is a heavy oil field in Alberta, Canada. The field has been under several thermal recovery schemes including Cyclic Steam Stimulation (CSS) and Steam Assisted Gravity Drainage (SAGD) to increase the recovery of the bitumen deposits. These processes led to limited recovery of the bitumen originally in place, partly due to insufficient stimulation of the reservoir volume. Recently, one of the production pads, Pad 31, was re-developed with six new horizontal steam injectors (in green, Figure 3.9) and operated as a Top Down Steam Drive (TDSD). This new development was monitored with a permanent seismic monitoring system (the monitoring period was between May 2014 and May 2016) that provides snapshots of reservoir state on a daily basis (Hetz et al. 2017; Lopez et al. 2015). In addition to the ongoing TDSD, one of the producers (31-08 well, Figure 3.9) has undergone CSS to promote communication with the northern part of the pad.

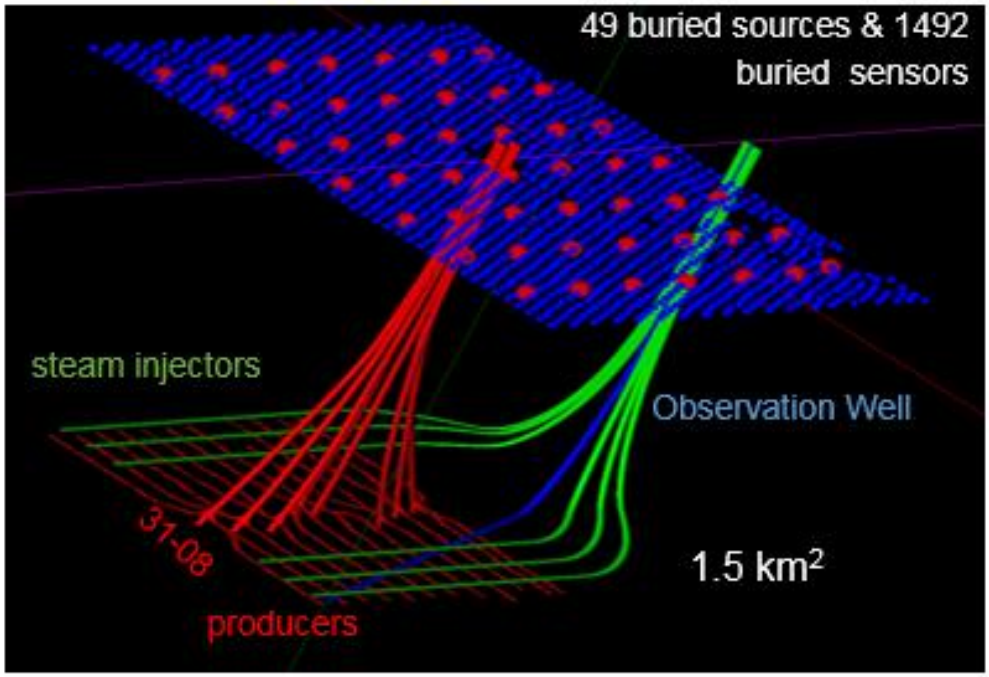

Figure 3.9 Pad 31 horizontal production wells (red), injection wells (green), and observation well (blue). Also shown are seismic sources (red dots) and receivers (blue dots). Producer 31-08 underwent CSS and is the focus of this study.

Our objective is to understand the fluid movements and pressure propagation using the time lapse seismic data and to calibrate reservoir models to the seismic data acquired over a CSS cycle in well 31-08 using an assisted history matching process. At the same time, we would like to reproduce the bottomhole pressure (BHP) response at this well. The fact that the well under consideration is relatively isolated from the rest of the pad and did not seem to be influenced by the ongoing TDSD, allows one to use a sector model for dynamic modeling on a fine grid (Przybysz-Jarnut et al. 2016). The seismic data is translated into time shift maps, expressing the travel time changes in the

seismic wave propagation across the reservoir between a chosen baseline survey (e.g. the start of the cycle) and subsequent monitor surveys. Over the CSS cycle, a total of 175 time lapse seismic surveys are available for integration (Figure 3.10).

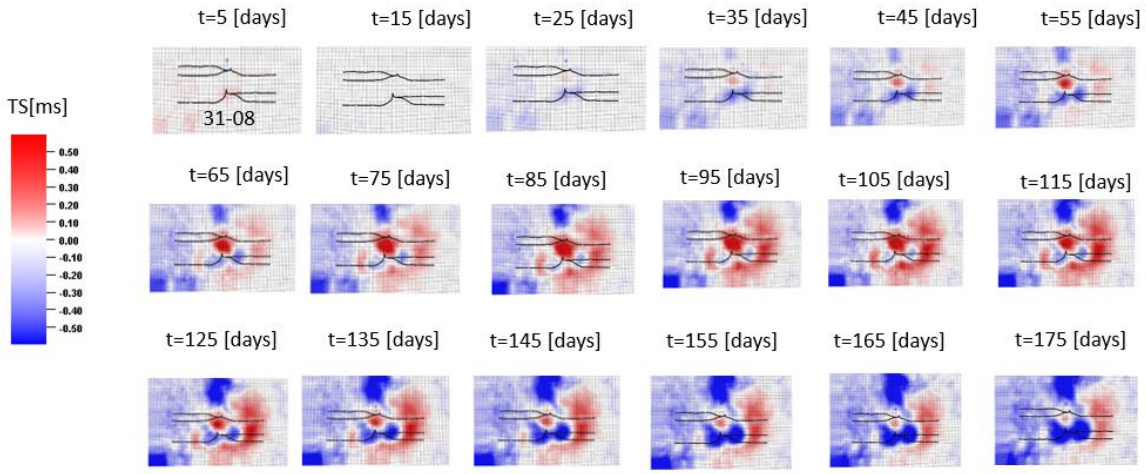

Figure 3.10 Seismic observations in well 31-08. 18 samples of time shift maps are shown out of 175 time shift maps that are available for integration.

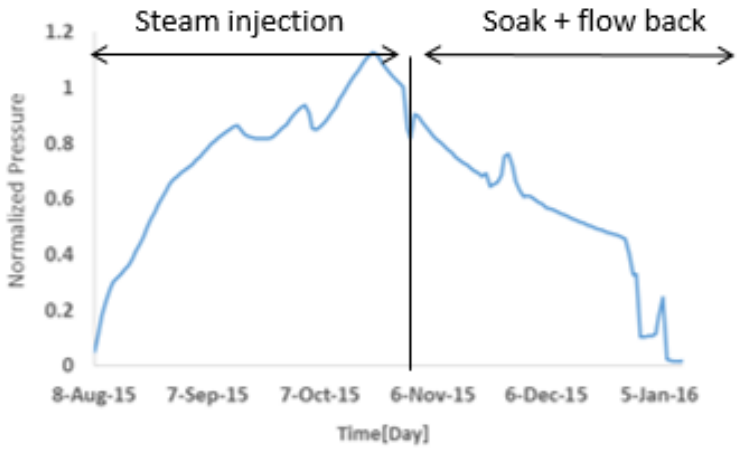

Figure 3.11 The Normalized BHP over the CSS cycle

We use the model derived by (Barker and Xue 2016) to convert the dynamic simulation response to elastic properties. The sensitivity of the petro elastic model is presented in Figure 3.12. The interpretation of the time shift maps can be done based on the suggested rock physics model. For example, time shift increasing (red color in Figure 3.10) is generated by an increase in temperature, pressure or when gas phase replaces water phase. On the other hand, temperature or pressure decreasing as well as water phase replaces gas phase would lead to a decrease in time shift (blue color in Figure 3.10).

The amount and the nature of the recorded time shift data, which combine the effects of temperature, pressure and phase saturation changes in the reservoir, make it extremely challenging and time consuming for history matching. To overcome these

problems, we use our onset time approach to integrate the time lapse seismic data into the model.

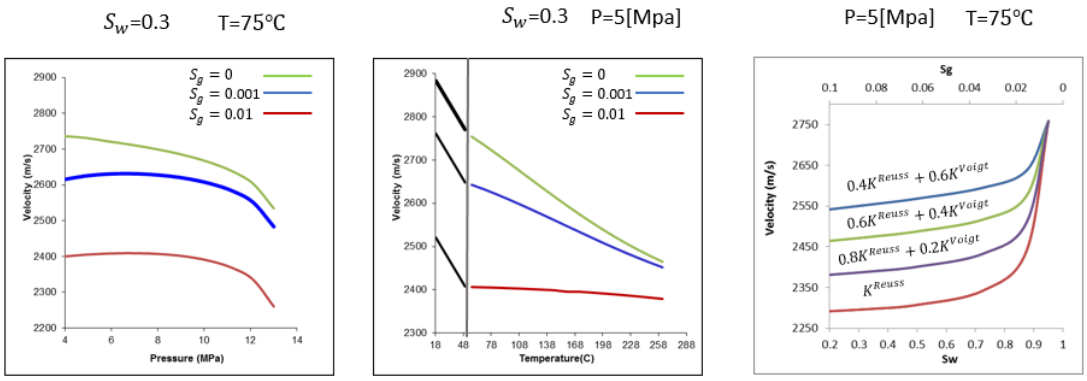

Figure 3.12 Sensitivity of the rock physics model. (a) Velocity of a compressional wave as a function of pressure for different gas saturation where temperature and water saturation are fixed. (b) Velocity of a compressional wave as a function of temperature for different gas saturation where pressure and water saturation are fixed. (c) Velocity of a compressional wave as a function of the saturations. All velocity estimates are computed by Gassmann's approach but using different methods for calculating the composite fluid bulk modulus.

Based on the signal to noise ratio of the seismic dataset, we define the threshold as a decrease of 0.1[mS] in the time-shift. At the first part of the cycle (e.g. the injection), the onset time is associated with water phase replacing gas phase as a result of steam injection. In the second part (e.g. soak), the onset is related to pressure diffusion after the injection ceases.

For the field application, the first step is to sample the seismic observations into the reservoir model grid to be able to compare it with the simulation response. As shown in Figure 3.13, first, inline/crossline data is converted to XY coordinate system. Then, we create a surface on the seismic grid by interpolating the values between the points. Finally, this surface is sampled into the simulation grid.

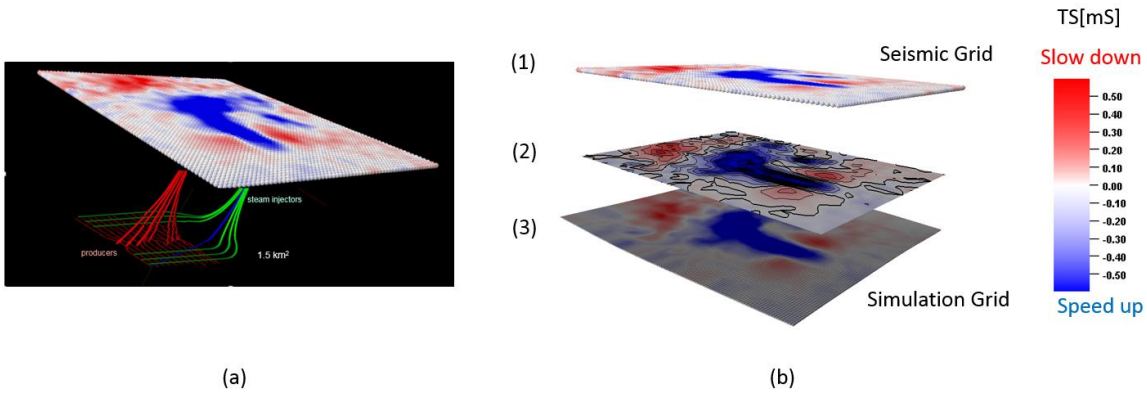

Figure 3.13 Sampling the seismic observations into the reservoir model grid. (a) A 2D map (on the seismic grid), expressing the travel time changes in the seismic wave propagation across the reservoir between a chosen baseline survey (e.g. the start of the cycle) and subsequent monitor surveys. (b) The sampling procedure

After the seismic data was sampled into the simulation grid, we follow the same procedure we presented in the synthetic case (Figure 3.2) to generate the onset time map (Figure 3.14**)**. The onset time map provides an alternative representation of the

propagating changes and, by collapsing the data into one single map, makes it attractive to calibrate the reservoir model using an assisted history matching process.

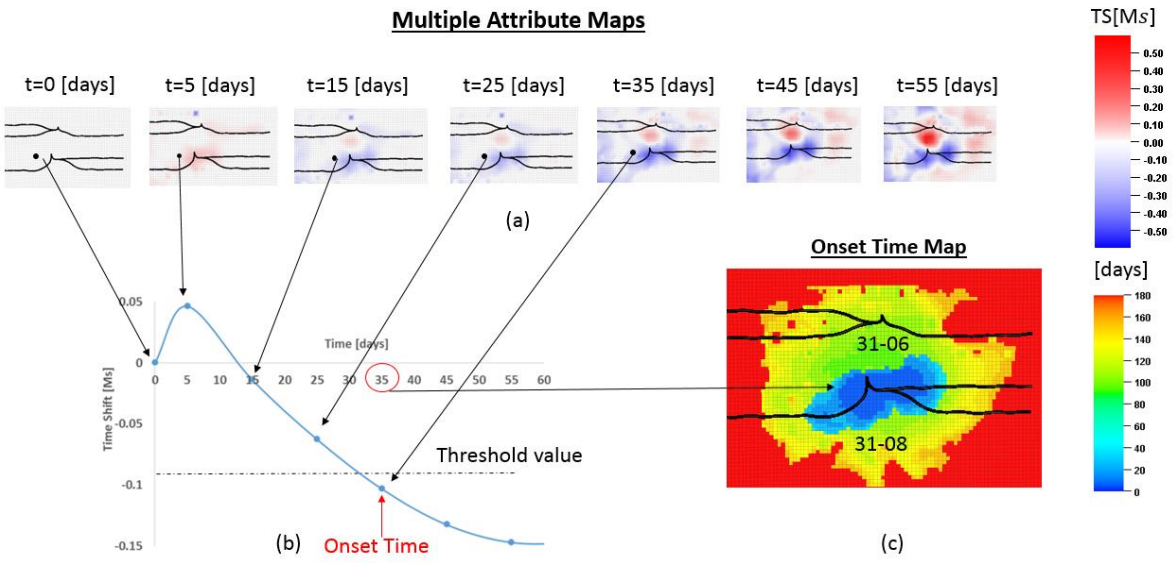

Figure 3.14 Conversion of multiple attribute maps (time shift) to onset time map. (a) A sample of 7 attribute maps (time shifts) out of 175 that are available for integration.(b) A plot of the seismic response of a specific cell (label as black dot in Figure 2(a)) to indicate the onset time. (c) The onset time map after converting from seismic attribute to time. The contours display the front progression.

As previously observed in the synthetic case, the onset time not only leads to a significant data reduction, but also seems to be less sensitive to the unknowns in the petro elastic model. In an effort to examine the sensitivity of the onset time to variations in the method used to map the fluid saturations in the field application, in Figure 3.12C we plot the P- wave velocity as a function of saturation for different models to describe

the bulk modulus of the pore-filling fluids. We observed that the P-wave velocity is very sensitive to the selected model. In Figure 3.15 we plot the time shift changes over the injection period (e.g. the first 82 surveys), calculated using the presented models in Figure 3.12C. At the same time, we generate the corresponding onset time maps for this period as shown in Figure 3.16. While significant differences are seen in the magnitudes of seismic attribute maps, the onset times appear to be relatively insensitive to the petro-elastic model and properly captures areal propagation of changes related in this particular case to steam/fluid propagation.

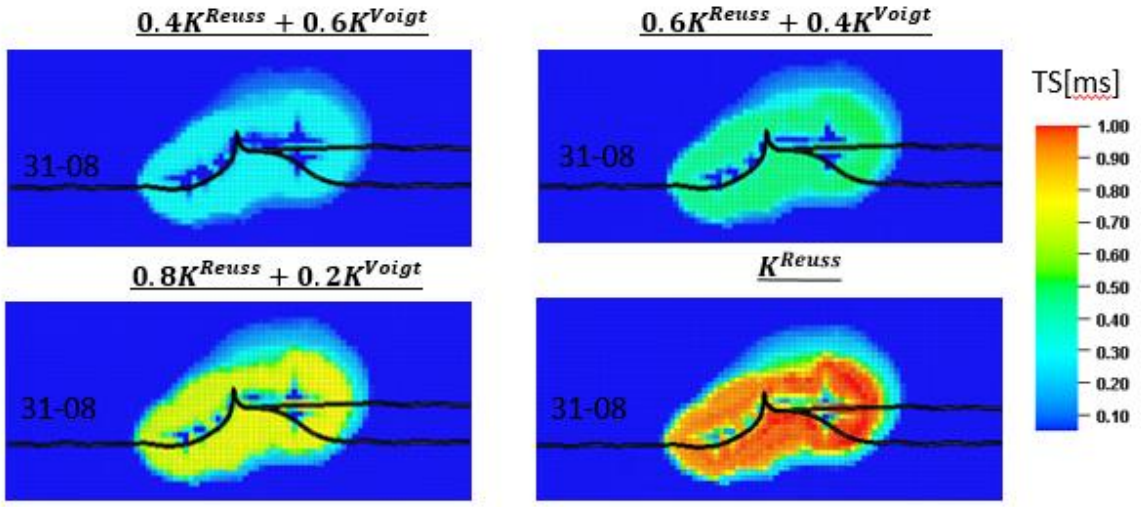

Figure 3.15 Time shift changes, calculated using the models presented in figure 6, after 82 days of steam injection

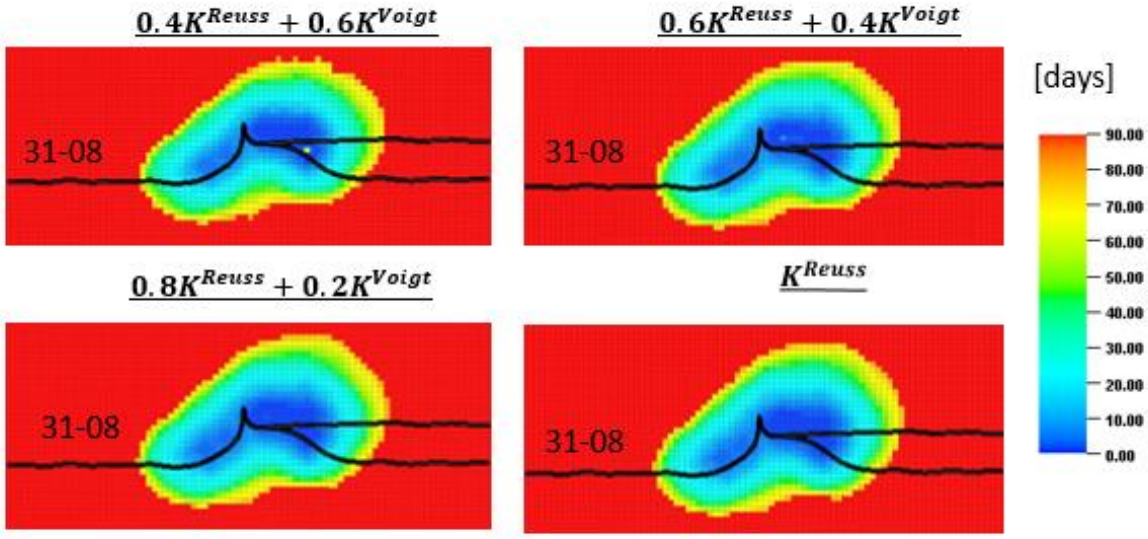

Figure 3.16 Onset tine maps, calculated using the models presented in figure 6, after 82 days of steam injection

3.5.3 Uncertain Parameters and Sensitivity Analysis

Since the heavy oil field has been under production for more than ten years with different thermal recovery schemes, the significant uncertainty lies in the initial conditions and the flow properties of the reservoir at the beginning of the cycle. Table 3.1 summarizes the initial reservoir conditions. While most of the parameters were initialized based on the geologic model or uniformly distributed, the initial temperature distribution was interpolated from the tubing head temperature (THT) within the observed onset time map region at the beginning of the cycle, as illustrated in

Table 3.1 Simulation specification peace river

Parameter	**Initial condition**
Initial pressure	40[bar]
Initial gas saturation	Uniformly distributed (4%)
Initial water saturation	Based on geologic model
Initial temperature	Interpolated from the THT

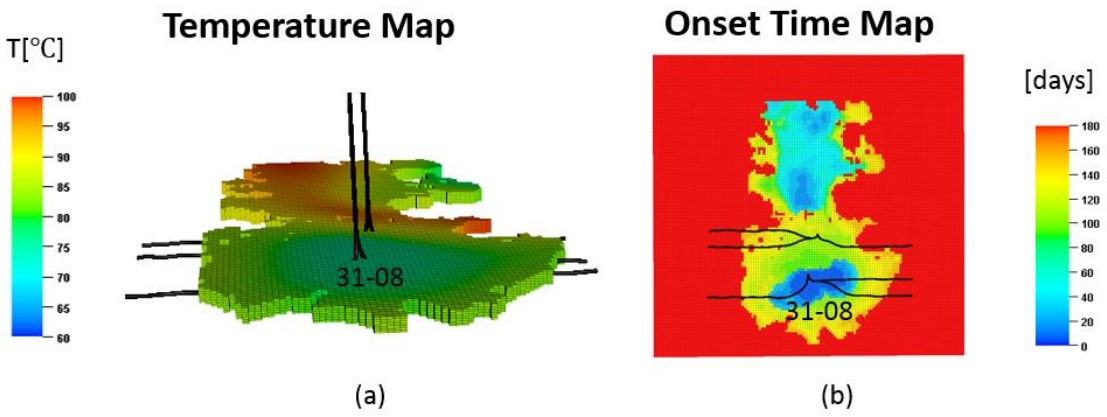

Figure 3. 17 The initial temperature of the CSS interpolated from the THT and the onset time map. (a) The interpolated region and (b) the onset time map for the full field.

We performed a sensitivity analysis to identify the parameters to be updated in the history matching process. Table 3.2 lists the uncertain parameters with the base values and ranges used for the sensitivity study.

Table 3.2 Parameter uncertainties for sensitivity and history matching

Parameter	**Base**	**Low**	**High**
Initial gas saturation	1.0	0.7	1.3
Initial temperature	1.0	0.7	1.3
Completion interval	1.0	0.7	1.3
Permeability	1.0	0.7	1.3
Pore Volume	1.0	0.7	1.3
Relative Permeability	0.75	0.5	1

For the sensitivity study, the objective function was defined as the summation of misfits in the onset time seismic response and the BHP

$$f(\mathbf{m}) = \sum_{i}^{Timestep} \left[\ln\left|\Delta \mathrm{OT}\right|_i + \ln\left|\Delta \mathrm{BHP}\right|_i \right] \tag{3.6}$$

where m is a set of reservoir parameters and Δ represents the misfit from the observed data. Figure 3.18 shows a tornado diagram of the objective function with respect to reservoir parameters listed in Table 3.2. Based on the sensitivity analysis we found that all of parameters have significant influencing on the objective function but the completion interval is the most impacting parameter indicating the need to adjust the size of stimulated zone.

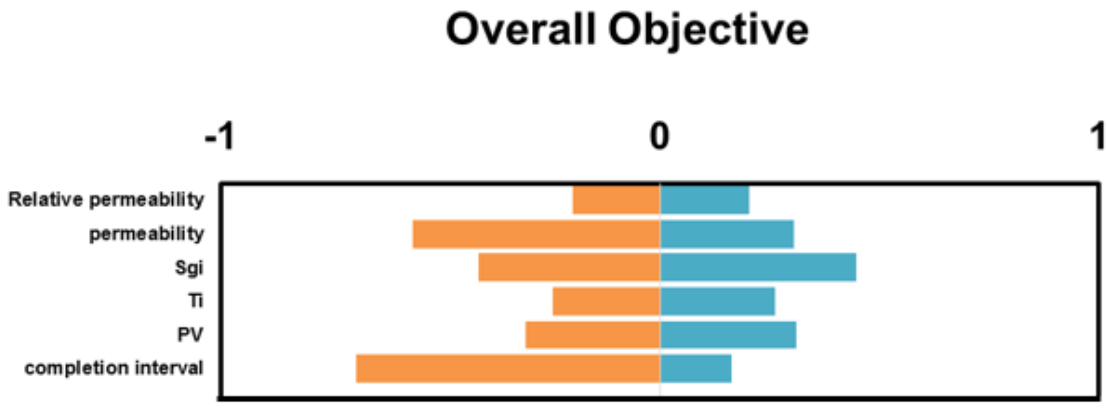

Figure 3.18 Sensitivity analysis of individual uncertain parameter. Low and high cases are colored in blue and orange, respectively.

3.5.4 History Matching First Stage

The CSS cycle can be divided into two periods (Figure 3.11**).** The injection part, which involves steam injection over three months and the soak part, where the fluids naturally flow back to the well after the injection stops. The history matching was carried out following the method outlined by (Zhang et al. 2016), which utilized the Genetic Algorithm (GA) facilitated by use of experimental design and response surface modelling (Yin et al. 2011). For validation purpose, we preformed history matching on the first part of the cycle (82 seismic surveys are available for integration) and used the second part of the cycle to validate the BHP response. The observed onset map and the simulated onset map of the initial model are illustrated in Figure 3.19. Note the large mismatch of propagation time of the initial model. Figure 3.20 shows the BHP of the observed, the initial model and the first 10 simulations. Note that the variation of the

simulated pressure response in the initial 10 models caused by sampling from large range of parameter uncertainties.

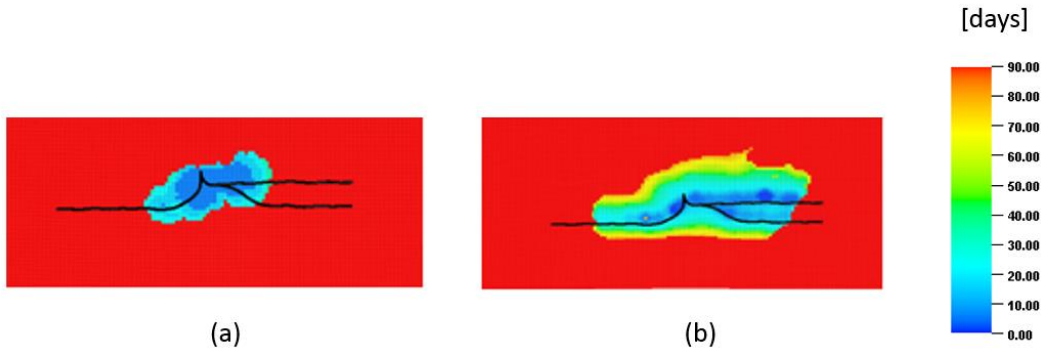

Figure 3.19 Onset time map over the injection interval (A total of 82 seismic surveys are available for integration). (a) Observed data. (b) Initial model.

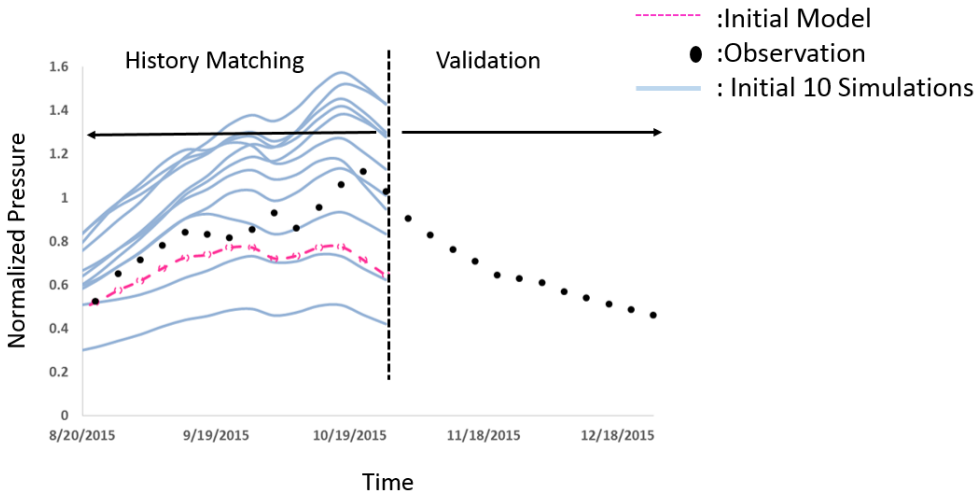

Figure 3.20 Simulated BHP of the initial 10 simulations compared with the observation (dot black line) and the initial model (pink line).

The BHP simulated with 10 models selected based on the objective function were compared with the observed data as shown in Figure 3.21. The selected models were able to closely match pressure behavior in the well for the history matching part and naturally following on the right trend at the validation (e.g. the production period). The onset time map improved significantly as shown in Figure 3.22 compared to the initial model.

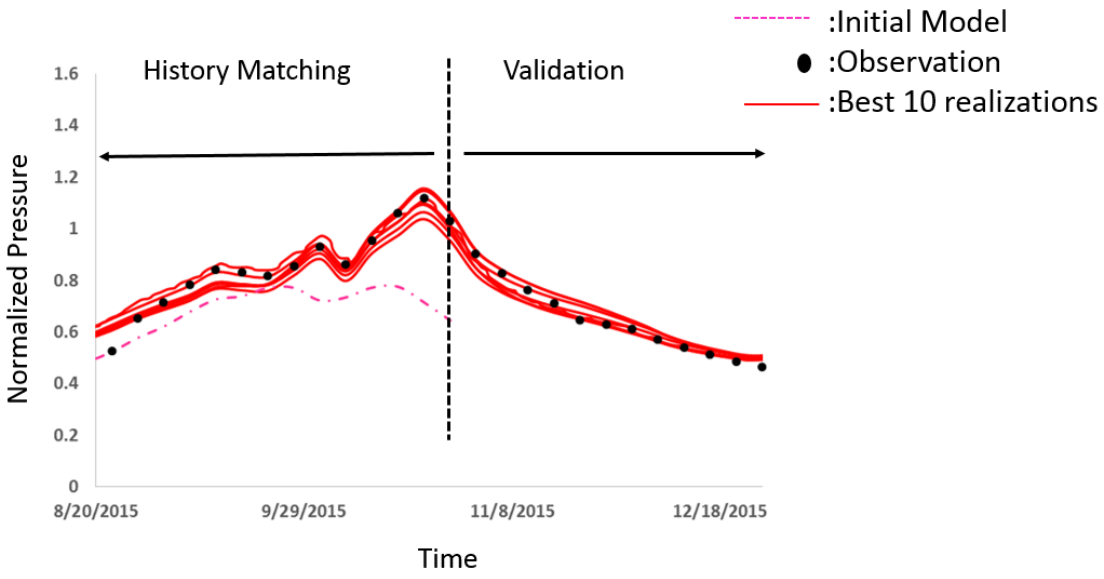

Figure 3.21 Simulated BHP after the history matching compared with the observed data (dot line).

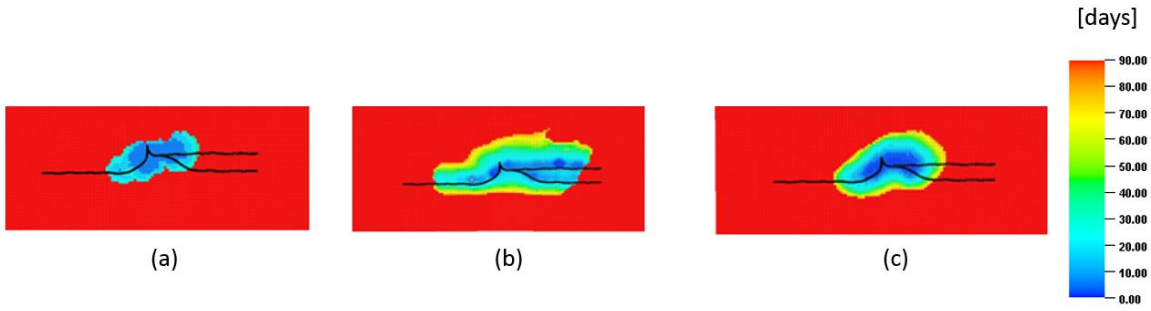

Figure 3.22 Onset time map over the injection interval after the history matching. (a) Observed data, (b) Initial model, and (c) the best model

The model parameters range of the initial generation and the selected model is illustrated in Figure 3.23. Overall we observe a notable reduction in the parameter range. One notable feature is the significant reduction of the completion interval range. To gain some insight into this variation, we plot in Figure 3.24 the onset time map of the upper outlier, the best model, and the lower outlier. The upper outlier represents a case where most of the horizontal part of the well is open for injection. On the other hand, the lower outlier represents a scenario where only the vertical part is open. Note the footprint of the radial flow at the onset time map. The variation of the onset time maps (Figure 3.24) suggesting that the onset time is very sensitive to completion interval. Still even with underestimation of propagation time we were able to reduce the parameters uncertainty range and indicate that most of the injection occurs in the near vertical part.

These initial results show the added value of using onset time to constrain and calibrate reservoir models. The next section will focus on the use of multi-objective optimization to obtain an improved representation of reservoir sweep through identification of stream saturation distribution and steam override.

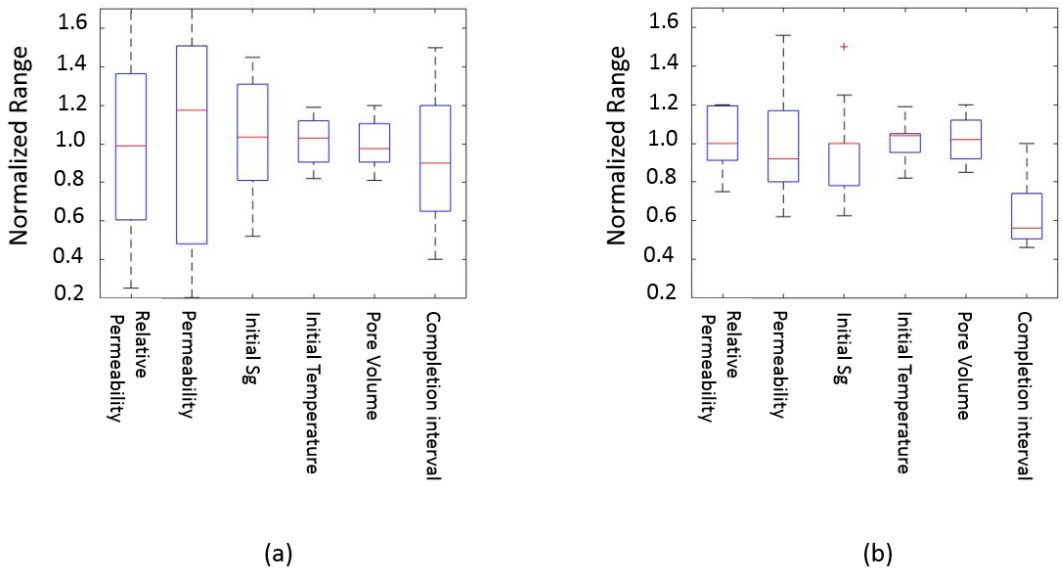

Figure 3.23 Box plots of the parameters range. (a) Initial generation and (b) the best 15 models.

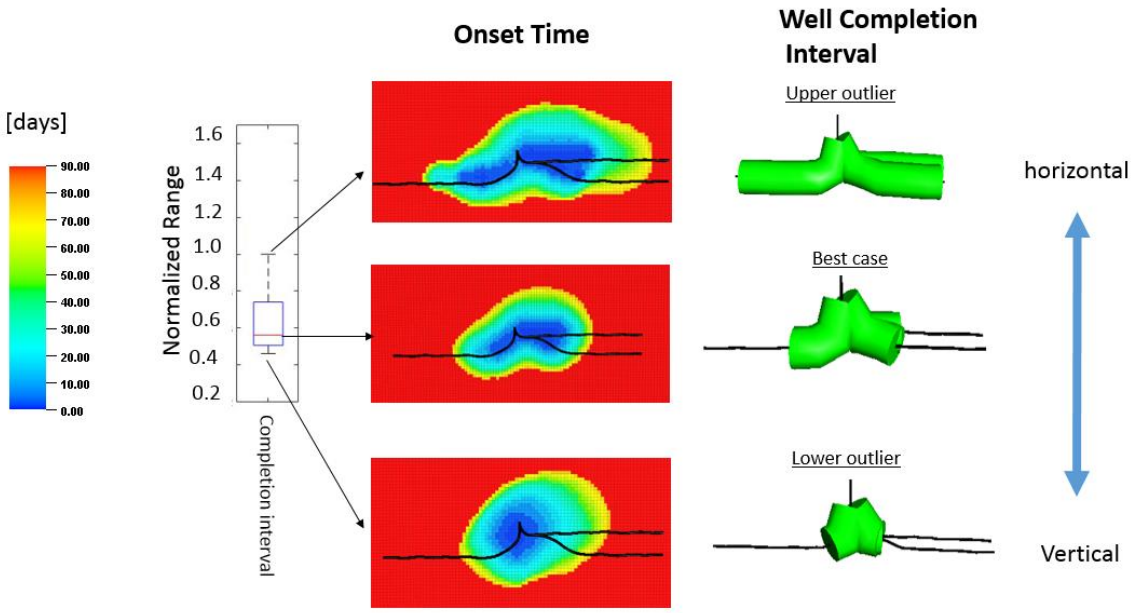

Figure 3.24 The effect of the well completion on the onset time map.

3.5.5 Global to Local Hierarchical History Matching Workflow

After indicating the sensitive parameters and adjusting the completion interval we apply a hierarchical history matching workflow that consists of two stages (Yin et al. 2011): a global update and a local update. Our objective is to calibrate the initial saturations, initial temperature, porosity, and the permeability field to the 4D seismic and the pressure data acquired to understand the unexpected reservoir behavior during CSS cycle in 31-08 well with much less injected volume and higher than expected injection pressure. In the global update, the geological model is first parameterized using an Adjacency-based Transformation, referred to as the ABT (Bhark et al. 2011). It is a

linear transformation characterized by the spectral modes of the adjacency-based Laplacian, L_A , as

$$L_A = \mathrm{D} - \mathrm{A} \tag{3.7}$$

D is a diagonal matrix with a degree of A, known as the adjacency matrix, where the components are calculated as

$$a_{ij} = exp\left(\frac{-\| p_i - p_j \|_2^2}{\sigma_P}\right) \times \begin{cases} exp\left(\frac{-\| x_i - x_j \|_2^2}{\sigma_X}\right) & if\ x_i - x_{j2} < r \\ 0 & else \end{cases}, \tag{3.8}$$

here $x_{i,j}$ is the cell center coordinates and $p_{i,j}$ is the cell property values. Each component represents the similarities between two cells. If the distance between two cells is larger than r , Euclidean cutoff distance, its similarity is defined as zero. σ_P and σ_X determine the weights of the property differences and distances. The eigenvectors of the adjacency-based Laplacian are defined as basis functions which transform the spatial domain to spectral domain, and vice versa using its orthogonality as

$$\mathrm{v} = \Phi^{\mathrm{T}}\mathrm{u} \Leftrightarrow \mathrm{u} = \Phi\mathrm{v}\,, \tag{3.9}$$

where u is N×1 dimension property field in the spatial domain and v is M-length column vector which consists parameter set in the spectral domain. Φ is a (N×M) matrix, containing M-columns ,that defines the discrete basis functions of each length N. Since,

most of spatial information is compressed only in a small number of leading basis vectors, *M* is much smaller than *N*. Thus, it is possible to perform a history matching with much smaller number of parameters, making it more efficient and relaxing a ill-posed problem. For model calibration, a spatial multiplier field has been posed in the multiplicative formulation as follows,

$$\mathrm{u} = \mathrm{u}_0 \circ \Phi \mathrm{v} \tag{3.10}$$

where u_0 is the prior property field, also called initial model, and $\Phi \mathrm{v}$ defines the multiplier field in the spatial domain and ∘ signifies element-wise multiplication (Schur product). This enables it to honor0 the prior property heterogeneity during the model updates.

A Pareto-based multi-objective evolutionary algorithm (Kam et al. 2016) is used to simultaneously integrate the BHP response and the onset time data to update the ABT coefficients. This algorithm is particularly well suited for minimizing multiple, and potentially conflicting, objectives and in this study defined as,

$$Onset\ Time\ Misfit = \sqrt{\frac{1}{N_{obs}} \sum_{i=1}^{N_{obs}} \left(OT_i^{obs} - OT_i^{cal} \right)^2} \tag{3.11}$$

and,

$$BHP\ Misfit = \sqrt{\frac{1}{N_{time}} \sum_{i=1}^{N_{time}} \left(BHP_i^{obs} - BHP_i^{cal} \right)^2} \tag{3.12}$$

Here is N_{time} the total number of timesteps and N_{obs} is the total number of seismic observation points.

In the local update, the gridblock permeability is calibrated to match the onset time data using the streamline approach, as demonstrated in the synthetic case, followed by BHP matching at the well. The entire CSS cycle can be divided into two periods. The injection part, which involves steam injection over three months and the soak part, to allow for heat exchange after which fluids are naturally flown back to the well. We preformed history matching on the first part of the cycle (82 seismic surveys are available for integration) and used the second part of the cycle to validate the BHP response.

The observed onset time map and the simulated onset time map of the initial model are illustrated in Figure 3.25. Note the large mismatch of propagation time of the initial model.

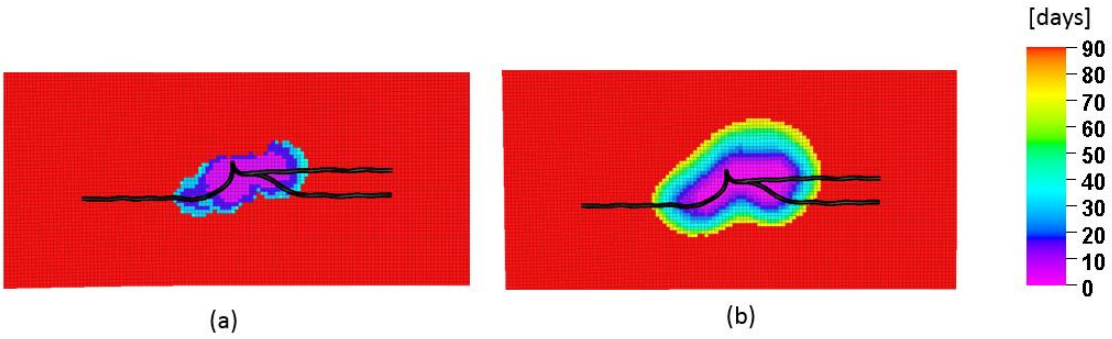

Figure 3.25 Top view of onset time map over the injection interval (a total of 82 seismic surveys are available for integration). (a) Observed data and (b) Initial model.

The first step in our data calibration procedure is to parameterize the initial saturations, initial temperature, porosity and permeability using ABT parameterization. While most of the parameters were initialized based on the geologic model or uniformly distributed, the initial temperature distribution was interpolated from the tubing head temperature (THT) at the beginning of the cycle, within the observed onset time map region. Since the gas saturation was uniformly distributed we use the observed onset time to calculate its adjacency matrix for the ABT parameterization. A Total of 50 basis functions (10 per each property) and corresponding basis coefficients are used to modify the initial properties in the course of model calibration. The ABT basis functions of layer 17 are shown in Figure 3.26. Note that the variations in the ABT basis functions are as a results of the property heterogeneity.

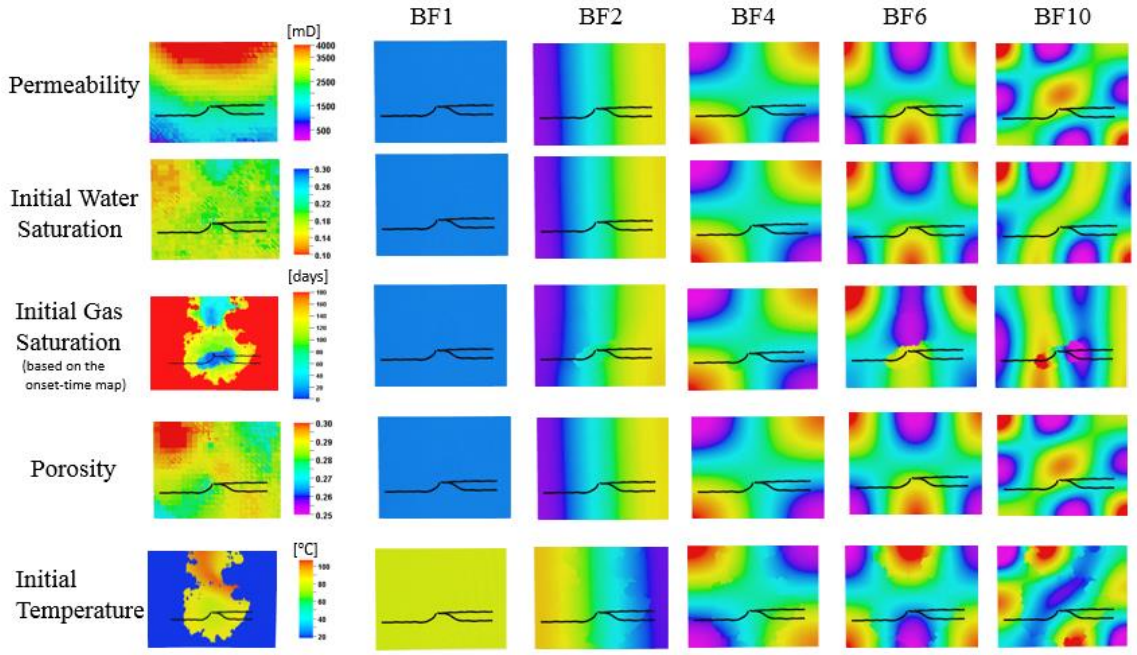

Figure 3.26 Parameterization of the parameters multiplier field at layer 17 (Top view) using ABT basis function

The Pareto-based evolutionary algorithm is solved using a genetic algorithm over 30 generations with papulation of 150 members per generation. The large number of simulations allows us to test different combinations of the model parameters and alternative dynamic realizations. The resulting multi-objective function for the initial and final generation is shown in Figure 3.27.

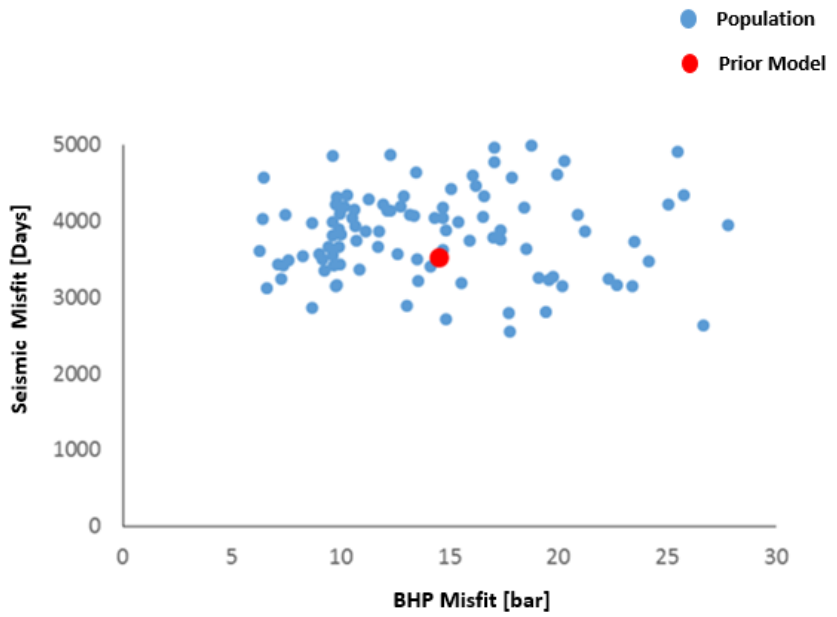

(a)

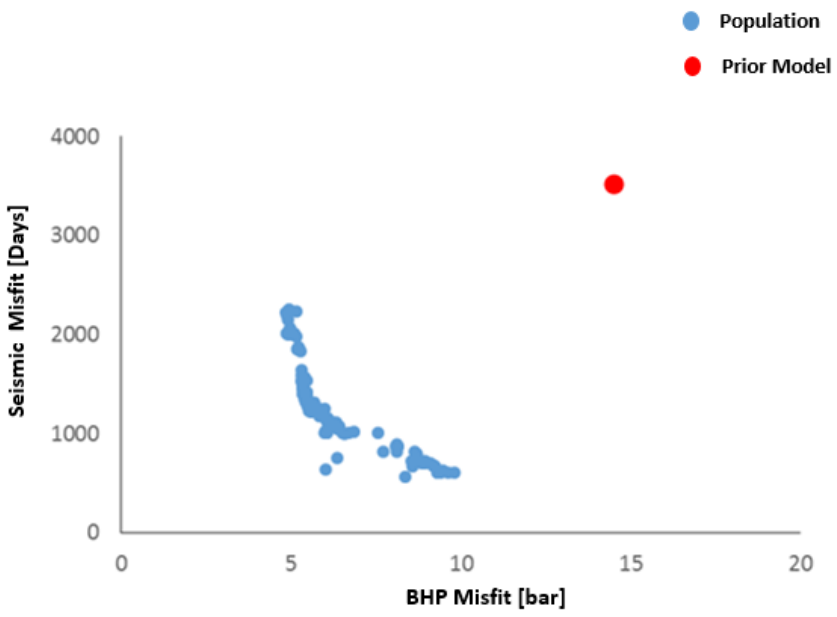

(b)

Figure 3.27 Multi-objective function comparisons between initial generation and the final generation in the global step model calibration. (a) Initial model and (b) Final generation.

While an overall reduction is observed for both the seismic data and the BHP, the trade-off between the objectives is clearly shown at the Pareto-fronts. By applying a cluster analysis, we further investigate the objective space as shown in Figure 3.28. Figure 3.29, Figure 3.30and Figure 3.31 show the updated onset time maps of selected models for cluster 1cluster 2 and cluster 3, respectively. For all clusters, we observed a notably improvement from the initial onset time map calculated using the prior model. In Figure 3.32 we plot the pressure response of 40 updated models, from all cluster, over the entire CSS cycle. There is marked improvement in the match quality that results from the integration of global step where the selected models from cluster 1 tend to overestimate the pressure. One notable feature is the consistent pressure match to the soak part (validation), where we used the history matched models to predict the pressure behavior indicating that the models are able to adequately represent the saturation propagation in the reservoir.

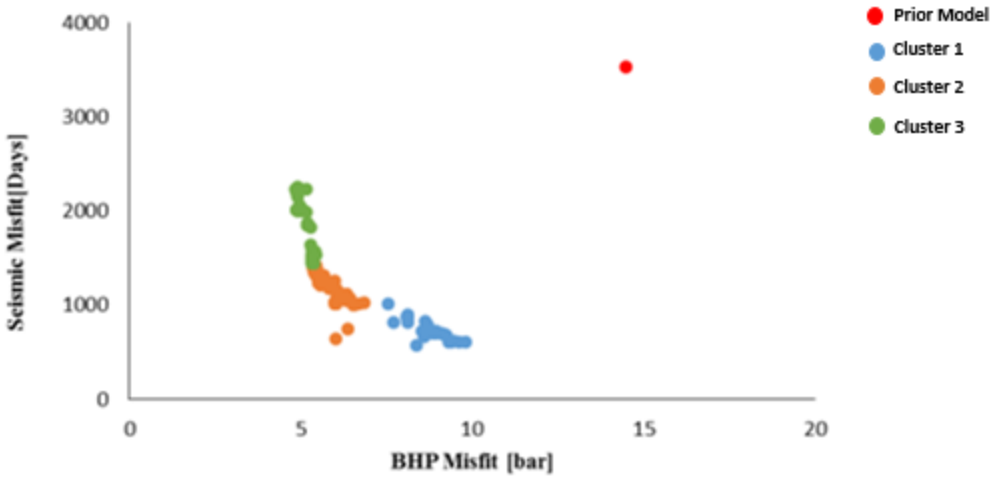

Figure 3.28 cluster analysis results for the last generation of the global history matching step.

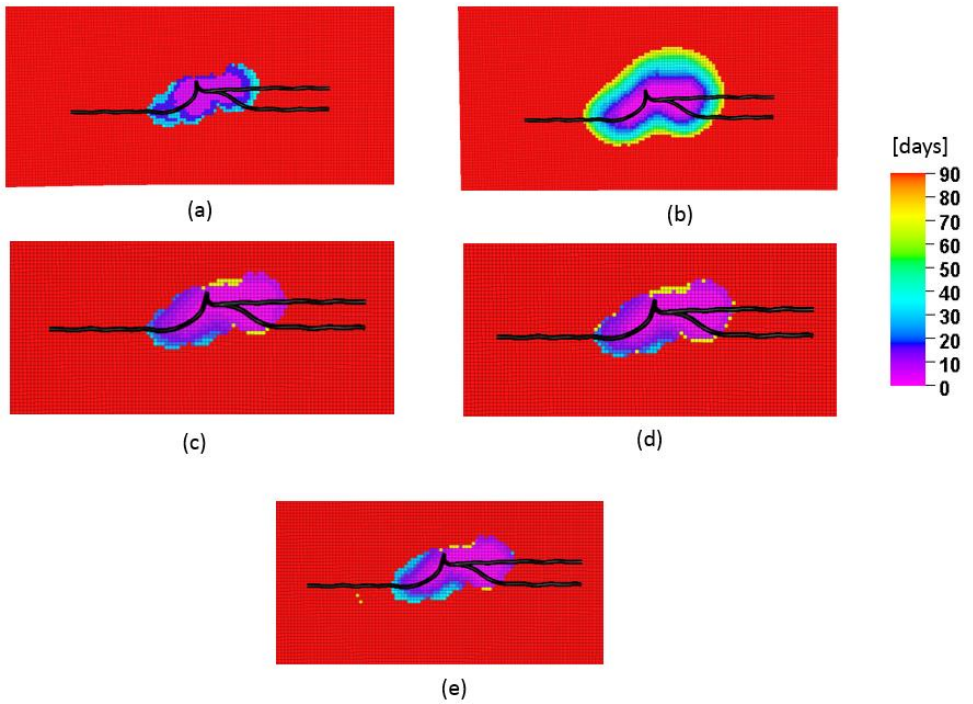

Figure 3.29 Onset time maps for selected models in cluster 1. (a) Observed onset time map, (b) initial onset time map ,(c) model 4425 (d) model 4712 and (e) model 3480

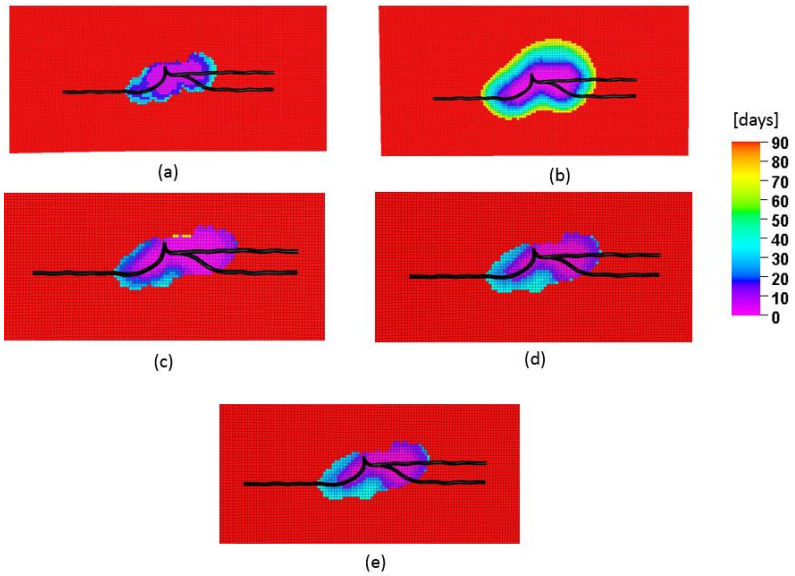

Figure 3.30 Onset time maps for selected models in cluster 2. (a) Observed onset time map, (b) initial onset time map ,(c) model 4430 (d) model 4633 and (e) model 4122

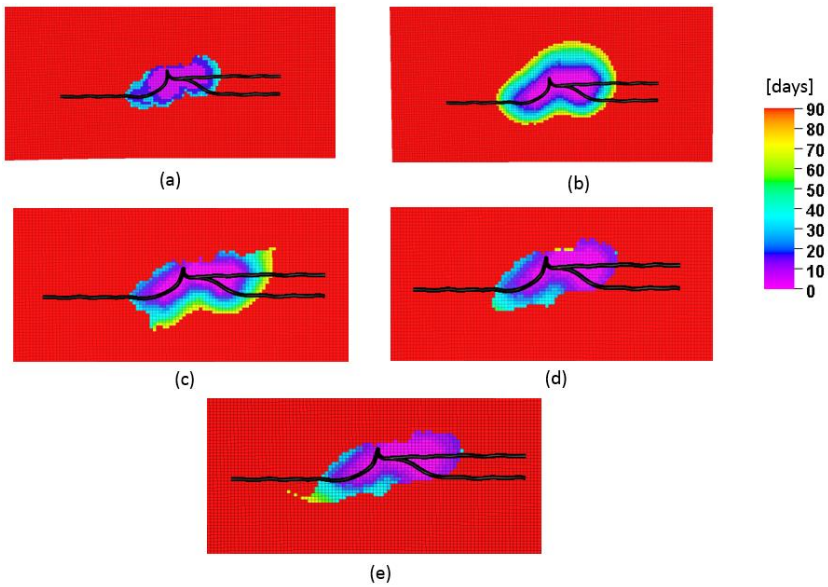

Figure 3.31 Onset time maps for selected models in cluster 3. (a) Observed onset time map, (b) initial onset time map, (c) model 4770 (d) model 4638 and (e) model 4492

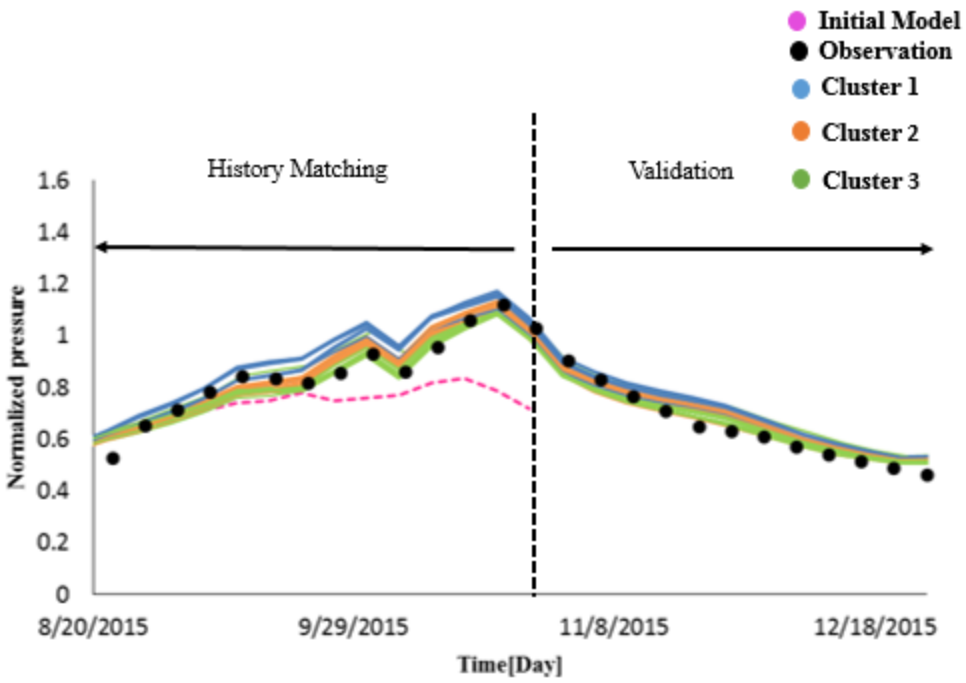

Figure 3.32 Pressure response of 40 models from the final generation. pink line is the initial model, black dots are the observed pressure response and color lines are the selected models from the final generation.

By looking on the change of the parameters over the global step we can gain some insight on the different physical mechanisms that are associated with the clusters. Figure 3.33 shows the change in the reservoir description for a selected model in each cluster. For example, it is observed that the permeability near the well decreases in cluster 1. Also, the water saturation in the bottom water zone increases compared to clusters 2 and 3. This can explain the overestimate of the pressure matching the associated with cluster1 (Figure 3.32). Similarly, in clusters 2 and 3, the change in the temperature and gas saturation distribution around the well resulting different spatial

flow patterns that reflect from the onset time maps with underestimation of propagation time. The relationship between the clusters can be further investigate by looking on the conflicting regions between the onset time and the BHP for each parameter. The conflicting regions (CR) is defined as

$$CR = \Delta K_{onset-time} \times \Delta K_{BHP} \ , \tag{3.13}$$

where $\Delta K_{onset-time}$ is the average parameter change that leads to smaller onset time mismatch (cluster 1) and ΔK_{BHP} is the average parameter change resulting smaller mismatch in the BHP (cluster 2). Negative values for *CR* in a specific region, indicates that the objective functions are conflicting with respect to a given parameter.Figure 3.34 shows the conflicting regions for the parameters that have been updated in the global step. For example it observed that the conflicting region for the initial gas saturation is around the vertical part of the well.

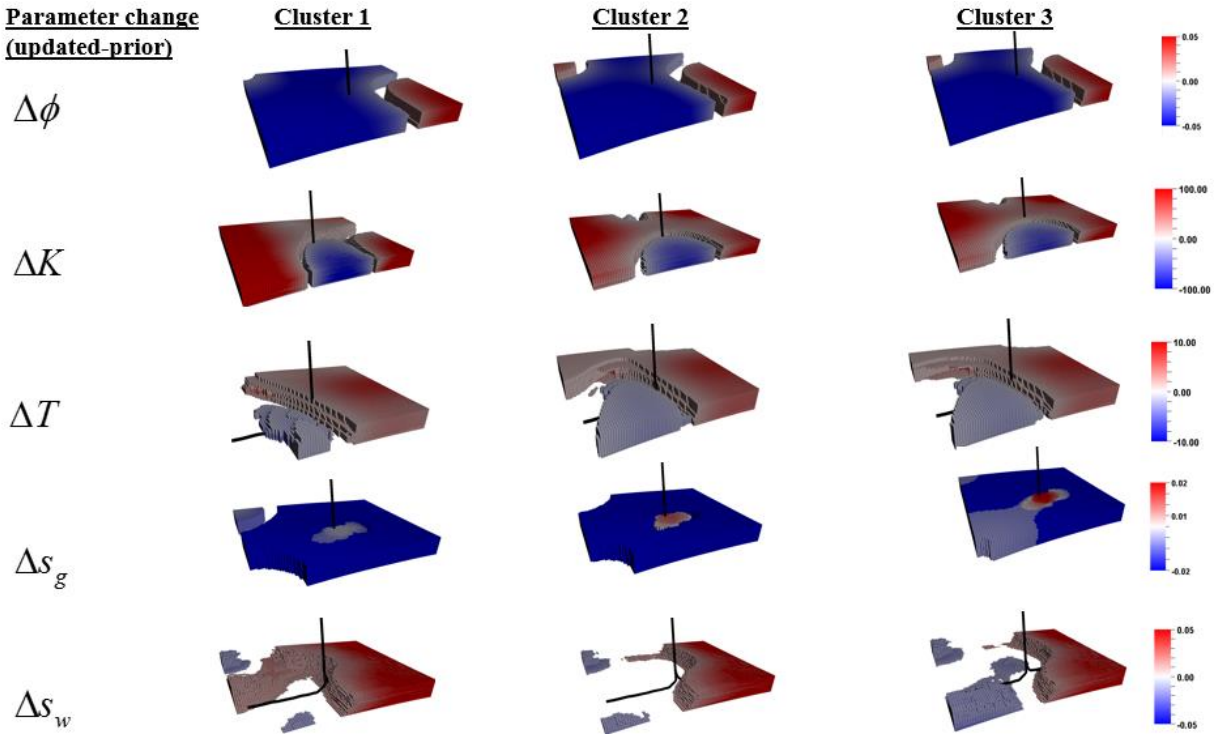

Figure 3.33 The change in the updated parameters over the global step for a selected model in each cluster.

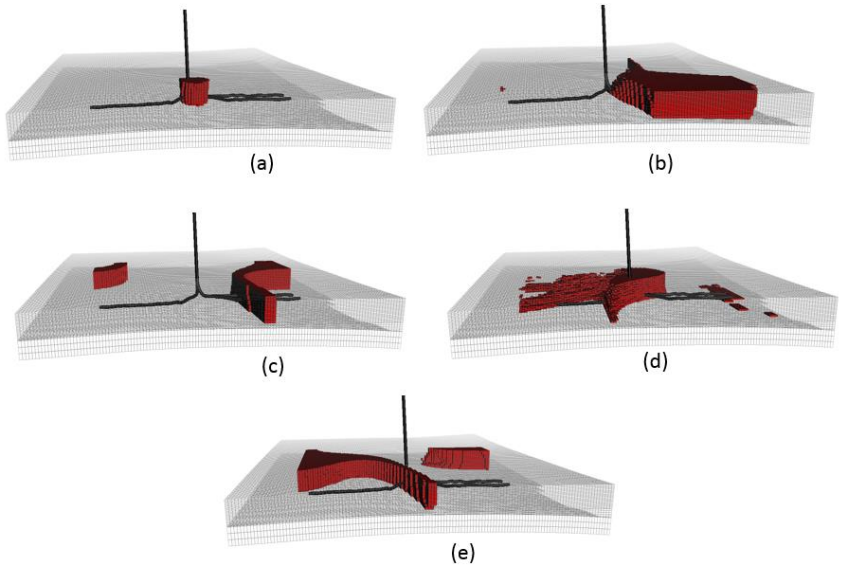

Figure 3.34 Conflicting reigns (red color) between the seismic updates and the BHP updates. (a) Initial gas saturation, (b) permeability, (c) porosity, (d) initial water saturation and (e) initial temperature.

3.5.5.1 Local Step Onset Time and BHP Data Integration

The matching of the propagation time can by further improved by applying our local step to update the permeability field on a cell-by-cell basis. Based on the cluster analysis we select several candidate models for the local step. Our history matching here calibrates the gridblock permeability to the onset time data and follows the same procedure as illustrated in the synthetic case. The reduction in the onset time misfit through the local inversion workflow for one of the models is shown in Figure 3.35

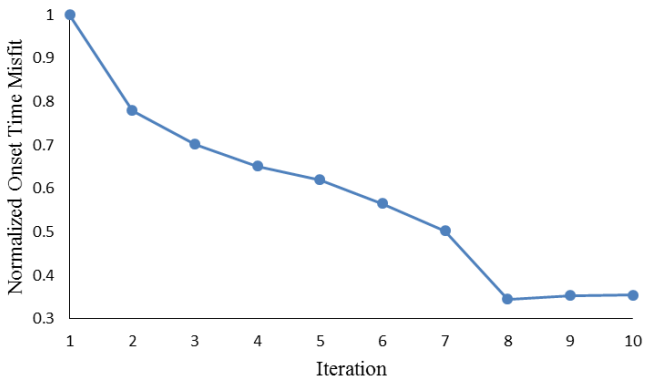

Figure 3.35 Seismic data misfit as a function of the number of iterations of the inversion algorithms

Figure 3.36 and Figure 3.37 show the results of the onset time response for a selected model in cluster 1 and cluster 2. The updated onset time response from the local step significantly improves the results due to local adjustments of reservoir flow properties.

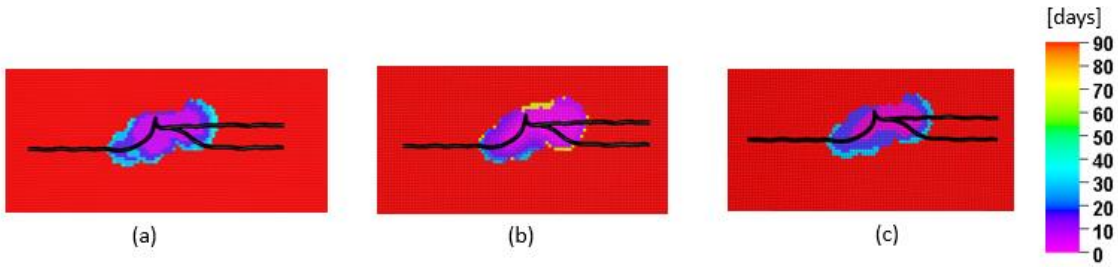

Figure 3.36 Top view of the onset time map after the history matching to a selected model from cluster 1. (a) Observed data, (b) after global, and (c) the final updated model

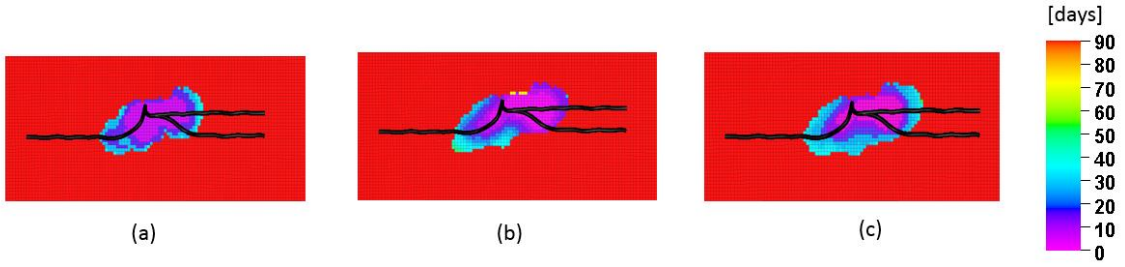

Figure 3.37 Top view of the onset time map after the history matching to a selected model from cluster 2. (a) Observed data, (b) after global, and (c) the final updated model

The changes made to permeability field resulting from the local update step are shown in Figure 3.38 and Figure 3.39 emphasizing the ability of the local updates to further improve the match to the data. These updates imply that the stimulated zones are located mostly arounds the vertical part of the well. Figure 3.40 and Figure 3.41 show the results of the model calibration procedure, comparing the pressure response before and following the local step data integration. Notable results of the inversion procedure are a matched pressure behavior over the injection interval (history matching), but more importantly we were able to closely match pressure behavior in the well at the validation period (e.g. the soak part).

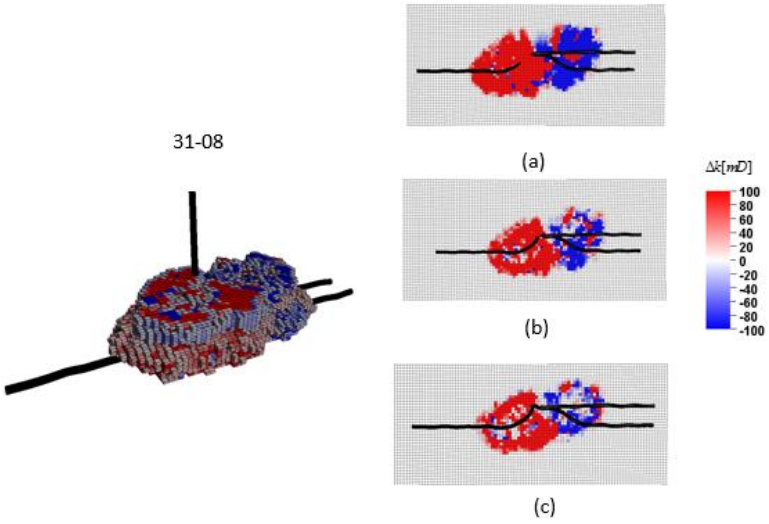

Figure 3.38 Permeability model change (final-prior) for a selected model in cluster 1. (a) Top view of layer 14, (b) Top view of layer 17 and (c) top view of layer 20

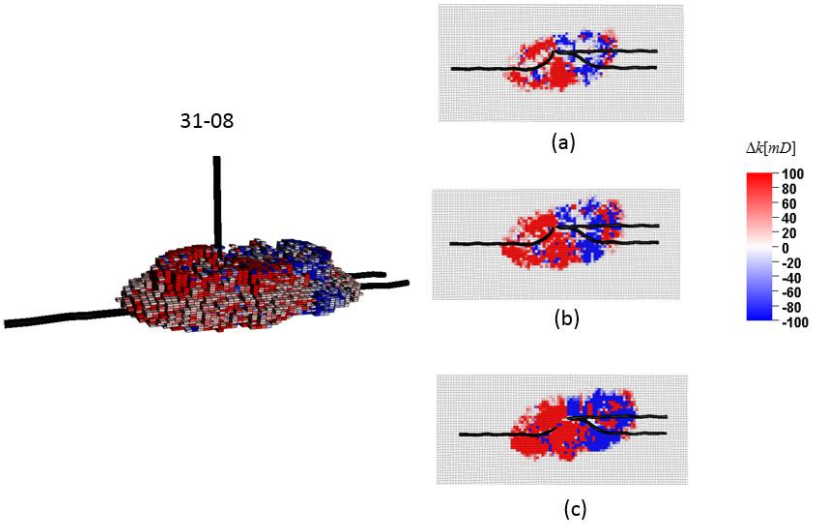

Figure 3.39 Permeability model change (final-prior) for a selected model in cluster 2. (a) Top view of layer 14, (b) Top view of layer 17 and (c) top view of layer 20.

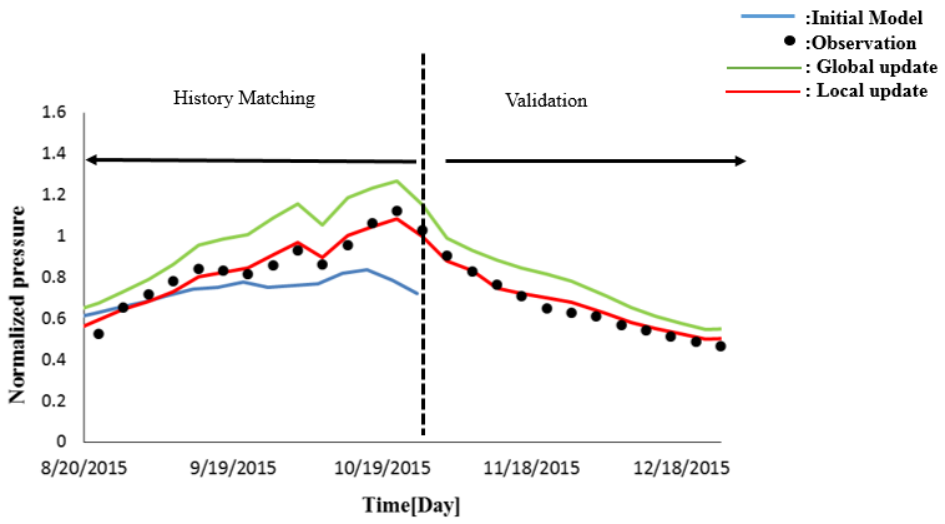

Figure 3.40 The BHP response of well 31-08 over the CSS cycle after the local updates for a selected model in cluster 1.

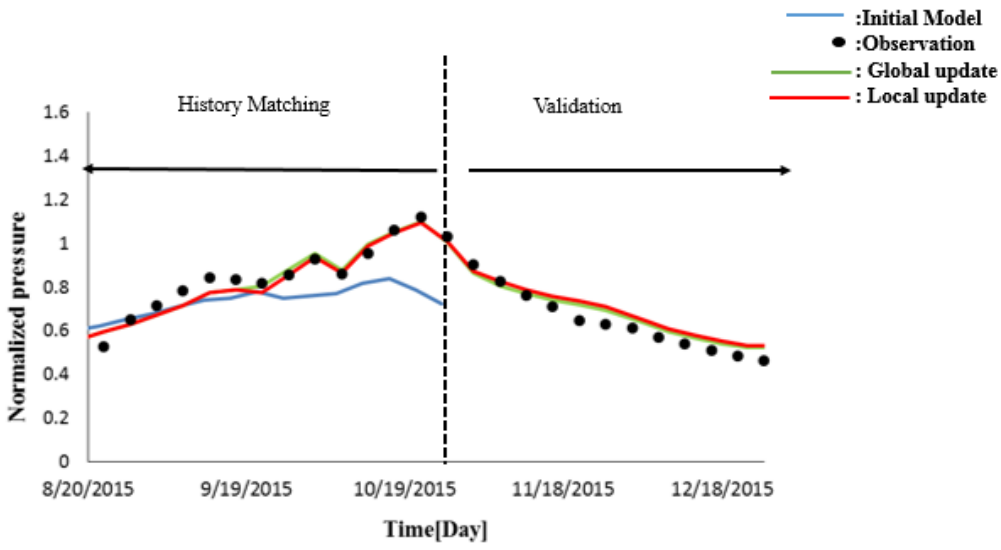

Figure 3.41 The BHP response of well 31-08 over the CSS cycle after the local updates for a selected model in cluster 2.

The onset-time map is not only a useful tool for better matching the model, but also gives additional insight of the physics that occurs in the reservoir. We plot the water saturation changes over the injection period for the initial model and the updated models, as shown in Figure 3.42 and Figure 3.43. This figure shows that the adjustments in the injected fluid distribution as a results of updating the flow properties based on the seismic observation.

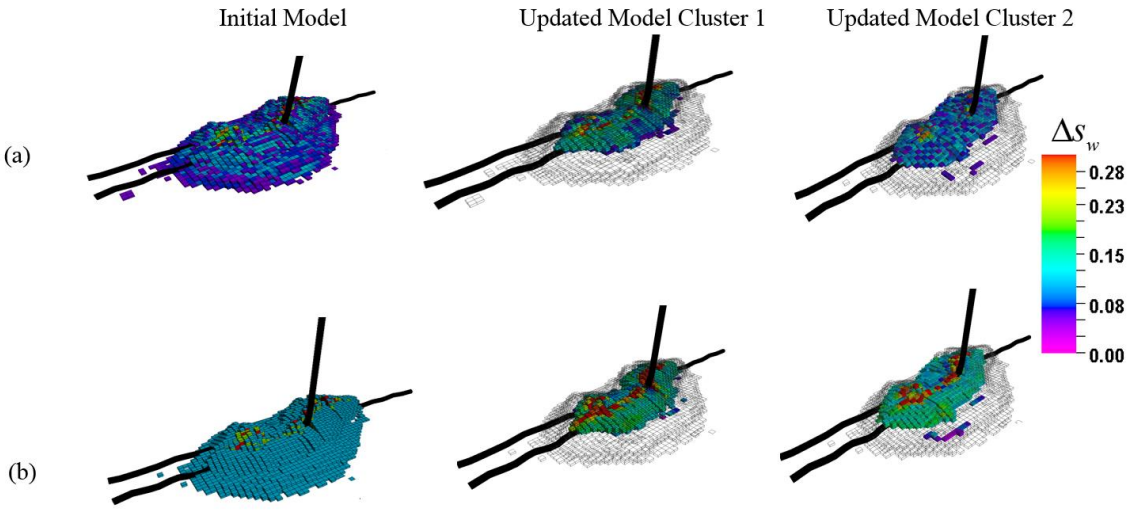

Figure 3.42 Water saturation change over the injection cycle for the initial and the updated models. The transparent cells in the updated models represent the water saturation changes observed in the initial model. (a) Water saturation changes after 45 days. (b) Water saturation changes after 85 days.

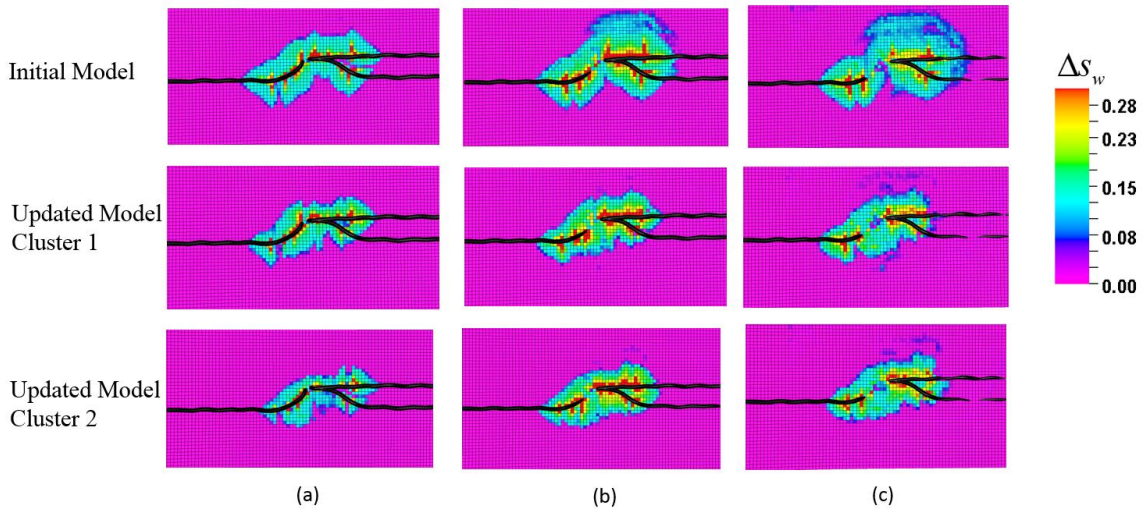

Figure 3.43 Top view of water saturation change after 45 days in the initial and the updated models for selected layers. (a) Layer 17, (b) layer 20, and (c) layer 21.

In addition, the onset-time maps help us to identify the steam override which is a common phenomenon in steam injection processes. The reason for this phenomenon is that mobility of displaced fluid is much lower than that of the displacing fluid (steam). Due to the differences in density between steam and oil, steam override occurs. Figure 3.44 shows the water saturation along the streamlines over the injection period. At the beginning of the cycle (Figure 3.44a) the steam starts moving upward as soon as it is injected inside the model. This movement is captured by the onset time map. The gravity override phenomenon becomes less severe in the course of time, as the fluid moves downward at later times (Figure 3.44b).

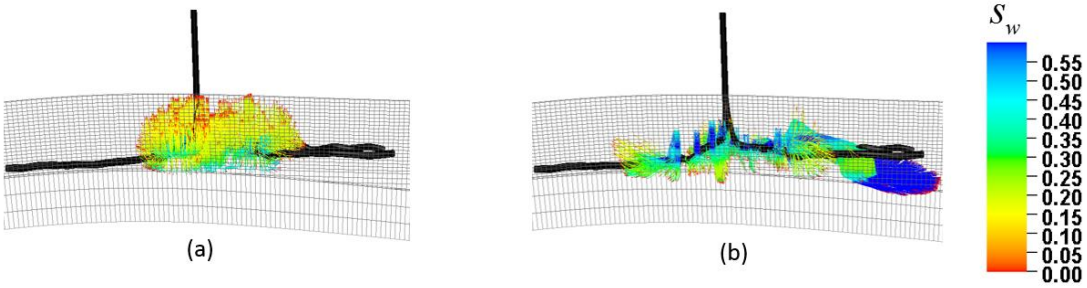

Figure 3.44 Cross view of the water saturation along the streamlines over the injection interval. (a) Water saturation along the streamlines after 5 days, and (b) water saturation along the streamlines after 80 days.

Overall our hierarchical history matching approach significantly reduced the misfit associated with 4D seismic and pressure data and provided an improved representation of reservoir sweep through identification of fluid saturation distribution and steam override.

3.6 Conclusions

In this chapter, we have proposed a novel approach to integrate frequent time lapse seismic data into high resolution reservoir models based on the seismic onset times. The technique is able to reconcile the model heterogeneity by compressing multiple seismic surveys into a single map of onset times that represents the propagation of changes in the reservoir.

Some of the conclusions from this study are the following:

- We propose a novel and computationally efficient approach for time lapse seismic integration using the onset time which is able to efficiently display the front propagation in order to update the flow properties.
- Our synthetic and field applications show that unlike seismic impedance, the onset times appear to be relatively insensitive to the petro elastic model but sensitive to the steam/fluid propagation, temperature and pressure.
- The onset time leads to a significant data reduction and provides practical and faster approach that allows testing alternative dynamic realizations, making the algorithm suitable for large field applications with frequent seismic surveys.
- The Peace River application demonstrates the feasibility and the robustness of the hierarchical workflow to integrate onset times and pressure data. Unlike the manual history matching (Przybysz-Jarnut et al, 2016), in the global step our approach updates the parameters simultaneously, which allows testing different combinations of parameters uncertainty range. The compression of the frequent seismic surveys into a single set of onsets assists efficient history matching using the population-based technique that requires a large number of simulation runs. In the local stage, where the flow properties were adjusted on a cell by cell basis, the algorithm was able to improve the location of the water/steam front and identified the location of increased permeabilities which in case of steam injection in heavy oil is equivalent with stimulated zones. With this technique, through initial conditions and local permeability updates, we were able to

identify the injectivity profile along the horizontal well, which was crucial for further development considerations.

- The results clearly show the importance of accounting for both the global and the local updates to match the data, as seen through improved estimation of the permeability distribution, fluid saturation evolution and swept volume.

CHAPTER IV ONSET TIME VS. AMPLITUDE MATCHING FOR SEISMIC DATA INTEGRATION

4.1 Chapter Summary

In this chapter, we explore the effectiveness of the onset time and the amplitude inversion to solve the inverse problem associated with integrating 4D seismic data into the reservoir model. By applying the geometric concept of curvature(Bates and Watts 1980), we quantitatively investigate the nonlinearity associated with each of the inversion methods. A high degree of nonlinearity usually leads to problems in convergence and instability of the solution, resulting in an inadequate history matched model. It is found that integration of seismic data using the amplitude inversion can be orders of magnitude more nonlinear compared to the onset time inversion. Also, the onset time inversion has a much less dense matrix of sensitivities that properly captures the front propagation as a result of the injection.

We demonstrate the results using synthetic and field applications. The synthetic case involves gas injection in a five spot well configuration. The field example involves steam injection into a heavy oil reservoir at Pad 31 in the Peace River Field (Alberta, Canada) presented in the previous chapter. The results clearly show that inversion for the flow properties based upon onset time is more robust and less nonlinear.

4.2 Introduction

Reservoir model calibration, also known as history matching, is an essential tool for the prediction of fluid displacement patterns and related decisions concerning reservoir management and field development. Recently, the use of time-lapse geophysical data for the characterization of flow properties in the subsurface has been increased significantly, and a number of successful field experiences of reservoir management have used time-lapse seismic information (Behrens et al. 2002; Fahimuddin et al. 2010; Landrø et al. 2001; Landrø et al. 1999; Watanabe et al. 2017). The integration of time-lapse seismic data usually involves least-squares-based minimization to match the observed and calculated response (Dadashpour, Mohsen et al. 2010; Dadashpour et al. 2009; Falcone et al. 2004; Gosselin et al. 2003; Gosselin et al. 2001; Rey et al. 2009; Rey et al. 2012; Rwechungura, R.W. et al. 2012; Vasco 2004; Watanabe et al. 2017), where the objective function mostly focuses on amplitude, traveltime, and waveform matching (Vasco et al. 2015).The solutions of such inverse problems, however, known to define an ill-posed such that the solution of geologic parameters is always non-unique and potentially unstable. While this problem can be partially mitigated by including additional regularization terms, penalizing attributes of the model such as its spatial roughness or its vector norm (Menke 2012), a fundamental challenge remains in specifying the relationship between the geophysical properties and reservoir properties, which still can be highly nonlinear. This can cause the solution to converge to a local minimum, leading to an inadequate history match (Cheng et al. 2005).

Recently, the onset time based method has shown a great potential for incorporating seismic data into high-resolution reservoir models (Hetz et al. 2017; Vasco et al. 2015; Vasco et al. 2014). The onset times are defined as the calendar times at which geophysical observations begin to deviate from their initial or background values above a pre-defined threshold value. It allows the compression of multiple seismic surveys into a single map of front propagation, which can be used for dynamic model updating (Hetz et al, 2017). As noted in the previous chapter it is also less sensitive to the unknowns in the petro elastic model. The onset time approach is analogous to "arrival-time match." Instead of matching the amplitude change of a geophysical observation directly, we relate the change in the geophysical property to the arrival time of a saturation/pressure front.

Such arrival times can often be linked to flow properties(Vasco et al. 2014). For example, (Vasco and Datta-Gupta 2001) have shown that the saturation arrival time can be related directly to the permeability, and it seemed to be more robust even when the initial model deviates strongly from the final solution. (Vasco 2011) derived an expression for the velocity of the saturation and pressure front and showed that it has a direct relationship to the reservoir flow properties. Several papers (Datta-Gupta et al. 2002; He et al. 2002; Vasco and Datta-Gupta 1999; Vasco et al. 1998) derived an expression that relates the trace arrival time to variations in permeability. In those papers, the integration of dynamic data is curried out using a two-step iterative inversion that involves travel-time matching followed by a conventional amplitude match. The showed that the major part of the production data misfit reduction occurs during the

traveltime inversion. In the field of flow properties history matching, Cheng et al. (2005) used quantitative measures of nonlinearity to compare the travel-time inversion and amplitude inversion for production-data integration. This study found that the travel time problem is quasi-linear and thus converges more readily than the highly nonlinear amplitude matching problem. (Luo and Schuster 1991) and (Zhou et al. 1997)arrived at the same conclusion in the context of seismic inversion.

In this chapter, the benefits of onset time inversion for seismic data integration in terms of nonlinearity and convergence properties is examined. We discuss the mathematical foundation for the measure of nonlinearity and its implications on the seismic-data integration. We quantitatively investigate the extent of nonlinearity in onset-time inversion and amplitude inversion. In particular, we show that the nonlinearity in onset-time inversion is smaller than that of the amplitude inversion. This leads to better convergence properties and a robust method for seismic-data integration. We illustrate our results using both synthetic and field applications. The field example involves steam injection into a heavy oil reservoir at Pad 31 in the Peace River (Alberta, Canada) with daily time lapse seismic surveys (in terms of two-way travel time) recorded by a permanently buried seismic monitoring system. In our specific application, we have used time lapse data from a Cyclic Steam Stimulation (CSS) cycle in the pad with a total of 45 seismic surveys. The results clearly demonstrate the benefits of the onset time inversion to handle large number of seismic surveys by compressing them into a single map. In particular, the onset inversion appears to outperform the amplitude inversion in reconciling the geologic model to the seismic data response.

4.3 Background and Approach

4.3.1 Onset Time Inversion and Amplitude Inversion

As discussed in chapter 3, the traditional approach to time lapse seismic data integration uses multiple seismic surveys (whenever available) and integrates seismic magnitude (or change in the magnitude) thereof via dynamic modelling and history matching. For a given location and time the amplitude inversion attempts to match the observed seismic response (e.g. acoustic impedance) and the simulated seismic response directly, as shown in Figure 4.1a. In contrast, the onset time inversion attempts to match, for a given location, the time at which measured time-lapse attributes begin to deviate from their initial values above a pre-defined threshold value, illustrated in Figure 4.1b. As mentioned in the introduction, the onset time inversion is analogous to the travel time inversion.

Such an approach removes the requirement that we map a change in a geophysical property to a specific change in fluid saturation and/or pressure (Vasco et al. 2014). The advantages of travel-time inversion are well documented in geophysics literature. For example, (Luo & Schuster, 1991) showed that travel-time inversion is quasilinear as opposed to amplitude inversion, which can be highly nonlinear. Amplitude inversion typically works well when the prior model is close to the solution. In this section, we will quantitatively investigate the relative merits of the different methods in terms of nonlinearity and convergence properties.

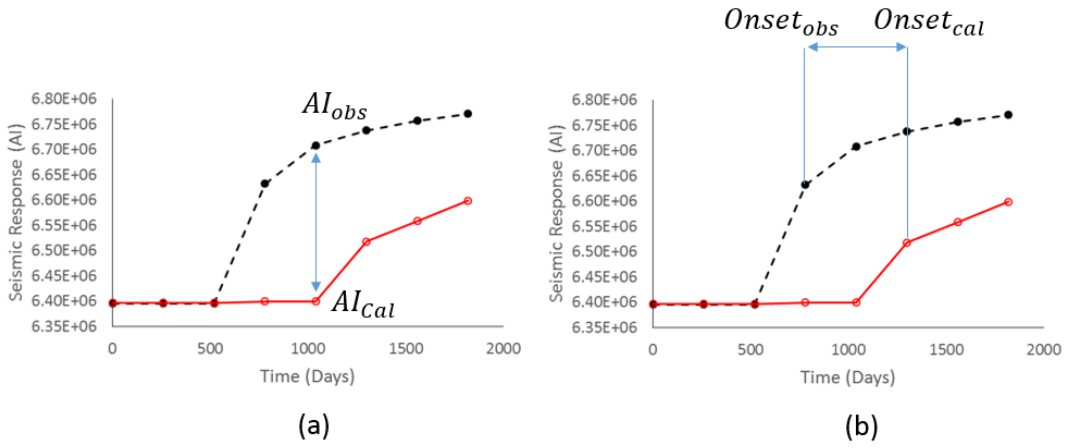

Figure 4.1 Seismic response at a given location as a function of time, (a) amplitude inversion (b) onset time inversion

4.3.1 Measure of Nonlinearity

Here, our goal is to characterize and assess the nonlinearity of the inverse problem to gain insight about the robustness and efficiency of seismic data integration approaches. There are several methods for quantifying the degree of nonlinearity in parameter estimation problems. In this study, the geometric framework for studying nonlinear least squares models was proposed by Bates and Watts (1980).(Grimstad and Mannseth 2000), used this method to investigate the relationship between nonlinearity, scale, and sensitivity in parameter-estimation problems. Cheng et al. (2005) applied this measure to examine the nonlinearities in travel-time and amplitude inversion of production data integration. In this study, the measure of the curvature is used to quantitatively measure

the nonlinearities in onset time and amplitude inversion. If the seismic response is given by F, then a measure of the curvature is given by

$$\kappa = \frac{\left\| F_{mm} \right\|}{\left\| F_m \right\|^2}, \tag{4.1}$$

where F_m is the vector of the first-order derivatives with respect to the parameter vector m, F_{mm} is the vector of second-order derivatives. κ represents the inverse of a radius of the circle that best approximates the outcome locus F in the direction of F_m at m. Smoother and more linear outcome will have smaller curvature (larger radius) and thus a smaller measure of nonlinearity, as illustrated in Figure 4.2.

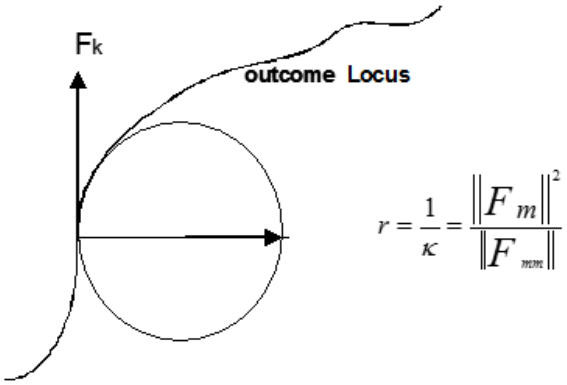

Figure 4.2 Geometric meaning of the measure of nonlinearity

In our application, we measure the nonlinearity at each iteration during the inversion. Since we usually have large numbers of physical observation points (e.g. the location where the seismic data observed), we plot the nonlinearity at the observed location for a given iteration.

Bates and Watts (1980) separate the nonlinearity measures into parameter-effect curvature and intrinsic curvature; thus, they decompose the second-order derivative F_{mm} into one component parallel to the tangent plane defined by F_m for all directions and another component normal to that plane. Here, the tangent vector F_m and the second-order derivative F_{mm} are essentially obtained from the sensitivity calculations. The sensitivity computation to relate perturbation in the geophysical observation to a perturbation in the flow properties is described in detail in the previous chapters.

For the amplitude inversion, the sensitivity is given as

$$G(t_i)=\left(\frac{\partial AI(t_i)}{\partial k_1},\frac{\partial AI(t_i)}{\partial k_2},\cdots,\frac{\partial AI(t_i)}{\partial k_{n_b}}\right)^T , \tag{4.2}$$

where we use **Eq.2.45** to calculate the sensitivity of the acoustic impedance with respect to grid block permeability $\frac{\partial AI}{\partial k}$.

The sensitivity of the onset time inversion can be given as

$$G(t_i)=\left(\frac{\partial OT(t_i)}{\partial k_1},\frac{\partial OT(t_i)}{\partial k_2},\cdots,\frac{\partial OT(t_i)}{\partial k_{n_b}}\right)^T . \tag{4.3}$$

Here **Eq.3.5** is used to relate perturbations in flow properties to perturbations in the onset time, $\frac{\partial OT}{\partial k}$.

To account the variation in units order, we need to normalize the parameters or use a linear transformation to obtain a meaningful solution. Simply expressing the parameters in the original units can be a bad choice because parameters of different types can be of different numerical orders(Duijndam 1988a, 1988b). There are several options to achieve that: (1) to express the parameters in units that correspond with the parameter ranges of interest for the problem; (2) to take the a priori standard deviations as units; and (3) to statistically normalize the parameters with the transformation so that the transformed parameters have the identity matrix as a priori covariance matrix. Here we use option 3 to express the tangent vector F_m and second-order derivative F_{mm}

$$F_k(t_i) = \begin{bmatrix} J_y \\ J_x \end{bmatrix} = -\begin{bmatrix} C_n^{-\frac{1}{2}} G(t_i) \\ C_x^{-\frac{1}{2}} \end{bmatrix}, \tag{4.4}$$

in which G is the sensitivity, C_n is the data covariance and C_x is the model parameter covariance. The second-order derivative F_{mm}

can be written as the sum

$$F_{mm}(t_i) = H_x + H_y , \tag{4.5}$$

where H_y is the contribution of the data,

$$H_y = J_y^T J_y \tag{4.6}$$

and H_x is due to the a priori information

$$H_x = J_x^T J_x = C_x^{-1} . \tag{4.7}$$

We use the statically normalizing $D = C_x^{\frac{1}{2}}$ to obtain

$$F_{mm} = D^T * H * D = C_x^{\frac{1}{2}} * H_y * C_x^{\frac{1}{2}} + I \quad . \tag{4.8}$$

Now we can calculate the nonlinearity measure using **Eq.4.5** according to the theory of Bates and Watts (1980).

4.4 Applications

4.4.1 Five–Spot Synthetic Case

We now consider a two-dimensional synthetic application to demonstrate the procedure. This is a three-phase reservoir model with a five spot pattern. The model of initial and reference permeability is the same as the one we used in chapter III. PVT properties are in Figure 4.3 and Figure 4.4. This case has a gas injector at the center of the reservoir , and thus, the reservoir has not only dissolved gas but also free gas from a gas injector.

The description of the model is given in Table 4.1.

Table 4.1 General parameters of 2D model for history matching

Parameters	Input Values
Grid number	(nx,ny,nz) = (50,50,1)
DX	30 [ft]
DY	30 [ft]
DZ	10 [ft]
Porosity	0.15
Rock compressibility	3.8 E-06 [1/psi]
Oil density	49.1 [lb/cf]
Water density	64.79 [lb/cf]
Gas density	0.065 [lb/cf]
Water viscosity	1.0 [cp]
Water formation volume factor	1.0 [rb/stb]
Initial reservoir pressure	3000 [psi]
Injection constrain	3200 [psi]
Production constrain	200 [rb/day]

***Values for water and rock are at the reference pressure of 3000 psi**
***Density is surface condition (14.7 psi)**

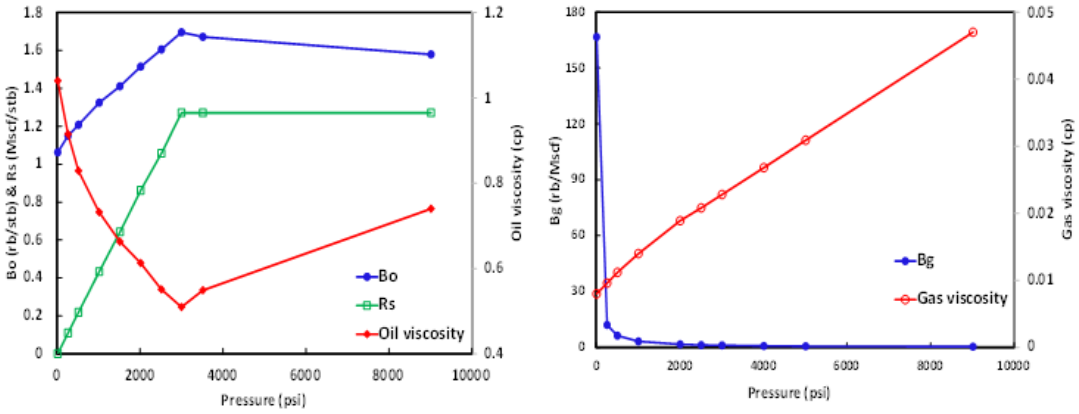

Figure 4.3 Oil and gas PVT properties

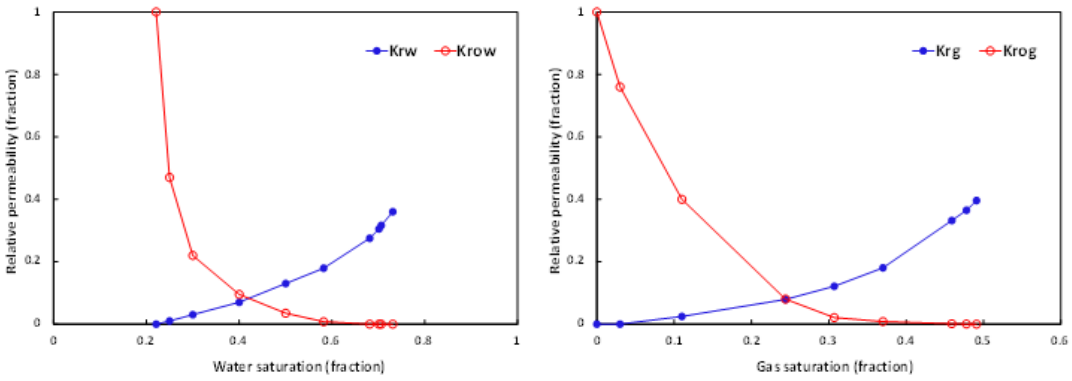

Figure 4.4 Three-phase relative permeability data

Our amplitude inversion is based on acoustic impedance changes over the gas injection interval. The observed seismic data were generated from the reference model using a commercial reservoir simulator and the petro elastic model. Over an interval of 450 days, a total of 15 time-lapse seismic surveys (30 days each) in the form of elastic acoustic impedance maps, are available for integration. To examine the effects of amplitude perturbations, we added 7% Gaussian noise to the amplitudes before estimating the onset times. The magnitude of the noise is specified with respect to the amplitude at a specific location. Figure 4.5 shows the acoustic impedance change (that is, the observation) over the injection interval with and without the noise. Figure 4.6 shows the acoustic impedance response over the interval with the added Gaussian noise from two points at the model.

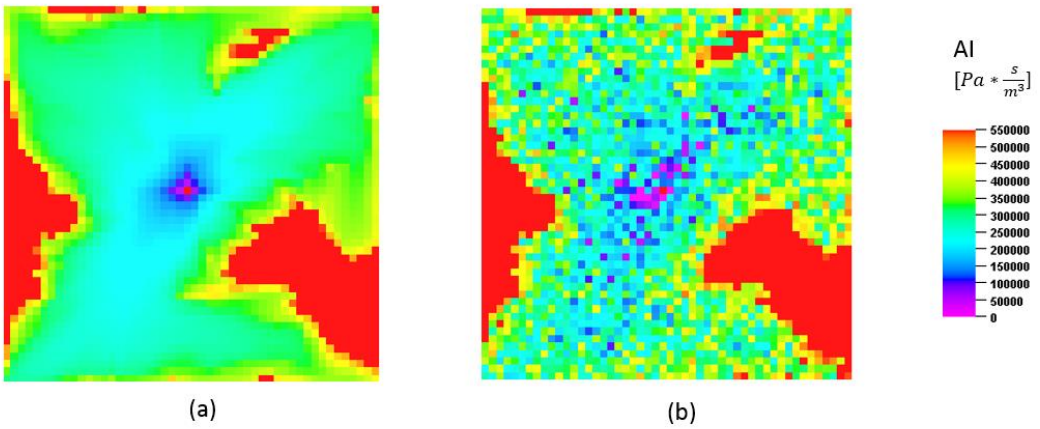

Figure 4.5 The seismic observations for the AI change inversion. (a) AI change over the interval (noise-free). (b) AI change over the interval (with 7% added Gaussian noise).

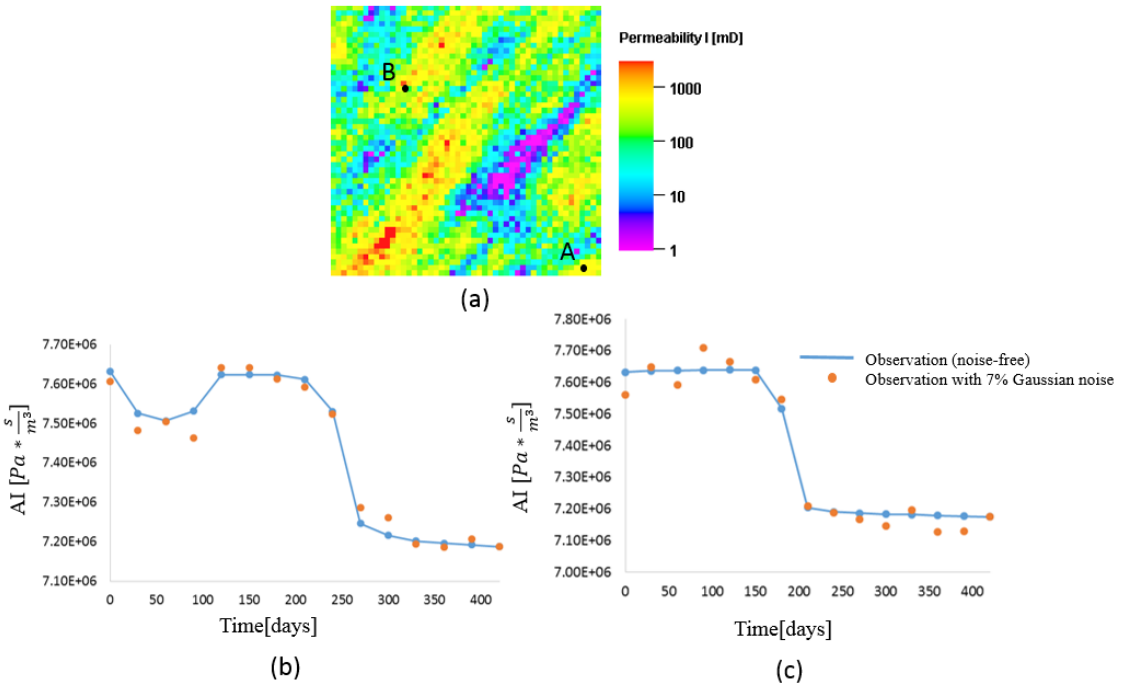

Figure 4.6 Time series of the acoustic impedance response for points A and B (a) Permeability model used to generate the observed data. (b) The acoustic impedance response of point A over the entire interval. (c) The acoustic impedance response of point B over the entire interval

The random amplitude deviations, shown in Figure 4.6, lead to seismic signals even when there are no dynamic changes within the reservoir and thus a need for a threshold value to distinguish between noise and meaningful signal. In this example, we define the threshold to be 7% below the acoustic impedance of the baseline survey (e.g. before the injection started). This decrease above the threshold corresponds to a decrease in the bulk density and velocity of the seismic waves, which results from replacement of

"harder" for "softer" reservoir fluids. The observed onset map inferred from the observed acoustic impedance is shown in Figure 4.7.

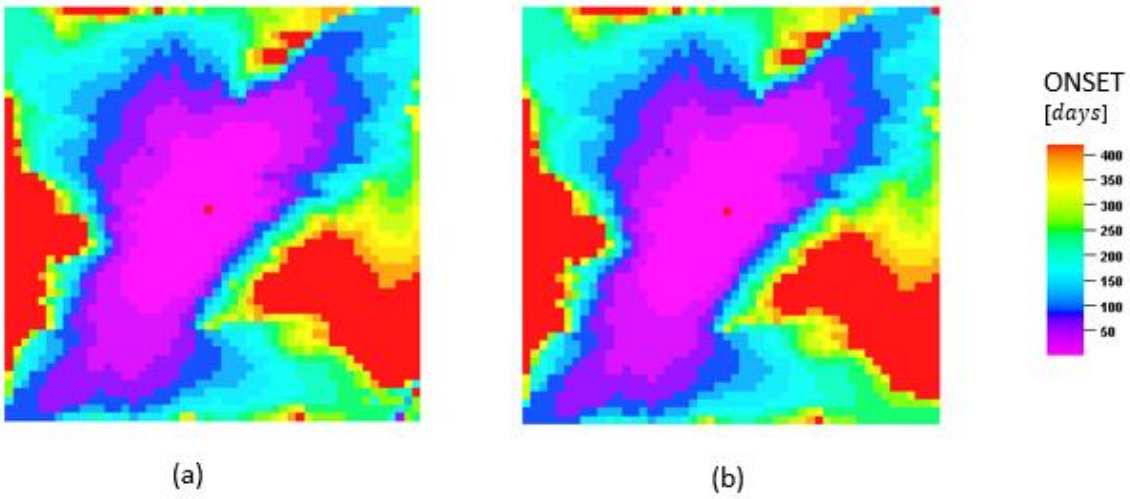

Figure 4.7 The seismic observations for the onset time inversion. (a) Onset time map over the interval (noise-free). (b) Onset time map over the interval (with 7% added Gaussian noise).

In this example, we compare the relative performance of onset time and amplitude inversion. In addition, we investigate the nonlinearities inherent in these approaches.

The normalized misfit reduction is shown in Figure 4.8 for both inversion methods as a function of the number of iterations. The reduction of the onset time objective function as compared to the acoustic impedance change implies that the onset time approach

properly capture the gas propagation in the reservoir. Figure 4.9 and Figure 4.10 show the fit to time lapse seismic for both cases, with a significant improvement in the onset time map. The updated permeability field for both cases is shown in Figure 4.11. It appears that the onset time approach is able to better identify the low permeability barrier located in the right lower corner of the model.

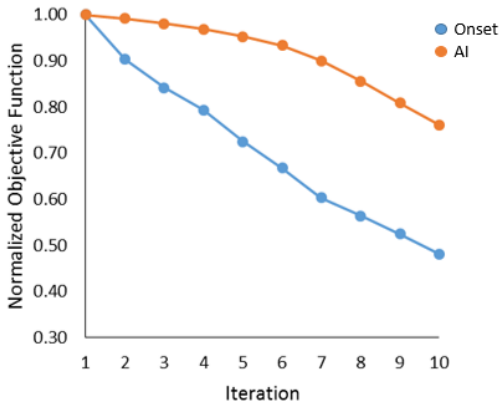

Figure 4.8 Objective function as a function of the number of iterations of the inversion algorithm

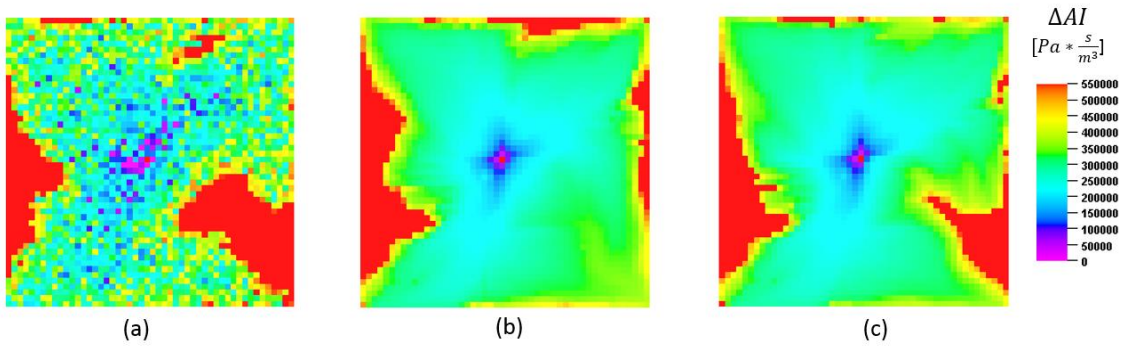

Figure 4.9 The acoustic impedance changes over the injection interval. (a) AI changes of the reference model, (b) AI changes of the initial model, and (c) AI changes of the updated model.

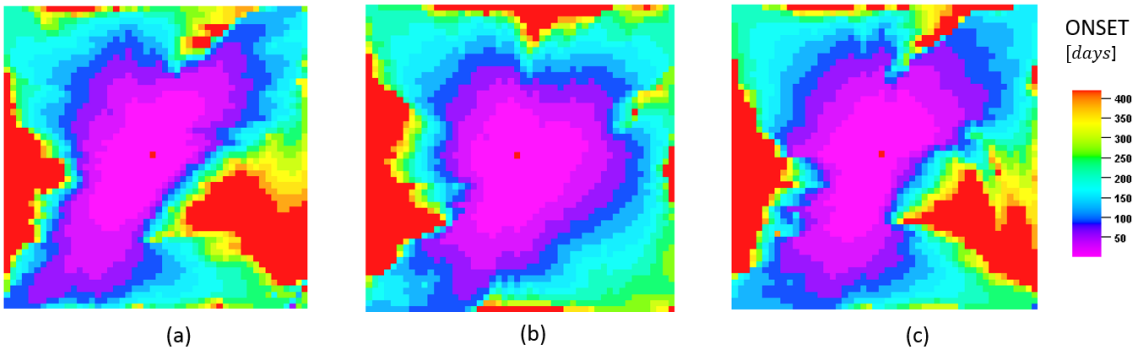

Figure 4.10 The onset time map over the injection interval. (a) Onset time map of the reference model, (b) onset time map of the initial model, and (c) onset time map of the updated model.

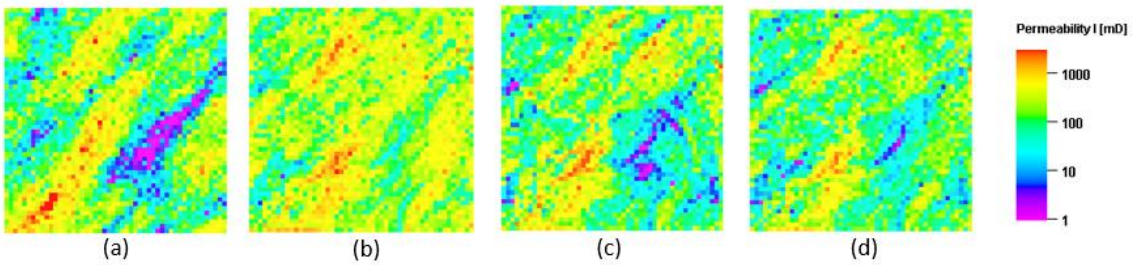

Figure 4.11 Permeability fields for the five-spot synthetic test. (a) Reference model, (b) Initial model, and (c) updated model based on Onset Time data integration, (d) updated model based on AI changes data integration.

In Figure 4.12 we compare the overall measure of the nonlinearity at each iteration for both inversion methods. It is observed that the magnitude of nonlinearity of the amplitude inversion is two to three order of magnitude more nonlinear than the onset time inversion. This is partly the reason for the better conversion results, shown in Figure 4.8.

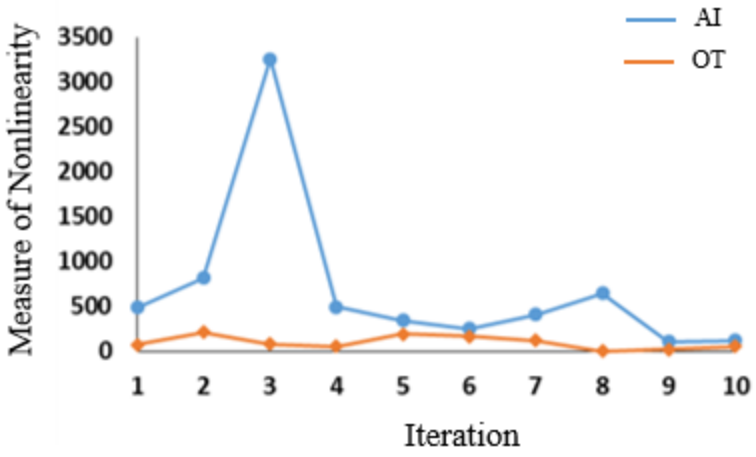

Figure 4.12 Measure of nonlinearity for the gas injection example

To emphasize the differences of the nonlinearity measurement between the amplitude and onset time inversion, in Figure 4.13 and Figure 4.14 we plot the measure of the nonlinearity for each method as a function of the physical location at which the seismic measurement was observed. Note that the nonlinearity of the onset time is one order smaller than of the amplitude inversion.

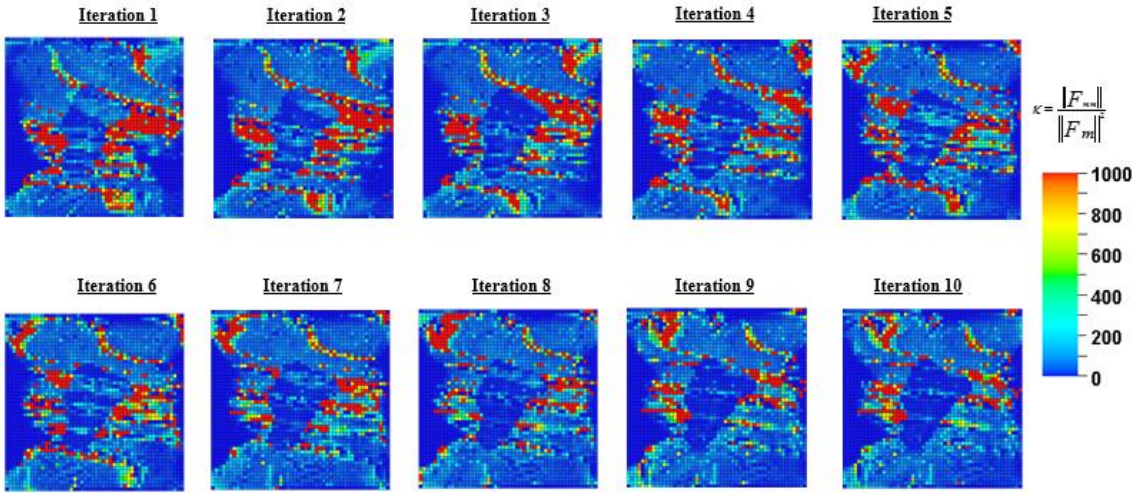

Figure 4.13 Measure of nonlinearity of the amplitude inversion for the gas injection example as a function of the physical location.

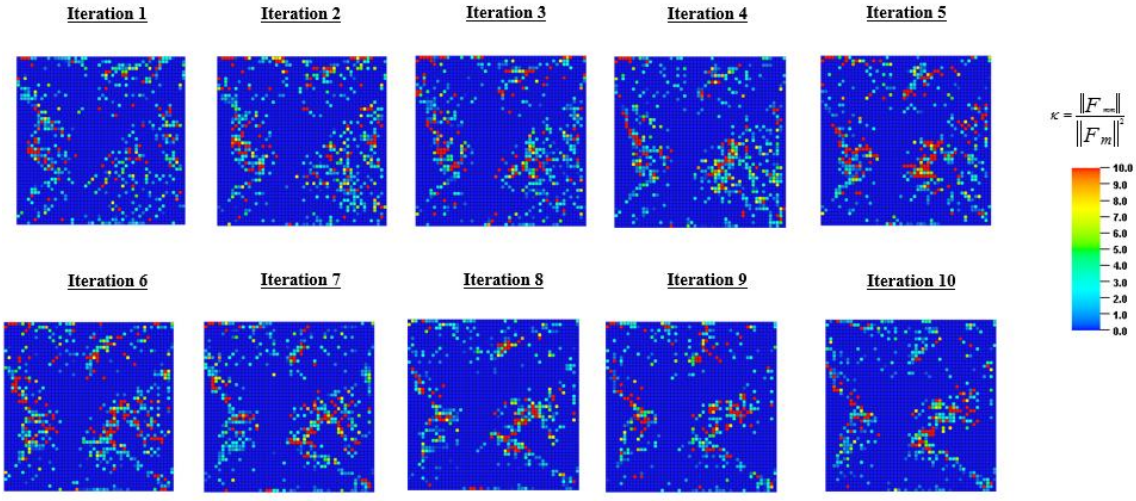

Figure 4.14 Measure of nonlinearity of the onset time inversion for the gas injection example as a function of the physical location.

It is observed that the amplitude inversion displays notably higher measure of the nonlinearity with a significantly large number of locations (red color). To gain some insight into the variation of the nonlinearity, in Figure 4.15 we plot the updated time lapse seismic together with the partial derivatives of each of the methods (e.g. onset time, acoustic impedance) with respect to gas saturation. The partial derivatives of the onset time (Figure 4.15a) are at the locations where the contours of the onset time change, which clearly show the gas front propagation throughout the injection interval. On the other hand, the partial derivatives of the acoustic impedance do not seem to indicate a clear underlying physics. In fact, the nature of the acoustic impedance maps, which couple the effects of different physics, make the amplitude inversion to be more nonlinear with significantly a dense sensitivity matrix.

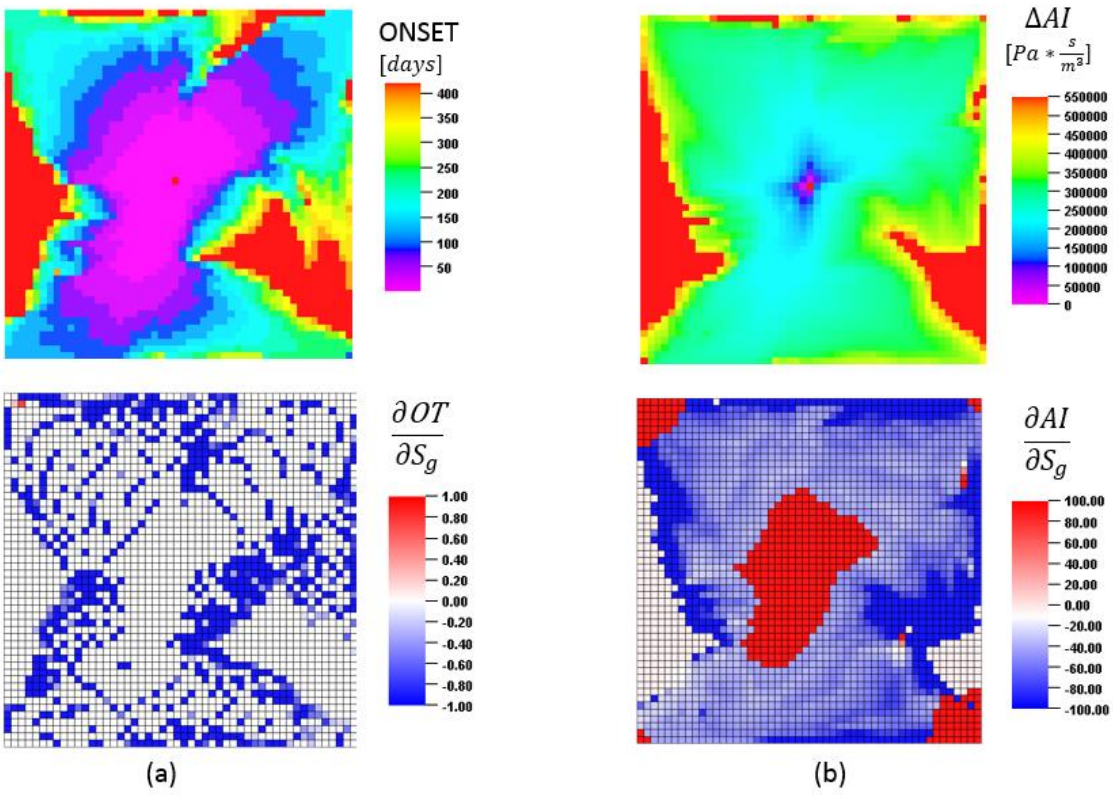

Figure 4.15 Updated seismic response and the partial derivatives of the seismic with respect to gas saturation at the last iteration. (a) Onset time and (b) acoustic impedance changes

4.4.2 The Peace River Cases

Our field application is a heavy oil reservoir at Pad 31 in the Peace River Field (Alberta, Canada) with daily time lapse seismic surveys recorded by a permanently buried seismic monitoring system(Lopez et al. 2015). The description of the field and the seismic observations is given in chapter III. As we showed in the synthetic case, our goal is to compare the relative performance of the onset time and the amplitude inversion by

investigating the nonlinearities inherent in these approaches. The amount and the nature of the recorded time shift data make it extremely challenging and time consuming for amplitude inversion. Thus, for this demonstration we will focus on the first 45 days of the injection interval. In the amplitude inversion, our seismic data integration is based on the travel time changes in the seismic wave propagation across the reservoir between the start of the cycle and 45 days of steam injection, as shown in Figure 4.16.

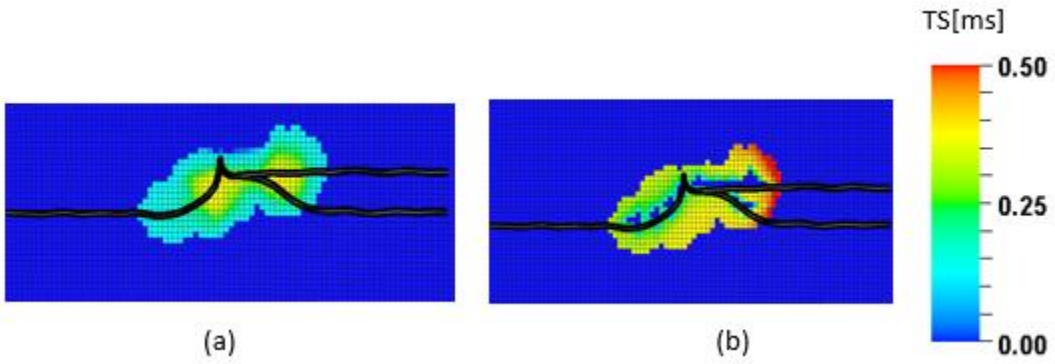

Figure 4.16 The time shift map over the first 45 days of injection. (a) Observed data ,(b)initial model.

For the onset time inversion, we follow the same procedure we presented in the synthetic case to generate the onset time map, as shown in Figure 4.17.

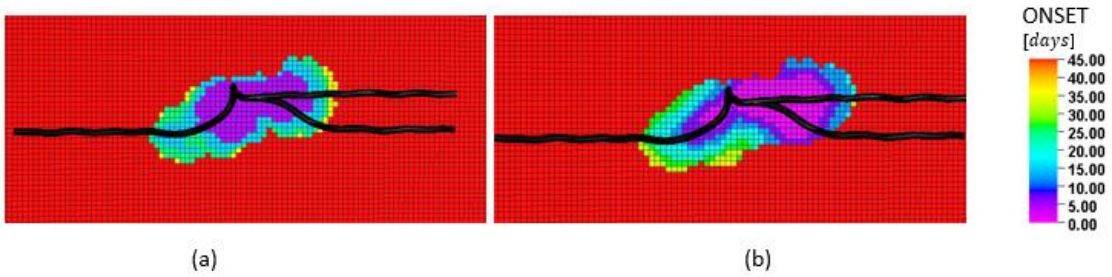

Figure 4.17 The onset time map over the injection interval. (a) Onset time map of the reference model, (b) onset time map of the initial model

The data misfit reduction from the prior model is shown in Figure 4.18. Still even when we started with an initial model after the global update, the amplitude inversion was not able to resolve or calibrate the model. Figure 4.19and Figure 4.20 show the fit to time lapse seismic for both inversion methods. The updated onset time response significantly improved from the initial model due to local adjustments of the permeability. On the other hand, the time shift map (Figure 4.19) shows a small improvement from the prior model. The fact that the time shift is very sensitive to the petro elastic properties, as described in detail in the previous chapter, leads to high degree of nonlinearity in the amplitude inversion. The updated permeability fields for both cases are shown in Figure 4.11Figure 4.21 and Figure 4.22. The amplitude inversion seems to increase the permeability around the well. On the contrary, the permeability updates based on the onset time inversion suggest an increase in the permeability around the vertical part and decrease at the east part of the horizontal well. The onset time was able to identify the

injectivity profile along the horizontal well, which in the case of steam injection in heavy oil, is shown by the increased permeabilities.

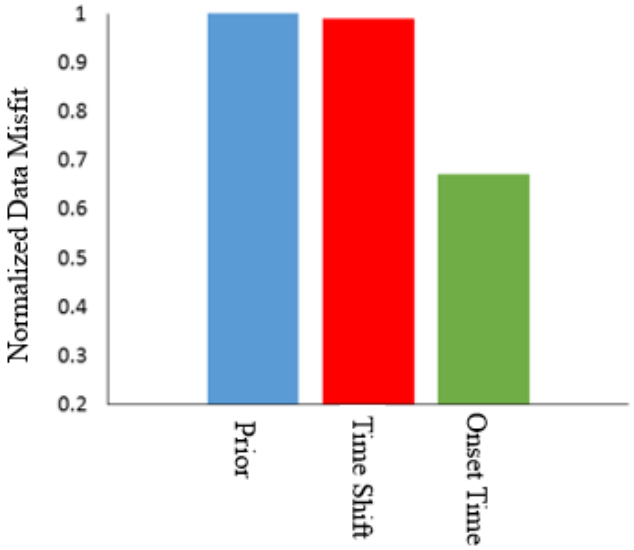

Figure 4.18 The comparison of normalized objective function for amplitude (time shift) inversion, and onset time inversion

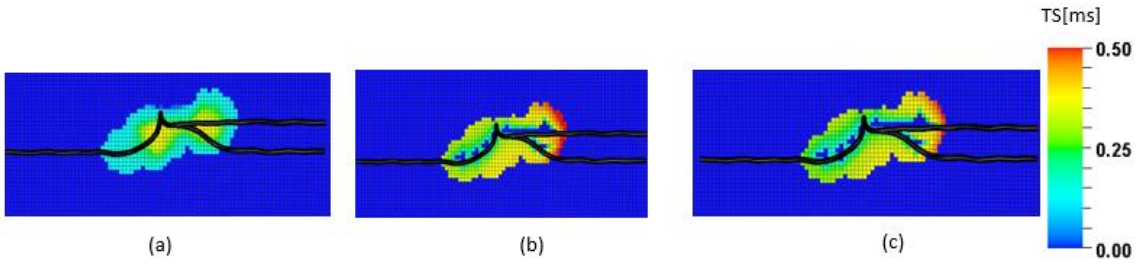

Figure 4.19 Top view of the time shift map after the history matching (a) Observed data, (b) after global update, and (c) the final updated model

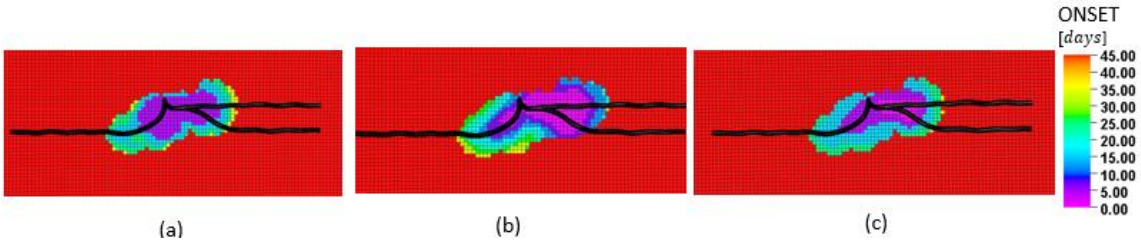

Figure 4.20 Top view of the onset time map after the history matching (a) Observed data, (b) after global update, and (c) the final updated model

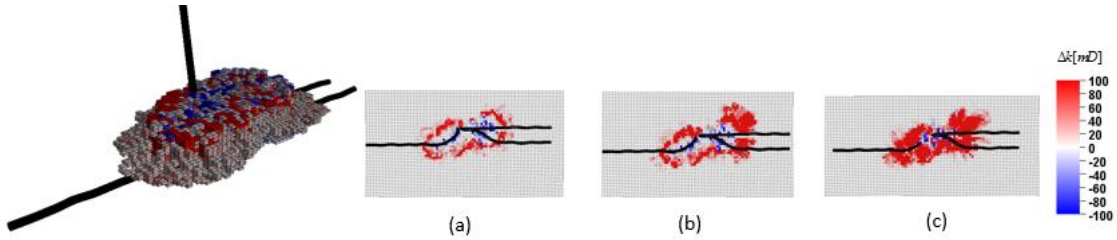

Figure 4.21 Permeability model change (final-prior) for the amplitude inversion (time shift). (a) Top view of layer 15, (b) Top view of layer 18 and (c) top view of layer 20

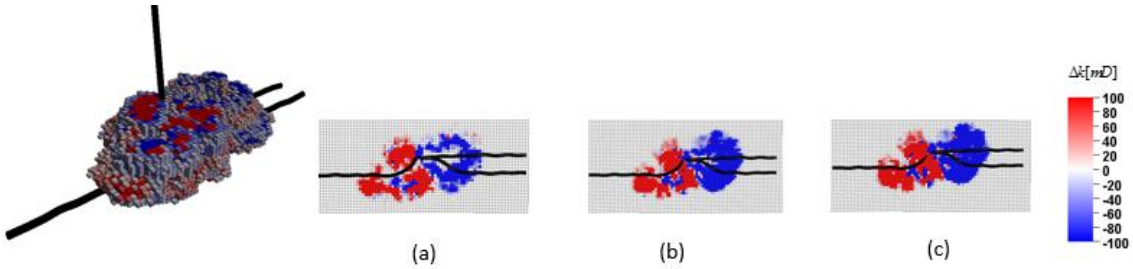

Figure 4.22 Permeability model change (final-prior) for the onset time inversion. (a) Top view of layer 15, (b) Top view of layer 18 and (c) top view of layer 20

As we illustrated in the synthetic case, in Figure 4.23 and Figure 4.24 we plot the measure of the nonlinearity for each method as a function of the physical location at which the seismic measurement was observed. Note that the nonlinearity of the onset time is two orders smaller than that of the amplitude inversion.

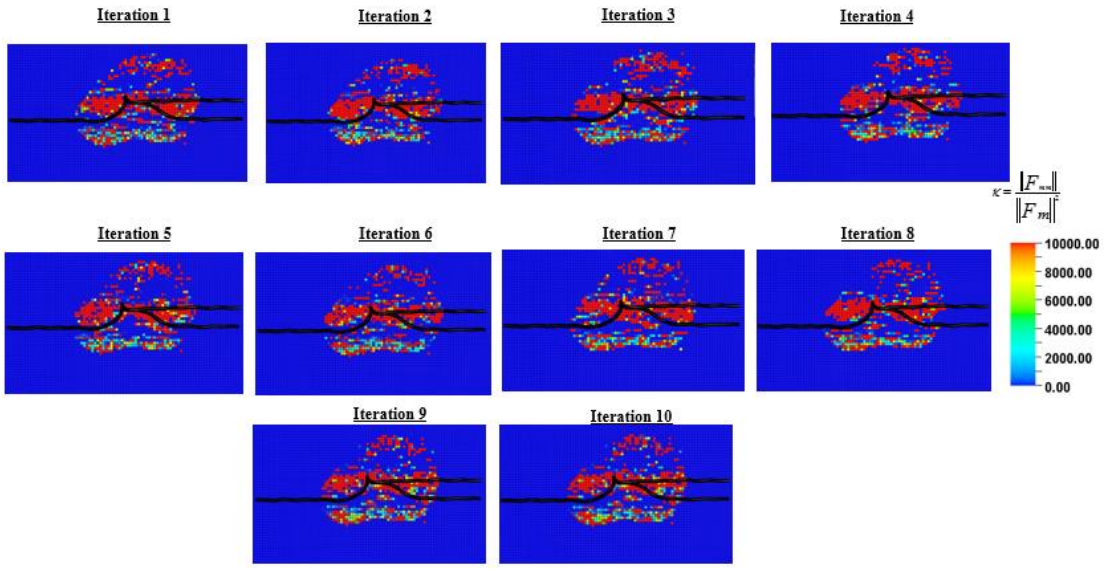

Figure 4.23 Top view of the measure of nonlinearity of the amplitude (time shift) inversion for the field example as a function of the physical location

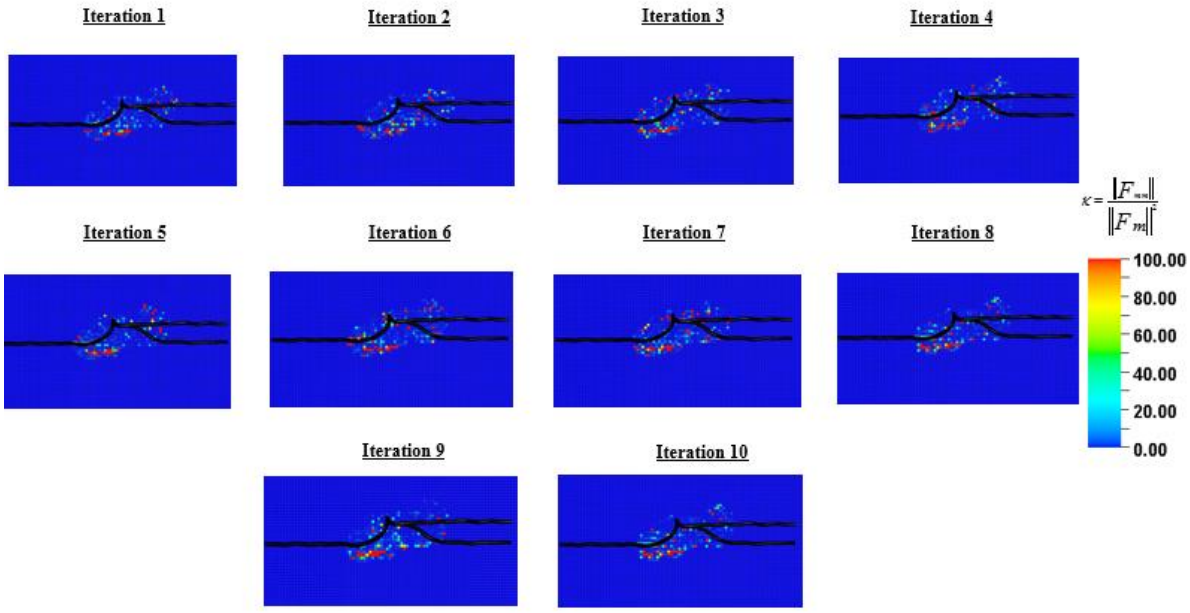

Figure 4.24 Top view of the measure of nonlinearity of the onset time inversion for the field example as a function of the physical location

The measure of the nonlinearities shows that an inversion based on amplitude is orders of magnitude more nonlinear compared to the onset time inversion. In addition, unlike the onset time inversion, the nonlinearity region of the amplitude inversion seems to be spread out from the well. One of the reasons for this nonlinearity comes from the fact that the amplitude inversion accounts for seismic signals that are not directly related to steam propagation. Finally, we plot the partial derivatives of each of the methods (e.g. onset time and time shift) with respect to water saturation in Figure 4.24 and Figure 4.25. As we observed in the synthetic case, the partial derivatives of the onset time (Figure 4.26) are at the locations where the contours of the onset time change, which

clearly show the steam front propagation throughout the injection interval. On the other hand, the partial derivatives of the time shift do not seem to indicate a clear underlying physics, resulting in a significantly dense sensitivity matrix.

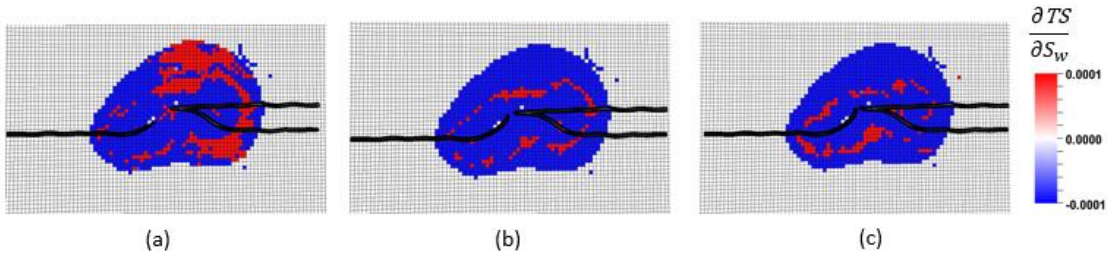

Figure 4.25 The partial derivatives of the time shift with respect to water at the last iteration (a) Top view of layer 15, (b) Top view of layer 18 and (c) top view of layer 20

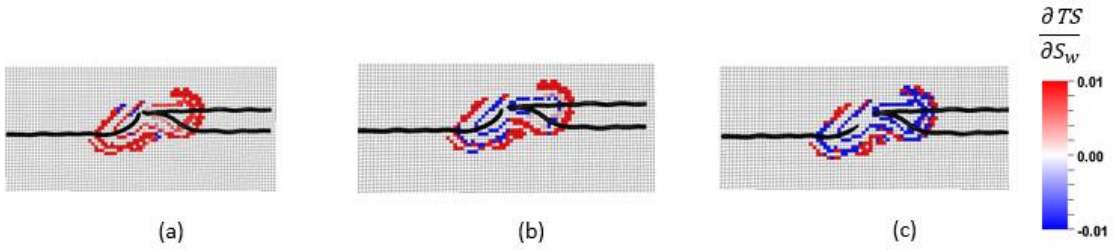

Figure 4.26 The partial derivatives of the onset time with respect to water at the last iteration (a) Top view of layer 15, (b) Top view of layer 18 and (c) top view of layer 20

4.5 Conclusions

In this chapter we compared the ability of the onset time inversion and the amplitude inversion to integrate time lapse seismic data. By applying the geometric concept of curvature, we examined their relative merits using the measures of nonlinearity. The onset time inversion found to be more stable and robust than amplitude inversion for reservoir characterization when frequent seismic surveys are available.

Some of the conclusions from this study are the following:

- We have quantitatively investigated the nonlinearities associated with onset time and amplitude inversion.
- Both the synthetic and field applications show that the nonlinearity of the onset time inversion is orders of magnitude smaller than the amplitude inversion, leading to a better match of the data and an adequate history matched model. Similar conclusions were arrived at by Cheng et al (2005).
- The onset time sensitivities appear to be notably less dense than the amplitude sensitivities. In addition the onset time better identifies the propagation of changes in the reservoir and seems to have quasilinear properties, which leads to improved convergence properties.

CHAPTER V CONCLUSIONS AND RECOMMENDATIONS

5.1 Conclusions

The study summarize the developments and applications of an integrated approach for model calibration using time lapse seismic data. We present a novel approach that integrate frequent time lapse (4D) seismic data into high resolution reservoir models based on seismic onset times. We also show how to indicate the reliability of the estimated solution using an analysis of spatial resolution. Throughout this dissertation we illustrated our methods using synthetic and field applications. The main findings are listed below:

- We presented a method to quantify the resolution and the spatial averaging associated with estimated permeabilities derived through an efficient history matching approach of multi-scale data integration, accounting for both pressure and saturation effects.
- The model resolution matrix is useful for assessing the inversion results in underdetermined problems.
- In seismic data, the spatial resolution points out the importance of accounting for both saturation and pressure changes to constrain the parameter estimation. It appears that pressure is more sensitive to barriers to flow in the global updates, whereas in the flow unit the barriers to flow and small variations in permeability are better determined by saturation.

- We propose a novel and computationally efficient approach for time lapse seismic integration using the onset time which is able to efficiently display the front propagation in order to update the flow properties.
- Our synthetic and field applications show that unlike seismic impedance, the onset times appear to be relatively insensitive to the petro elastic model but sensitive to the steam/fluid propagation, temperature and pressure.
- The onset time leads to a significant data reduction and provides a practical and faster approach that allows testing alternative dynamic realizations, making the algorithm suitable for large field applications with frequent seismic surveys.
- The Peace River application demonstrates the feasibility and the robustness of the hierarchical workflow to integrate onset times and pressure data.
- The compression of the frequent seismic surveys into a single set of onsets assists efficient history matching using the population-based technique that requires a large number of simulation runs.
- In the local stage, where the flow properties were adjusted on a cell by cell basis, the algorithm was able to improve the location of the water/steam front and identified the location of increased permeabilities, which in case of steam injection in heavy oil is equivalent with stimulated zones.
- We have quantitatively investigated the nonlinearities associated with onset time and amplitude inversion.

- Both the synthetic and field applications show that the nonlinearity of the onset time inversion is orders of magnitude smaller than the amplitude inversion, leading to a better match of the data and an adequate history matched model.
- The onset time sensitivities appear to be notably less dense than the amplitude sensitivities. In addition the onset time better identifies the propagation of changes in the reservoir and seems to have quasilinear properties, which leads to improved convergence properties.

5.2 Recommendations

The use of seismic data for quantitative calibration of reservoir models is an extremely difficult task. Although our workflow works well, there is still large room for improvement when applied to complex reservoir conditions.

Several recommendations are listed below:

- Indicating the reliability of the estimated solution is an important tool in history matching. We recommend implementing an adaptive adjustment algorithm that accepts/ rejects updates based on the analysis of spatial resolution.
- We have observed that the onset time is sensitive to both the permeability and the porosity. We recommend implementing streamline-based inversion methods that involves updates of the permeability and porosity.
- In our field application we integrate the seismic and the BHP data in a sequential order. We suggest to try a joint inversion with a multiscale approach that integrate the onset time and the production data simultaneously.

- Our streamline based onset time sensitivity is a reasonable approximation for the history matching. However, in case of steam injections we recommend developing a new algorithm that accounts for temperature changes along the streamline.

REFERENCES

Aki, K. and Richards, P.G. 2002. *Quantitative Seismology* Original edition. ISBN 0935702962.

Anterion, F., Eymard, R., and Karcher, B. 1989. Use of Parameter Gradients for Reservoir History Matching. In *SPE Symposium on Reservoir Simulation*: Society of Petroleum Engineers. ISBN 1555635725.

Arenas, E., van Kruijsdijk, C., and Oldenziel, T. 2001. Semi-Automatic History Matching Using the Pilot Point Method Including Time-Lapse Seismic Data. In *SPE Annual Technical Conference and Exhibition*: Society of Petroleum Engineers. ISBN 1555631541.

Arts, R., Brevik, I., Eiken, O. et al. 2000. Geophysical Methods for Monitoring Marine Aquifer Co2 Storage–Sleipner Experiences. In *5th International Conference on Greenhouse Gas Control Technologies, Cairns, Australia*.

Aster, R.C., Borchers, B., and Thurber, C. 2013. *Parameter Estimation and Inverse Problem*. San Diego: Academic Press.

Backus, G. and Gilbert, F. 1968. The Resolving Power of Gross Earth Data. *Geophysical Journal International* **16** (2): 169-205.

Backus, G.E. and Gilbert, J. 1967. Numerical Applications of a Formalism for Geophysical Inverse Problems. *Geophysical Journal International* **13** (1-3): 247-276.

Barker, T. and Xue, Y. 2016. Inversion of Continuous 4d Seismic Attributes to Reveal Daily Reservoir Changes. In *Seg Technical Program Expanded Abstracts 2016*: Society of Exploration Geophysicists.

Bates, D.M. and Watts, D.G. 1980. Relative Curvature Measures of Nonlinearity. *Journal of the Royal Statistical Society. Series B (Methodological)*: 1-25.

Behrens, R., Condon, P., Haworth, W. et al. 2002. 4d Seismic Monitoring of Water Influx at Bay Marchand: The Practical Use of 4d in an Imperfect World. *Spe Reservoir Evaluation & Engineering* **5** (5): 410-420. DOI: 10.2118/79961-PA

Bhark, E.W., Jafarpour, B., and Datta-Gupta, A. 2011. A Generalized Grid Connectivity-Based Parameterization for Subsurface Flow Model Calibration. *Water Resources Research* **47**. DOI: Artn W0651710.1029/2010wr009982

Chavent, G., Dupuy, M., and Lemmonier, P. 1975. History Matching by Use of Optimal Theory. *Society of Petroleum Engineers Journal* **15** (01): 74-86.

Cheng, H., Datta-Gupta, A., and He, Z. 2005. A Comparison of Travel-Time and Amplitude Matching for Field-Scale Production-Data Integration: Sensitivity, Nonlinearity, and Practical Implications. *Spe Journal* **10** (1): 75-90. DOI: 10.2118/84570-Pa

Cheng, H., Dehghani, K., and Billiter, T. 2008. A Structured Approach for Probabilistic-Assisted History Matching Using Evolutionary Algorithms: Tengiz Field Applications. Paper SPE 116212 presented at the SPE Annual Technical Conference and Exhibition, Denver, Colorado, USA, 116221-116224 September.

Dadashpour, M., Ciaurri, D.E., Mukerji, T. et al. 2010. A Derivative-Free Approach for the Estimation of Porosity and Permeability Using Time-Lapse Seismic and Production Data. *Journal of Geophysics and Engineering* **7** (4): 351-368. DOI: 10.1088/1742-2132/7/4/002

Dadashpour, M., Echeverría-Ciaurri, D., Kleppe, J. et al. 2009. Porosity and Permeability Estimation by Integration of Production and Time-Lapse near and Far Offset Seismic Data. *Journal of Geophysics and Engineering* **6** (4): 325-344.

Dadashpour, M., Landro, M., and Kleppe, J. 2008. Nonlinear Inversion for Estimating Reservoir Parameters from Time-Lapse Seismic Data. *Journal of Geophysics and Engineering* **5** (1): 54-66. DOI: 10.1088/1742-2132/5/1/006

Datta-Gupta, A. and King, M.J. 2007. *Streamline Simulation: Theory and Practice*: Society of Petroleum Engineers.

Datta-Gupta, A., Vasco, D., and Long, J. 1997. On the Sensitivity and Spatial Resolution of Transient Pressure and Tracer Data for Heterogeneity Characterization. *SPE Formation Evaluation* **12** (02): 137-144.

Datta-Gupta, A., Yoon, S., Vasco, D.W. et al. 2002. Inverse Modeling of Partitioning Interwell Tracer Tests: A Streamline Approach. *Water Resources Research* **38** (6). DOI:10.1029/2001WR000597

Dong, Y. and Oliver, D.S. 2005. Quantitative Use of 4d Seismic Data for Reservoir Description. *SPE Journal* **10** (01): 91-99.

Duijndam, A. 1988a. Bayesian Estimation in Seismic Inversion. Part I: Principles1. *Geophysical Prospecting* **36** (8): 878-898.

Duijndam, A. 1988b. Bayesian Estimation in Seismic Inversion. Part Ii: Uncertainty Analysis1. *Geophysical Prospecting* **36** (8): 899-918.

Eastwood, J., Lebel, P., Dilay, A. et al. 1994. Seismic Monitoring of Steam-Based Recovery of Bitumen. *The Leading Edge* **13** (4): 242-251.

Fahimuddin, A., Aanonsen, S.I., and Skjervheim, J.-A. 2010. 4d Seismic History Matching of a Real Field Case with Enkf: Use of Local Analysis for Model Updating. In *SPE Annual Technical Conference and Exhibition*: Society of Petroleum Engineers. ISBN 1555633005.

Falcone, G., Gosselin, O., Maire, F. et al. 2004. Petroelastic Modelling as Key Element of 4d History Matching: A Field Example. In *SPE Annual Technical Conference and Exhibition*: Society of Petroleum Engineers. ISBN 1555631517.

Foster, D.G. 2007. The Bp 4-D Story: Experience over the Last 10 Years and Current Trends. In *International Petroleum Technology Conference*: International Petroleum Technology Conference. ISBN 1555631843.

Gassmann, F. 1951. Elastic Waves through a Packing of Spheres. *Geophysics* **16** (4): 673-685. DOI: 10.1190/1.1437718

Golub, G.H. and Reinsch, C. 1970. Singular Value Decomposition and Least Squares Solutions. *Numerische mathematik* **14** (5): 403-420.

Gosselin, O., Aanonsen, S., Aavatsmark, I. et al. 2003. History Matching Using Time-Lapse Seismic (Huts). In *SPE Annual Technical Conference and Exhibition*: Society of Petroleum Engineers. ISBN 1555631525.

Gosselin, O., van den Berg, S., and Cominelli, A. 2001. Integrated History-Matching of Production and 4d Seismic Data. In *SPE Annual Technical Conference and Exhibition*: Society of Petroleum Engineers. ISBN 1555631541.

Granville, V., Krivánek, M., and Rasson, J.-P. 1994. Simulated Annealing: A Proof of Convergence. *IEEE transactions on pattern analysis and machine intelligence* **16** (6): 652-656.

Grimstad, A.-A. and Mannseth, T. 2000. Nonlinearity, Scale, and Sensitivity for Parameter Estimation Problems. *SIAM Journal on Scientific Computing* **21** (6): 2096-2113.

Hansen, P.C. 1998. *Rank-Deficient and Discrete Ill-Posed Problems: Numerical Aspects of Linear Inversion*: SIAM. Original edition. ISBN 0898714036.

Hastings, W.K. 1970. Monte Carlo Sampling Methods Using Markov Chains and Their Applications. *Biometrika* **57** (1): 97-109.

He, Z., Yoon, S., and Datta-Gupta, A. 2002. Streamline-Based Production Data Integration with Gravity and Changing Field Conditions. *Spe Journal* **7** (4): 423-436.

Hetz, G., Datta-Gupta, A., Przybysz-Jarnut, J. et al. 2017. Integration of Continuous Time Lapse Seismic Data into Reservoir Models Using Onset Times. In *First EAGE Workshop on Practical Reservoir Monitoring*. ISBN 2214-4609.

Hoffman, B.T., Caers, J.K., Wen, X.-H. et al. 2006. A Practical Data Integration Approach to History Matching: Application to a Deepwater Reservoir. *SPE Journal* **11** (04): 464-479.

Huang, X., Meister, L., and Workman, R. 1997. Reservoir Characterization by Integration of Time-Lapse Seismic and Production Data. In *SPE Annual Technical Conference and Exhibition*: Society of Petroleum Engineers. ISBN 1555633994.

Kam, D., Han, J., and Datta-Gupta, A. 2016. Streamline-Based Rapid History Matching of Bottomhole Pressure and Three-Phase Production Data. In *SPE Improved Oil Recovery Conference*: Society of Petroleum Engineers. ISBN 1613994397.

Kennett, B. 1983. *Seismic Wave Propagation in Stratified Media*: Cambridge University Press Original edition. ISBN 0521239338.

Kennett, B. 2013. *Seismic Wave Propagation in Stratified Media*: ANU Press. Original edition. ISBN 192153673X.

Lanczos, C. 1996. *Linear Differential Operators*: SIAM. Original edition. ISBN 0898713706.

Landrø, M., Digranes, P., and Strønen, L. 2001. Mapping Reservoir Pressure and Saturation Changes Using Seismic Methods-Possibilities and Limitations. *First break* **19** (12): 671-684.

Landrø, M., Solheim, O.A., Hilde, E. et al. 1999. The Gullfaks 4d Seismic Study. *Petroleum Geoscience* **5** (3): 213-226.

Li, R., Reynolds, A., and Oliver, D. 2001. Sensitivity Coefficients for Three-Phase Flow History Matching. In *Canadian International Petroleum Conference*: Petroleum Society of Canada. ISBN 1613991088.

Lopez, J., Wills, P., La Follett, J. et al. 2015. Real-Time Seismic Surveillance of Thermal Eor at Peace River. In *SPE Canada Heavy Oil Technical Conference*: Society of Petroleum Engineers. ISBN 1613994028.

Lumley, D.E. 2001. Time-Lapse Seismic Reservoir Monitoring. *Geophysics* **66** (1): 50-53. DOI: 10.1190/1.1444921

Luo, Y. and Schuster, G.T. 1991. Wave-Equation Traveltime Inversion. *Geophysics* **56** (5): 645-653.

Mavko, G., Mukerji, T., and Dvorkin, J. 2009. *The Rock Physics Handbook: Tools for Seismic Analysis of Porous Media*: Cambridge university press. Original edition. ISBN 0521861365.

Menke, W. 2012. *Geophysical Data Analysis: Discrete Inverse Theory*: Academic press. Original edition. ISBN 0123971608.

Mindlin, R.D. 1949. Compliance of Elastic Bodies in Contact. *Journal of Applied Mechanics* **16**: 259-268.

Paige, C.C. and Saunders, M.A. 1982. Lsqr: An Algorithm for Sparse Linear Equations and Sparse Least Squares. *ACM transactions on Mathematical Software* **8** (1): 43-71.

Parker, R.L. 1994. *Geophysical Inverse Theory*: Princeton university press. Original edition. ISBN 0691036349.

Przybysz-Jarnut, J., Didraga, C., Potters, J. et al. 2015. Value of Information of Frequent Time-Lapse Seismic for Thermal Eor Monitoring at Peace River. In *SPE Annual Technical Conference and Exhibition*: Society of Petroleum Engineers. ISBN 1613993765.

Przybysz-Jarnut, J., Wills, P., Araujo, M. et al. 2016. Combining Frequent 4d Seismic and Mechanistic Reservoir Modeling to Improve the Effectiveness of Steam Injection Operations. In *SPE Annual Technical Conference and Exhibition*: Society of Petroleum Engineers. ISBN 161399463X.

Rey, A., Ballin, P.R., Vitalis, C.F. et al. 2009. Assisted History Matching in an Offshore Turbidite Reservoir with Active Reservoir Management. In *SPE Annual*

Technical Conference and Exhibition: Society of Petroleum Engineers. ISBN 1555632637.

Rey, A., Bhark, E., Gao, K. et al. 2012. Streamline-Based Integration of Time-Lapse Seismic and Production Data into Petroleum Reservoir Models. *Geophysics* **77** (6): M73-M87. DOI: 10.1190/Geo2011-0346.1

Rwechungura, R., Bhark, E., Miljeteig, O. et al. 2012. Results of the First Norne Field Case on History Matching and Recovery Optimization Using Production and 4d Seismic Data. Paper SPE 157112 presented at the SPE Annual Technical Conference and Exhibition, San Antonio, Texas, USA, 157118-157110 October.

Rwechungura, R.W., Bhark, E.W., Miljeteig, O.T. et al. 2012. Results of the First Norne Field Case on History Matching and Recovery Optimization Using Production and 4d Seismic Data. In *SPE Annual Technical Conference and Exhibition*: Society of Petroleum Engineers. ISBN 1613992130.

Skjervheim, J.-A., Evensen, G., Aanonsen, S.I. et al. 2007. Incorporating 4d Seismic Data in Reservoir Simulation Models Using Ensemble Kalman Filter. *SPE journal* **12** (03): 282-292.

Stovas, A. and Arntsen, B. 2006. Vertical Propagation of Low-Frequency Waves in Finely Layered Media. *Geophysics* **71** (3): T87-T94. DOI: 10.1190/1.2197488

Tarantola, A. 2005. *Inverse Problem Theory and Methods for Model Parameter Estimation*: SIAM. Original edition. ISBN 0898715725.

Tura, A. and Lumey, D.E. 1999. Estimating Pressure and Saturation Changes Time-Lapse Avo Data. In *Seg Technical Program Expanded Abstracts 1999*: Society of Exploration Geophysicists.

Vasco, D. 2011. On the Propagation of a Coupled Saturation and Pressure Front. *Water Resources Research* **47** (3).

Vasco, D. and Datta-Gupta, A. 2001. Asymptotics, Saturation Fronts, and High Resolution Reservoir Characterization. *Transport in Porous Media* **42** (3): 315-350.

Vasco, D. and Datta-Gupta, A. 1999. Asymptotic Solutions for Solute Transport: A Formalism for Tracer Tomography. *Water Resources Research* **35** (1): 1-16.

Vasco, D., Datta-Gupta, A., and Long, J. 1997. Resolution and Uncertainty in Hydrologic Characterization. *Water Resources Research* **33** (3): 379-397.

Vasco, D.W. 2004. Seismic Imaging of Reservoir Flow Properties: Time-Lapse Pressure Changes. *Geophysics* **69** (2): 511-521.

Vasco, D.W., Bakulin, A., Baek, H. et al. 2015. Reservoir Characterization Based Upon the Onset of Time-Lapse Amplitude Changes. *Geophysics* **80** (1): M1-M14. DOI: 10.1190/Geo2014-0076.1

Vasco, D.W., Daley, T.M., and Bakulin, A. 2014. Utilizing the Onset of Time-Lapse Changes: A Robust Basis for Reservoir Monitoring and Characterization. *Geophysical Journal International* **197** (1): 542-556. DOI: 10.1093/gji/ggt526

Vasco, D.W., Datta-Gupta, A., Behrens, R. et al. 2005. B. Seismic Imaging of Reservoir Flow Properties: Time-Lapse Amplitude Changes. In *Insights and Methods for 4d Reservoir Monitoring and Characterization*: Society of Exploration Geophysicists and European Association of Geoscientists and Engineers.

Vasco, D.W., Yoon, S., and Datta-Gupta, A. 1998. Integrating Dynamic Data into High-Resolution Reservoir Models Using Streamline-Based Analytic Sensitivity Coefficients. In *SPE Annual Technical Conference and Exhibition*: Society of Petroleum Engineers. ISBN 1555631568.

Veeken, P.C., Priezzhev, I.I., Shmaryan, L.E. et al. 2009. Nonlinear Multitrace Genetic Inversion Applied on Seismic Data across the Shtokman Field, Offshore Northern Russia. *Geophysics* **74** (6): WCD49-WCD59.

Vega, L., Rojas, D., and Datta-Gupta, A. 2004. Scalability of the Deterministic and Bayesian Approaches to Production-Data Integration into Reservoir Models. *SPE Journal* **9** (03): 330-338.

Watanabe, S., Han, J., Hetz, G. et al. 2017. Streamline-Based Time-Lapse-Seismic-Data Integration Incorporating Pressure and Saturation Effects. *SPEJ Society of Petroleum Engineers*.

Wiggins, R.A. 1972. The General Linear Inverse Problem: Implication of Surface Waves and Free Oscillations for Earth Structure. *Reviews of Geophysics* **10** (1): 251-285.

Williams, M., Keating, J., and Barghouty, M. 1998. The Stratigraphic Method: A Structured Approach to History Matching Complex Simulation Models. *SPE Reservoir Evaluation & Engineering* **1** (2): 169-176.

Xia, J., Xu, Y., Miller, R.D. et al. 2010. A Trade-Off Solution between Model Resolution and Covariance in Surface-Wave Inversion. *Pure and applied geophysics* **167** (12): 1537-1547.

Yin, J., Park, H.-Y., Datta-Gupta, A. et al. 2011. A Hierarchical Streamline-Assisted History Matching Approach with Global and Local Parameter Updates. *Journal of Petroleum Science and Engineering* **80** (1): 116-130.

Zhang, Y., Bansal, N., Fujita, Y. et al. 2016. From Streamlines to Fast Marching: Rapid Simulation and Performance Assessment of Shale-Gas Reservoirs by Use of Diffusive Time of Flight as a Spatial Coordinate. *SPE Journal*.

Zhou, C., Schuster, G.T., Hassanzadeh, S. et al. 1997. Elastic Wave Equation Traveltime and Waveform Inversion of Crosswell Data. *Geophysics* **62** (3): 853-868.